

Hydrologic Resources Management Program and Underground Test Area FY 1999 Progress Report

D. K. Smith, G. F. Eaton, T. P. Rose, J. E. Moran, A. Brachmann, J. E. McAninch, A. B. Kersting, V. V. Romanovski, R. E. Martinelli, J. K. Werner Jr.

July 1, 2000

U.S. Department of Energy

Lawrence
Livermore
National
Laboratory

DISCLAIMER

This document was prepared as an account of work sponsored by an agency of the United States Government. Neither the United States Government nor the University of California nor any of their employees, makes any warranty, express or implied, or assumes any legal liability or responsibility for the accuracy, completeness, or usefulness of any information, apparatus, product, or process disclosed, or represents that its use would not infringe privately owned rights. Reference herein to any specific commercial product, process, or service by trade name, trademark, manufacturer, or otherwise, does not necessarily constitute or imply its endorsement, recommendation, or favoring by the United States Government or the University of California. The views and opinions of authors expressed herein do not necessarily state or reflect those of the United States Government or the University of California, and shall not be used for advertising or product endorsement purposes.

This work was performed under the auspices of the U. S. Department of Energy by the University of California, Lawrence Livermore National Laboratory under Contract No. W-7405-Eng-48.

This report has been reproduced
directly from the best available copy.

Available to DOE and DOE contractors from the
Office of Scientific and Technical Information
P.O. Box 62, Oak Ridge, TN 37831
Prices available from (423) 576-8401
<http://apollo.osti.gov/bridge/>

Available to the public from the
National Technical Information Service
U.S. Department of Commerce
5285 Port Royal Rd.,
Springfield, VA 22161
<http://www.ntis.gov/>

OR

Lawrence Livermore National Laboratory
Technical Information Department's Digital Library
<http://www.llnl.gov/tid/Library.html>

**Hydrologic Resources Management Program
and Underground Test Area
FY 1999 Progress Report**

Editors

David K. Smith
Gail F. Eaton

Contributors

David K. Smith
Timothy P. Rose
Jean E. Moran
Axel Brachmann
Jeffery E. McAninch
Annie B. Kersting
Vadim V. Romanovski
Roger E. Martinelli
J. Kent Werner, Jr.*

July 2000

* United States Naval Academy, Annapolis, Maryland

Table of Contents

Chapter	Title	Page
Introduction	FY 1999 HRMP/UGTA Report	i
Chapter 1	Flow-Through Leaching Studies of Archived Nuclear Explosive Melt Glass at 25°C And Near-Neutral pH	1
Chapter 2	Characterization of Groundwater Colloids from the ER-20-5 Well Cluster and Cheshire Underground Nuclear Test	13
Chapter 3	Measurements of Technetium-99 in Nevada Test Site Well Water Samples	35
Chapter 4	Secondary Ion Mass Spectrometry Measurements of Volcanic Tufts Containing Radionuclides from Underground Nuclear Tests	45
Chapter 5	Quadrupole ICP-MS and Multi-Collector ICP-MS: Nevada Test Site Applications	59
Chapter 6	Lithologic, Mineralogic, and Petrographic Characterization of Alluvium from the U-1a 102C and 102D Drifts of the U-1a Tunnel Complex, Nevada Test Site	69

Hydrologic Resources Management Program and Underground Test Area FY 1999 Progress Report

Introduction

This report presents the results from fiscal year (FY) 1999 technical studies conducted by Lawrence Livermore National Laboratory (LLNL) as part of the Hydrology and Radionuclide Migration Program (HRMP) and Underground Test Area (UGTA) work-for-others project. This report is the latest in a series of annual reports published by LLNL to document the migration of radionuclides and controls on radionuclide movement at the Nevada Test Site. The HRMP is sponsored by Defense Programs (DP) of the U.S. Department of Energy, Nevada Operations Office (DOE/NV), and supports DP operations at the Nevada Test Site (NTS) through studies of radiochemistry and resource management related to the defense programs mission. Other participating organizations include the Los Alamos National Laboratory (LANL), the United States Geological Survey (USGS), the Desert Research Institute (DRI) of the University of Nevada, the United States Environmental Protection Agency (EPA), and Bechtel Nevada (BN). The UGTA project is an Environmental Management (EM) activity of DOE/NV that supports a Federal Facilities Agreement and Consent Order between the Department of Energy, the Department of Defense, and the state of Nevada to assess contamination resulting from more than 800 underground nuclear tests conducted at the Nevada Test Site. Participating contractors include LLNL (Earth and Environmental Sciences Directorate, Analytical and Nuclear Chemistry Division), LANL, DRI, USGS, BN, HSI-GeoTrans, and IT Corporation.

The FY 1999 HRMP and UGTA annual progress report follows the organization and contents of our FY 1998 report (Smith et al., 1999). Work for HRMP concentrated on radiochemical studies relevant to DOE Defense Programs and continuing investigations using environmental isotopes as indicators of regional groundwater flow. HRMP initiated a project with the LLNL Stockpile Radiochemistry program to investigate the fractionation of refractory radionuclides to support nuclear test diagnostics of historical core samples and diagnostics for the comprehensive nuclear test ban. In FY 2000 this led to a funded proposal from LLNL Defense and Nuclear Technologies Directorate to develop a method to separate and measure ^{151}Sm with a 90 year-half life in archived post-shot glasses. Support to UGTA in FY 1999 included data acquisition driven by numerical models of the hydrologic source term for nuclear tests conducted beneath Frenchman Flat and Pahute Mesa. The models rely on an accurate measure of the radiologic source term from each test as well as the distribution of radionuclides in the vicinity of the explosion cavity and collapse chimney. In addition, models highlight specific data needs that affect the predicted flux of radionuclides in the near-field as part of a predicted dose assessment for the five principal NTS testing areas. Considerable effort has been made in FY 1999 to provide data essential for credible and technically defensible models of radionuclide transport. In FY 1999 LLNL developed high abundance sensitivity analytical tools to

measure radionuclides in groundwater and geologic materials, measured the concentration of dissolved and non-solute radioactive species in groundwater, and conducted experiments to determine the controls on radionuclide migration.

The FY1999 studies highlighted in this report follow:

- 1) Chapter 1 provides the results from flow-through leaching of nuclear melt glasses at 25°C and near-neutral pH using dilute bicarbonate groundwaters.
- 2) Chapter 2 reports on a summary of the size and concentration of colloidal material in NTS groundwaters.
- 3) Chapter 3 discusses the collaboration between LLNL/ANCD and the Center for Accelerator Mass Spectrometry (CAMS) to develop a technique for analyzing NTS groundwater for 99-Technicium (⁹⁹Tc) using accelerator mass spectrometry (AMS). Since ⁹⁹Tc is conservative like tritium in groundwater systems, and is not sorbed to geologic material, it has the potential for being an important tool for radionuclide migration studies.
- 4) Chapter 4 presents the results of secondary ion mass spectrometry measurements of the in-situ distribution of radionuclides in zeolitized tuffs from cores taken adjacent to nuclear test cavities and chimneys. In-situ measurements provide insight to the distribution of specific radionuclides on a micro-scale, mineralogical controls of radionuclide sorption, and identification of migration pathways (i.e., matrix diffusion, fractures).
- 5) Chapter 5 outlines new analytical techniques developed in LLNL/ANCD to study hydrologic problems at the NTS using inductively coupled plasma mass spectrometry (ICP-MS). With costs for thermal-ionization mass spectrometry (TIMS) increasing relative to sample preparation time and facility support, ICP-MS technology provides a means for rapidly measuring dilute concentrations of radionuclides with precision and abundance sensitivity comparable to TIMS.
- 6) Chapter 6 provides results of a characterization study of alluvium collected from the U-1a complex approximately 300 meters below ground surface in Yucca Flat. The purpose of this investigation was to provide information on particle size, mineralogical context, the proportion of primary and secondary minerals, and the texture of the reactive surface area that could be used to accurately model radionuclide interactions within Nevada Test Site alluvial basins (i.e., Frenchman Flat and Yucca Flat).

Other FY1999 HRMP and UGTA Activities

In addition to the activities described above, LLNL's HRMP and UGTA staff contributed to several other technical products during FY 1999. These products include:

- 1) A paper titled "Aged Nuclear Explosive Melt Glass: Radiography and Scanning Electron Microscope Analyses Documenting Radionuclide Distribution and Glass Alteration," is in peer-review for the *Journal of Radioanalytical and Nuclear Chemistry* (Eaton & Smith, in review). This work was initially outlined in the FY 1998 report (Smith et al., 1999), and was presented at the Methods and Applications of Radioanalytical Chemistry (MARC V) conference. Work is continuing to determine the exact composition of melt glass alteration and distribution from test fired both below and above the level of the standing water table.
- 2) HRMP staff (T. Rose) traveled to the International Atomic Energy Agency in Vienna, Austria in May, 1999 to present a paper entitled "Isotopic Investigation of Recharge to a Regional Groundwater Flow System, Great Basin, Nevada USA" (Rose et al. 1999) at an international symposium on the use of isotopes in hydrology. This paper was included in the FY 1998 LLNL HRMP and UGTA Progress Report (Smith et al., 1999).
- 3) In response by a request by the American Geophysical Union, UGTA staff (A. Kersting) traveled to the 1999 Spring Meeting of the American Geophysical Union in Boston, Massachusetts to give an invited presentation to the union session entitled "The Nevada Test Site as a Natural Analog for the Yucca Mountain Repository: Insights into Radionuclide Migration" (Kersting, 1999).
- 4) The International Atomic Energy Agency published a paper entitled "The Production and Dissolution of Nuclear Explosive Melt Glasses at Underground Test Sites in the Pacific Region" in a symposium volume on international marine pollution (Smith & Bourcier, 1999).
- 5) LLNL staff (A. Kersting) served on the organizing committee of the Seventh International Conference on the Chemistry and Migration Behavior of Actinides and Fission Products in the Geosphere: Migration '99 held in September, 1999 in Lake Tahoe, Nevada / California. LLNL also presented three papers at this conference: A. B. Kersting and A. Brachmann (1999) presented a paper entitled "Identification of Groundwater Colloids from the Nevada Test Site," D. K. Smith (1999) presented a paper entitled "Studies of Radionuclide Migration at the Nevada Test Site in the Era the Comprehensive Nuclear Test Ban," and J.L. Thompson, D.L. Finnegan of LANL and D.K. Smith of LLNL (1999) presented a paper entitled "Radionuclides in Groundwater: A Study of the 1976 Nuclear Test CHESHIRE."

References

- Eaton, G.F. and Smith, D.K. (in review), Aged Nuclear Explosive Melt Glass: Radiography and Scanning Electron Microscope Analyses Documenting Radionuclide Distribution and Glass Alteration, *Journal of Radioanalytical and Nuclear Chemistry*.

- Kersting, A.B. (1999), The Nevada Test Site as a Natural Analog for the Yucca Mountain Repository: Insights into Radionuclide Migration, EOS, Transactions, America Geophysical Union, v. 80, no. 17, p. S1.
- Kersting, A.B. and Brachmann, A. (1999), Identification of Groundwater Colloids from the Nevada Test Site, Seventh International Conference on the Chemistry and Migration Behavior of Actinides and Fission Products in the Geosphere: Migration '99, Lawrence Livermore National Laboratory, UCRL-ID-135626, p. 125.
- Rose, T.P., Davisson, M.L., Criss, R.E. and Smith, D.K. (1999) Isotopic investigation of recharge to a regional groundwater flow system, Great Basin, Nevada, USA. In: Proceedings International Symposium on Isotope Techniques in Water Resources Development and Management, Vienna, 10-May 1999. International Atomic Energy Agency, IAEA-CSP-2/C, session 2, p. 63-72.
- Smith, D.K., Rose, T.P., Eaton, G.F., Kenneally, J.M., Hudson, G.B., and Davisson, M.L., Benedict, F.C., Jr., and Criss, R.E. (1999), Hydrologic Resources Management Program and Underground Test Area Operable Unit FY 1998 Progress Report. Lawrence Livermore National Laboratory Report, UCRL-ID-135170, 76 p.
- Smith, D.K., and Bourcier, W.L. (1999), The Production and Dissolution of Nuclear Explosive Melt Glasses at Underground Test Sites in the Pacific Region, International Atomic Energy Agency Report, IAEA-TECDOC-1094, p. 169-174.
- Smith, D.K. (1999), Studies of Radionuclide Migration at the Nevada Test Site in the Era the Comprehensive Nuclear Test Ban, Seventh International Conference on the Chemistry and Migration Behavior of Actinides and Fission Products in the Geosphere: Migration '99, Lawrence Livermore National Laboratory Report, UCRL-ID-135626, p. 266.
- Thompson, J.L., Finnegan, D. (1999), Radionuclides in Groundwater: A Study of the 1976 Nuclear Test CHESHIRE, Seventh International Conference on the Chemistry and Migration Behavior of Actinides and Fission Products in the Geosphere: Migration '99, Lawrence Livermore National Laboratory Report, UCRL-ID-135626, p. 181.

— Chapter 1 —

Flow-Through Leaching Studies of Archived Nuclear Explosive Melt Glass at 25°C And Near-Neutral pH

David K. Smith and Vadim V. Romanovski

Summary

Flow-through leaching experiments of archived nuclear explosive melt glass from the Nevada Test Site reacted with dilute bicarbonate groundwater and deionized water at 25°C and near-neutral pH showed little evidence of glass-water reaction. The low concentration of radionuclides in the leachate precluded a definitive measure of dissolution rate for the glass. Changes in pH and cation chemistry of the leaching solution may indicate ion exchange reactions initially dominate the glass-water exchange but are not diagnostic of dissolution of the glass matrix. Although the dissolution rate could not be quantified, the results of these experiments suggest that the long-term rate of release of plutonium and other long-lived, toxic radionuclides which are volumetrically incorporated in the melt glass is relatively low. These experimental results also support numerical predictions of glass dissolution under ambient conditions.

Introduction

Long-lived and toxic radionuclide residuals from underground nuclear explosions are principally released to the environment through reactions of groundwater with silicate glass, which sequester these species. The rate at which glass dissolves will govern the activity of radionuclides released per unit surface of the glass area per unit time. The release rate of radionuclides affects the flux of radionuclides transported downgradient from a nuclear explosion. Shock melting accompanying an underground nuclear detonation produces a large amount of glass. More than 700 tons of glass is produced per kiloton of nuclear yield. A recent estimate suggests that more than 30×10^6 metric tons of glass have been produced from the more than 800 underground nuclear tests conducted at the Nevada Test Site (Smith et al., 1999). Studies of the radionuclide content of the melt glasses suggest that greater than 95% of the high temperature, refractory species (including plutonium, americium, and neptunium) preferentially partition into the glass during condensation and become volumetrically incorporated in the vitreous matrix. Ultimately, knowledge of the glass dissolution rate is a critical component of accurate long-term predictive models of radionuclide transport for the Nevada Test Site (see Tompson et al., 1999).

As part of an assessment of the rate of radionuclide release from melt glass, the Analytical and Nuclear Chemistry Division (ANCD) of Lawrence Livermore National Laboratory performed leaching experiments using waters from the Nevada Test Site and samples of nuclear explosive melt debris. In FY 1997 static (batch) leaching experiments

were conducted which ran for approximately one year at 25°C (see Smith et al., 1998). The objective of these tests was to determine the effect of matrix type on the release of radionuclides. Volatile radionuclides which tend to condense on the fracture and mineral surfaces were released faster than refractory radionuclides which were incorporated in the matrix of the melt glass. Leaching rates calculated for the glass samples ranged from 10^{-5} to 10^{-3} grams of glass dissolved per m^2 per day for ^{137}Cs . While static leaching experiments provide a measure of leaching rate, flow-through experiments more realistically simulate the conditions expected for the leaching of melt glass by continually flowing fresh leachate over the solid. Precipitation of secondary phases is thereby avoided and the glass dissolves in a constant composition fluid. In the present experiment, several grams of nuclear explosive melt glass was provided for leaching from the weapons program radiochemistry archives at Los Alamos National Laboratory (LANL). The glass was split into three equal one-gram portions and reacted with bicarbonate groundwater and deionized water at 25°C and near-neutral pH.

There have been two other published studies of single pass leaching of nuclear explosive melt debris. Coles et al. (1978) reported on a 25°C single-pass experiment where NTS groundwaters were exposed to melt glass from a single test for a period of 120 days. Failor et al. (1983) report on the same single pass experiment as Coles et al. (1978) extended to 420 days and involving glass from three separate nuclear tests. Radionuclides leached from these glasses included ^{22}Na , ^{54}Mn , $^{57,58,60}\text{Co}$, ^{95}Zr , ^{106}Ru , $^{124,125}\text{Sb}$, ^{137}Cs , ^{144}Ce , and ^{239}Pu . Leaching rates varied from 10^{-6} to 10^{-3} grams of glass dissolved per m^2 per day for the different radionuclides.

Experimental

The flow-through experiments consist of fluids pumped from three separate reservoirs at a fixed rate through leaching cells which contained ground nuclear explosive melt glass. The design of the experimental apparatus has been described elsewhere; details can be found in Coles et al. (1978) and LLNL (1993). Figure 1 is a picture of the leaching hardware as configured for this experiment; Figure 2 is a schematic of the flow of the leaching solutions through the reactors. The radiochemical content of the melt glass was determined prior to the experiment. To determine the leaching rate, a volume of water is passed over the melt glass. The leaching rate is calculated by measuring the concentration of radionuclides originally in the melt glass that is transferred to the solution.

Leaching Solutions

In this experiment, reservoirs were filled with three different leaching solutions. Leaching solution #1 consisted of Nevada Test Site Water Well 4A groundwater collected in Area 6, which had been passed through a 0.45 μm filter. Water Well 4A groundwaters are produced from bedded and ash-flow tuff aquifers beneath the Yucca Flat testing area. Leaching solution #2 consisted of Nevada Test Site Water Well 4A

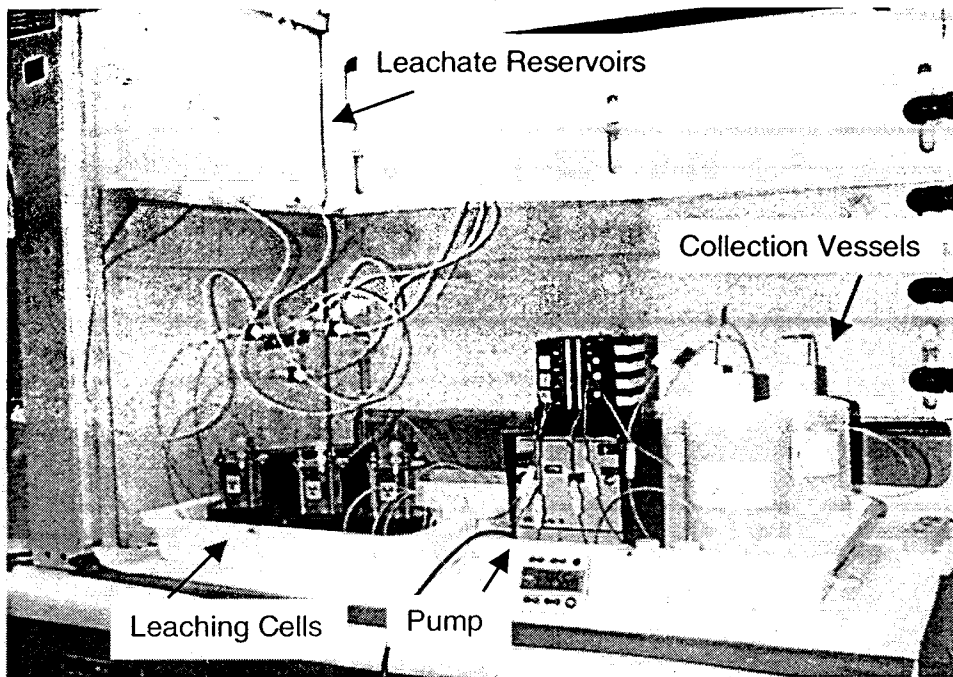


Figure 1: Photograph of leaching apparatus.

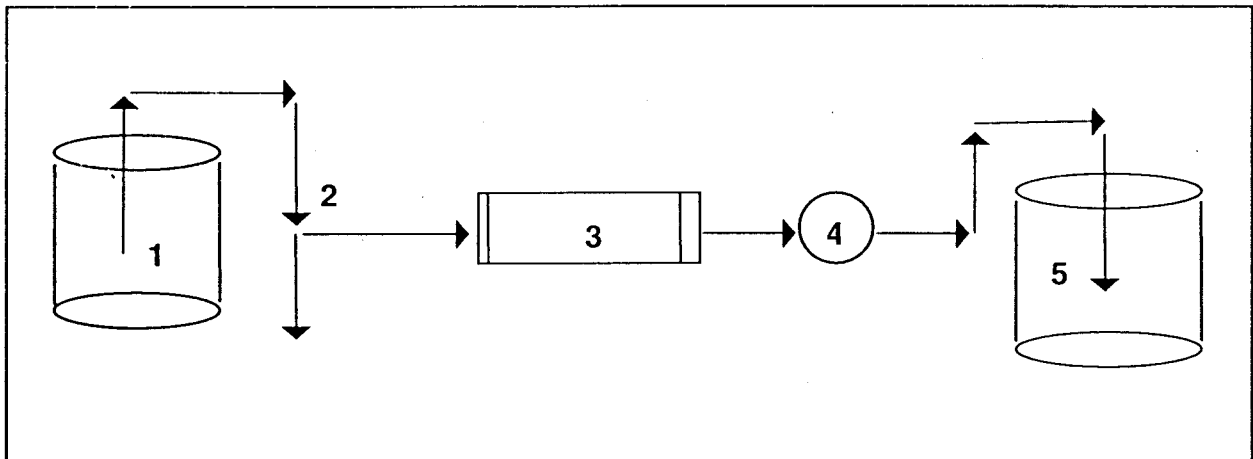


Figure 2: Flow chart of the flow-through leaching system (arrows indicate direction of flow): 1) reservoir for leaching solution; 2) three-way valve; 3) flow-through cell containing nuclear explosive melt glass; 4) peristaltic pump; 5) collection vessels.

groundwater passed through a 0.45 μm filter with the pH adjusted to 7.0 using 0.1M HCl. Leaching solution #3 consisted of deionized milli-Q water. The starting compositions of these fluids are provided in Table 1.

Table 1: Leachate Starting Compositions

Constituent	Water Well-4A: pH 8.35 (mg/L)	Water Well-4A: pH 7.0 (mg/L)	MilliQ Water pH 5.78 (mg/L)
Ca	23	23.7	0.1
Mg	7.14	7.05	0.002
Na	48	52	<0.3
K	5.1	8.8	0.5
Si	28	30	<0.2
Al	<0.06	<0.2	<0.2
Fe	<0.02	<0.03	<0.03
F	0.60		
Cl	11.8		
Br	0.09		
NO ₃	14.7		
PO ₄	<0.07		
SO ₄	38.1		
HCO ₃	168*		

* Bicarbonate analyses conducted on separate sample of Water Well 4A groundwater in 1997.

Melt Glass

Archived samples of ground (pulverized) nuclear explosive melt debris were received from LANL. The melt glass was intentionally selected on the basis of the high levels of radioactivity. Given the time interval between the end of underground nuclear testing and the start of this experiment, a glass sample was selected to provide sufficient activity to be measured in the leaching solution. Only one sample was received from LANL and one gram was used in each of the three reactors. Prior to being loaded, the glass was submitted for X-ray diffraction analysis to determine crystalline constituents. In addition to the glass, the X-ray results indicated the presence of quartz, potassium feldspars (sanidine, orthoclase, and microcline), anorthoclase, plagioclase (albite and anorthite), and clinoptilolite. Quantitative information is unavailable on the amount of crystalline impurities. Examination by optical microscopy suggests that the crystalline phases are subordinant to the majority of the bulk melt glass.

The melt glass sample arrived at LLNL as a disaggregated powder and was dry sieved through a #170 (90 μm), #200 (75 μm), #325 (45 μm) mesh screens to eliminate fines. An aliquot of the sieved material was analyzed by scanning electron microscopy to determine the grain size in order to calculate the geometric surface area available to the leaching solution. The mean particle diameter determined by imaging is 40 μm . Using a

density of 2.3 g/cm³ for the glass, the calculated geometric surface area is 0.065 m²/g. The electron microprobe was used to determine the major element composition of the glass. Eight analyses were conducted with analytical totals between 96.20 and 100.12. Results were normalized to 100% and are listed in Table 2.

Table 2: Major Element Composition of Nuclear Explosive Melt Glass[†]

SiO ₂	TiO ₂	Al ₂ O ₃	FeO*	MnO	MgO	CaO	Na ₂ O	K ₂ O	P ₂ O ₅
74.03	0.17	13.62	3.40	0.06	0.19	1.69	2.17	4.64	0.03

[†] Mean of 8 analyses

* Total iron as FeO

Radionuclides were measured in the sieved glass fraction by gamma counting using fixed Ge(Li) detectors prior to leaching. The fission products, activation products, and nuclear fuel residues detected in the glass are listed in Table 3.

Table 3: Radionuclides in Nuclear Explosive Melt Glass

Fission Products	Activation Products	Nuclear Fuel Residues
¹⁰⁶ Ru, ¹²⁵ Sb, ¹³⁴ Cs, ¹³⁷ Cs, ¹⁵⁵ Eu	²² Na, ⁵⁴ Mn, ⁶⁰ Co, ¹⁵² Eu, ¹⁵⁴ Eu	²⁴¹ Am

Leaching Protocol

Each of three leaching cells was loaded with one gram of the sieved glass (Fig 2.). Filters were supported on either end of each flow-through cell to hold the glass particles in place while permitting the passage of the leaching solution. Each flow-through cell was connected to one of the three leachate reservoirs (Water Well 4A, Water Well 4A at pH 7.0, and deionized water) and a corresponding effluent collection vessel. The experiments were conducted at room temperature (~ 25°C) and ran for a total of twenty eight days. The flow rate of the leachate was initially selected to ensure the fluid in contact with the glass was undersaturated with respect to silica and was increased during the course of the experiment to verify that the leaching rate was independent of the rate at which fluid was passed through the leaching cells; the flow rate was initiated at ~ 30 ml/24 hours, was increased to ~ 60 ml/24 hours after 14 days, and was increased again to ~ 80 ml/24 hours after 21 days. During the experiment the leachate from each of the three cells was sampled approximately every three days or 13 times total over the duration of the trial. Samples were collected into pre-cleaned sample vials and subsequently transferred to Prindle vials for detection of gamma-emitting radionuclides using fixed Ge(Li) detectors. An aliquot was also submitted for major element analysis using inductively coupled plasma – atomic emission spectroscopy and pH using an ion selective electrode.

Although samples were collected throughout the duration of the experiment, samples at five times were selected for analysis of major cations and radionuclides. Table 4 is a summary of the sample name, sampling collection time, corresponding flow rate, pH, and major element and radiochemical concentrations for analyzed samples. Three of the samples were taken during the initial flow rate of ~ 30 ml/24 hours, another after the flow rate had been increased to ~ 60 ml/24 hours, and a final sample after the flow rate had been maximized at ~ 80 ml/24 hours.

Results

The dilute concentrations of radioactivity in the leaching solutions indicates the dissolution rate for this nuclear explosive melt glass is too low to be determined given the present experimental procedure. Radionuclides were only detected in a minority of the leaching solutions; where measured, gamma counting errors are in excess of 40% following five day low-level counts. In addition, shifts in pre- and post-leach major cation chemistry and pH are insignificant (see Table 1 and Table 4) and are not diagnostic of changes in solution chemistry that would be expected to accompany glass dissolution. Initial changes in the leachate chemistry that occurred after 22 hours, 30 minutes of leaching include a slight decrease in Ca concentration, and slight increases in K, Na and Si concentrations on the order several parts per million. Because the changes in chemistry are small, these fluctuations result from ion exchange that affects only the surface of the glass rather than leaching of the glass matrix. Ion exchange is observed in initial reactions of glass with water (Tompson et al., 1999).

Discussion

The flow-through experiments conducted here using nuclear explosive melt debris and dilute bicarbonate groundwater indicates there is little dissolution of the melt glass at ambient temperatures and near-neutral pH. In the presence of three different leaching solutions, there is no measurable transfer of radioactivity from the glass to solution. In the context of studies of the long term release of radionuclides from nuclear explosive melt glasses in the saturated zone at the Nevada Test Site, the outcome of these experiments implies: 1) leaching rates are low enough that they cannot be measured for high silica melt glass with little radioactivity and 2) the experimental results validate numerical predictions for corrosion of the glass which emphasizes the extremely slow dissolution of high-silica glasses under ambient conditions.

As discussed by Tompson et al. (1999), glasses are thermodynamically unstable materials that in time will tend to transform to crystalline materials. Water facilitates this process. General models for glass dissolution predict that insoluble elements such as Al, Ca, Mg, and heavy metals (e.g. actinides) which are volumetrically incorporated in the glass are released and are subsequently incorporated into alteration phases which crystallize on the reacting layer. The expected alteration phases are mainly clays and zeolites. Other elements including the alkalis are released to solution and may be transported away by

Table 4: Leachate Analyses: pH, Major Cation Chemistry, and Radionuclide Concentrations

Sample	Sample Number	Collection Date	Flow Rate (ml/24hours)	Total Leaching Time	pH	Ca (mg/L)	K (mg/L)	Mg (mg/L)	Na (mg/L)	Si (mg/L)	¹³⁷ Cs* DPM / count time	¹³⁷ Cs Count Error
Line #1, Well 4A	11	11/4/98	31.14	22 hours, 30 minutes	8.58	21.02	8.2	7.215	54	30		
Line #2, MQ Water	31	11/4/98	28.54	22 hours, 30 minutes	7.35	<0.05	<0.9	<0.001	1.4	<0.2		
Line #3, Well 4A, pH 7	21	11/4/98	28.64	22 hours, 30 minutes	8.45	22.13	8.9	7.363	56	31	8.29E-1	57.1
Line #1, Well 4A	13	11/11/98	32.69	7 days, 22 hours, 19 minutes	8.59	23.32	5.7	7.144	53	31		
Line #2, MQ Water	33	11/11/98	29.34	7 days, 22 hours, 19 minutes	6.85	<0.05	<0.9	<0.001	<0.3	<0.2		
Line #3, Well 4A, pH 7	23	11/11/98	29.5	7 days, 22 hours, 19 minutes	8.48	23.83	9	7.348	53	32		
Line #1, Well 4A	16	11/17/98	33.37	13 days, 22 hours, 22 minutes	8.61	23.36	5.8	7.166	53	31		
Line #2, MQ Water	36	11/17/98	29.62	13 days, 22 hours, 22 minutes	6.72	<0.05	<0.9	<0.001	<0.3	<0.2	4.86E-1	64.2
Line #3, Well 4A, pH 7	26	11/17/98	29.85	13 days, 22 hours, 22 minutes	8.46	23.01	8.6	7.041	50	30		
Line #1, Well 4A	18	11/20/98	58.82	17 days, 5 hours, 15 minutes	8.6	23.35	5.6	7.129	52	31		
Line #2, MQ Water	38	11/20/98	54.43	17 days, 5 hours, 15 minutes	6.59	0.07	<0.9	0.037	<0.3	<0.2		
Line #3, Well 4A, pH 7	28	11/20/98	54.75	17 days, 5 hours, 15 minutes	8.46	23.36	8.8	7.081	47	29	9.71E-1	40.4
Line #1, Well 4A	112	11/30/98	89.2	27 days, 6 hours, 15 minutes	8.6	23.52	5.1	7.169	53	31	7.20E-1	40.9
Line #2, MQ Water	312	11/30/98	83.97	27 days, 6 hours, 15 minutes	6.36	<0.05	<0.9	<0.001	<0.3	<0.2		
Line #3, Well 4A, pH 7	212	11/30/98	87.28	27 days, 6 hours, 15 minutes	8.34	22.8	8.4	6.941	46	28		

* ¹³⁷Cs was the only radionuclide detected in solution; other radionuclides were below detection limits.

the reacting fluid. Dissolution rates for moderate to high silica (50 –70 weight percent SiO₂) glasses have a minimum at near-neutral pH. Experimental work by Mazer (1987) utilizing flow-through experiments to determine glass leaching rates for low silica (basalt @ ~ <60 weight percent SiO₂), intermediate silica (dacite @ ~ 65 weight percent SiO₂) and high silica (rhyolite @ ~ > 70 weight percent SiO₂) glass over a pH range from 2 to 12 shows a minimum between pH 6 and 7. Figure 3 shows the inverse relationship between rate of dissolution and silica content.

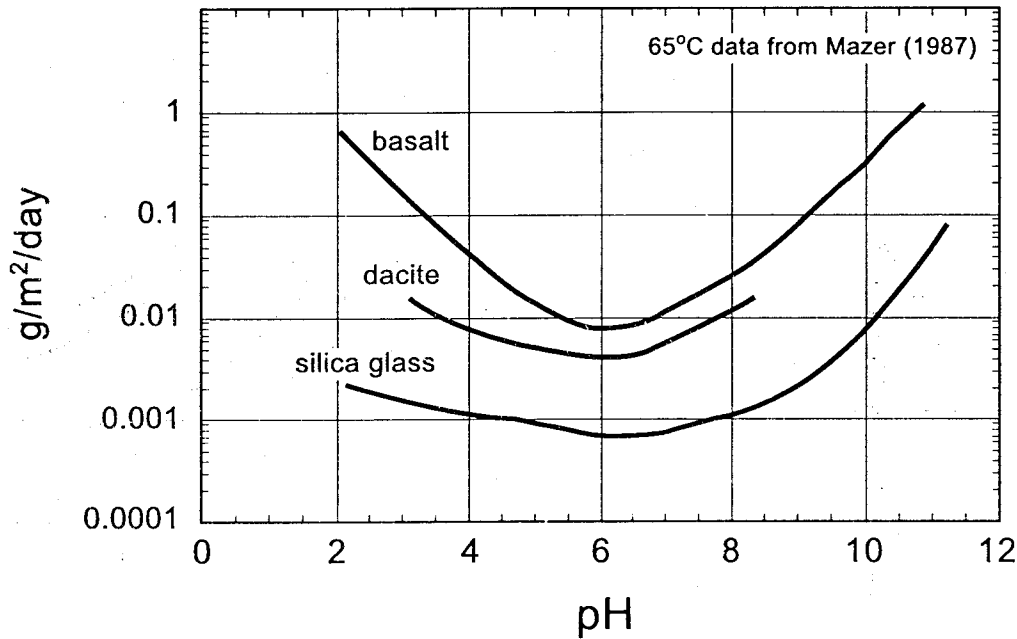


Figure 3: Dissolution Rates for Volcanic Glass at 65°C in g/m²/day (from Tompson et al., 1999)

Because the composition of the melt glass in these flow through experiments (74.03 weight % SiO₂) is nearly equal to that for natural rhyolite glasses (~ 70 weight % SiO₂) investigated by Mazer (1987), Bourcier and Bruton (1999) extrapolate the results of the 65°C dissolution studies of the natural volcanic glasses to estimate the dissolution rate for the nuclear explosive melt glass used in the present experiments. Based on the data in Figure 3, the dissolution decreases by approximately 0.03 log units for each 1% increase in silica content. The Mazer data at 65°C was extrapolated to 25°C using an activation energy of 20 kcal/mol (Tompson et al., 1999). Figure 4 shows the resulting dissolution rate for rhyolite glass at 25°C.

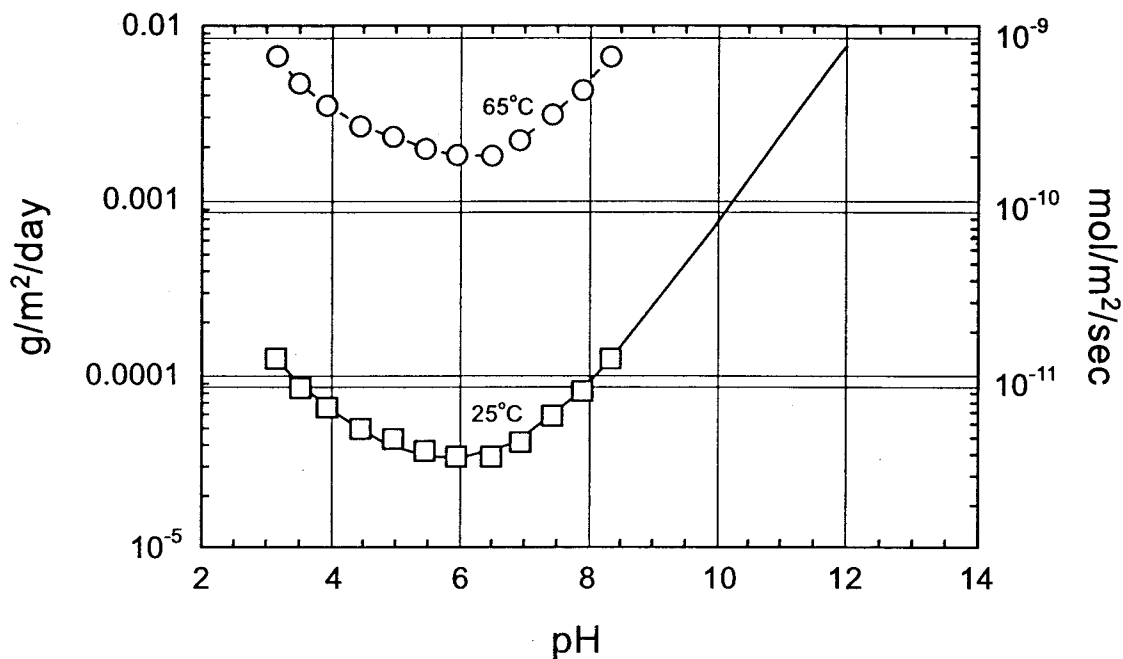


Figure 4: Dissolution Rate of Rhyolite (Melt) Glass at 25°C in g/m²/day and mol/m²/sec.

The modeled dissolution rate for the melt glass at 25°C in contact with a solution with a pH between 6 and 7 is approximately 4.0×10^{-5} grams/m²/day. Using this value for the dissolution rate, a geometric surface area of 0.065 m²/g for the melt glass, 1 gram of glass exposed to solution, and flow-through rate of 30 ml/day, only 0.087 mg of the glass is calculated to dissolve per liter of leaching solution. Using the dissolution model, few radionuclides are expected to be transferred to solution. This prediction matches exactly what is observed in the leaching solution; namely, radionuclides are only incompletely detected in the leachates and, where they are detected, counting errors are extraordinarily large. In addition, there is little change in the cation chemistry in the leachates from the starting composition.

Implications

While this experiment did not return a measure of the dissolution rate for nuclear explosive melt glass, in a broader sense, these results validate predictions made for nuclear melt glass dissolution as well as provide a plausible “lower bound” for the dissolution rate under ambient hydrologic conditions. Figure 4 suggests that the predicted rate of glass dissolution is approximately 4.0×10^{-5} grams/m²/day assuming that the glass composition is rhyolitic (~ 74 weight % SiO₂), the pH is near neutral, and the temperature of reaction is 25°C.

Despite the present combination of prediction and experiment that suggests nuclear explosive melt glass reacts extremely slowly in contact with Nevada Test Site

groundwaters, recent observations of nuclear explosive melt glass collected from below the water table document alteration layers on glass surfaces. The identity and maximum extent of the layers have yet to be determined, but is currently being investigated (Eaton & Smith, 2000; Smith et al., 1999). Smith et al. (1999) speculate that alteration is driven by higher temperatures that occur during the initial cooling of glass in the presence of water that has condensed from the explosion and/or water that flows back into the cavity region. That the glass undergoes a cooling step is important in developing accurate conceptual and predictive models of glass performance and radionuclide release; a single, static temperature does not accurately represent the long-term thermal history of glasses produced during an underground nuclear explosion.

Conclusions

Flow-through experiments conducted using ground high silica nuclear explosive melt debris reacted at 25°C and near-neutral pH yielded dissolution rates that were too low to quantify. This is in keeping with models of glass dissolution which predict dissolution rates of $\sim 4.0 \times 10^{-5}$ grams/m²/day. Several factors combined to contribute to the slow leaching rate: the high silica content of the melt glass, the ambient temperature of the experiment, and the neutral pH of the bicarbonate leaching solution.

The implications of the work provide “good news” for the long-term release of radionuclides from melt-glass at the Nevada Test Site; namely the rate of release of radionuclides after the glass has cooled is relatively low. In addition the experimental results validate recent predictions for the dissolution of nuclear explosive melt glasses at the Nevada Test Site (Tompson et al., 1999; Bourcier and Bruton, 1999). As discussed above, these results should not be interpreted to imply that radionuclides will not be released from nuclear explosive melt debris. As mentioned earlier, static leaching experiments indicate low temperature, volatile radionuclides (e.g., ²²Na, ⁹⁰Sr, ¹²⁵Sb, ¹³⁷Cs) are initially released to solution by ion exchange reactions from sites on exposed mineral and fracture surfaces. In addition evidence from alteration studies of nuclear explosive melt glass imply the glass will dissolve under the higher temperatures initially expected during the period the glass cools. Melt glasses with a lower silica content (~ 60 weight % SiO₂) should dissolve more readily than glasses with a higher silica content (~ 75 weight % SiO₂). At low temperatures, melt glasses at the Nevada Test Site may persist for in excess of one million years (Tompson et al., 1999). The results from the present flow-through experiments suggest that over long periods of time volumetrically incorporated fission products and activation products will be released from the glass at a slow rate and the rate will further decrease because of radioactive decay. The release of plutonium ($t_{1/2} = 2.4 \times 10^4$ years) and other actinides will be governed by the dissolution rate of the glass. With a dissolution rate of $\sim 4.0 \times 10^{-5}$ grams/m²/day, the melt glass will serve as a long-term, low concentration source for these radionuclides.

References

- Bourcier, W.L., and Bruton, C.J. (1999) Modeling Radionuclide Release from the Melt Glass, Lawrence Livermore National Laboratory, unpublished chapter for Frenchman Flat Hydrologic Source Term Report (in preparation).
- Coles, D.G., Weed, H.C., Jackson, D.D., and Schweiger, J.S. (1978) Single Pass Leaching of Nuclear Melt Glass by Groundwater, Part I., Lawrence Livermore National Laboratory Report, UCRL-81617 (preprint), 32 p.
- Eaton, G.F. and Smith, D.K. (in review), Aged Nuclear Explosive Melt Glass: Radiography and Scanning Electron Microscope Analyses Documenting Radionuclide Distribution and Glass Alteration, Journal of Radioanalytical and Nuclear Chemistry.
- Failor, R.A., Coles, D.G., and Rego, J.H. (1983) A Leaching Study of Nuclear Melt Glass: Part I, Lawrence Livermore National Laboratory Report, UCID-19729, 71 p.
- Lawrence Livermore National Laboratory (1993) Procedures for Flow Through Leach Experiments, unpublished Technical Implementing Procedure, 13 p.
- Mazer, J.J. (1987) Kinetics of Glass Dissolution as a Function of Temperature, Glass Composition, and Solution pHs, Ph.D thesis, Northwestern University.
- Smith, D.K., Kersting, A.B., Rose, T.P., Kenneally, J.M., Hudson, G.B., Eaton, G.F., and Davisson, M.L. (1998) Hydrologic Resources Management Program and Underground Test Area Operable Unit FY 1997 Progress Report, Lawrence Livermore National Laboratory Report, UCRL-ID-135170, 92 p.
- Smith, D.K., Eaton, G.F., Rose T.P., Kenneally, J.M., Hudson, G.B., Davisson, M.L., Benedict, F.C., and Criss, R.E., 1999, Hydrologic Resources Management Program and Underground Test Area FY 1998 Progress Report (D.K. Smith and G.F. Eaton eds.). Lawrence Livermore National Laboratory Report, UCRL-ID-135170, 76 p.
- Tompson, A.F.B, Bruton, C.J., and Pawloski, G.A., eds. (1999) Evaluation of the Hydrologic Source Term from Underground Nuclear Tests in Frenchman Flat at the Nevada Test Site: The CAMBRIC Test, Lawrence Livermore National Laboratory Report, UCRL-ID-132300, 319 p.

— Chapter 2 —

Characterization of Groundwater Colloids from the ER-20-5 Well Cluster and Cheshire Underground Nuclear Test

Axel Brachmann and Annie B. Kersting

Introduction

In this report we summarize our results regarding the composition, size distribution, and concentration of colloidal material in groundwaters collected from the Nevada Test Site (NTS). Colloids are defined as particles in solution that are < 1 micron (μm) in size. Samples were collected from wells ER-20-5 #1 and ER-20-5 #3, and drill hole U20n PS1 DDH, a post-shot hole for the CHESHIRE underground nuclear test. Both the ER-20-5 and CHESHIRE drill holes are located on Pahute Mesa in Area 20 at the NTS (Fig. 1). This work was started in FY98 and partially summarized in a progress report entitled: "Progress report on the characterization of groundwater colloids from the ER-20-5 well cluster" (September, 1998).

Groundwater samples from ER-20-5 #3 were collected on April 30, 1998 and samples from well ER-20-5 #1 were collected on July 9, 1998. Groundwater samples from the CHESHIRE region were sampled from two distinct production levels from well U20n PS1 DDH. The first sample (CHESHIRE upper) was taken on July 28, 1998 from the upper perforation interval between 2665 – 2995 (812 – 913m) above a bridge plug. After drilling through the bridge plug, the second sample (CHESHIRE lower) was collected on September 21, 1998 from the lower perforation level between 4100 – 4110 ft (1250 – 1253 m), within the test cavity.

Purpose of this Work

In this study, special care was taken to evaluate the potential effect of sampling and experimental protocols on the detection of colloids. We wanted to make sure that our results regarding the composition, size, and concentration of colloids in groundwaters at the NTS were not impacted by our sampling methods.

Kersting et al. (1999) documented the presence of low levels of Pu in groundwater by identifying Pu originating from an underground nuclear test located 1.3 km away. The Pu and other radionuclides were associated with the colloidal fraction of the groundwater. In turn, this work has raised many unresolved questions concerning: 1) the mineralogy of the colloids, 2) the sorption of radionuclides to colloidal minerals, 3) the colloid concentration in the groundwater, 4) the size distribution of the colloids, and 5) the colloidal flow in fractured media.

the filter (ultra-filtrate) was considered the dissolved fraction. The concentrated retentate was then freeze-dried and prepared for x-ray diffraction (XRD) and scanning electron microscopy (SEM) analysis. The groundwaters collected at ER-20-5 are dilute bicarbonate waters.

This procedure is slightly different from the serial filtration techniques used on the groundwater samples collected in 1997 (Kersting et al., 1999). In previous filtration exercises, 200 liters of groundwater were filtered and the filterable material deposited on the various filters used. A small portion of this material was then scraped off the filters and analyzed. Additional details can be found in 1998 LANL and LLNL reports (Thompson et al, 1998; Smith et al, 1998). In contrast, less than 5 liters of the groundwaters sampled in 1998 were filtered for analysis, and only one size filter was used (~7 nm, 100,000 NMW). Instead of collecting the colloids on the filters, the colloids were concentrated in the retentate and freeze-dried. This eliminated any potential chemical interaction between the colloids and the filters.

Freeze-drying compared with air drying the colloid sample has the advantage of preventing minerals from precipitating as the solution becomes more concentrated (e.g. NTS waters are close to calcite saturation). This technique is also better for preserving the morphology of the clay minerals for resolution on the SEM.

ER-20-5 well cluster

The colloids collected from ER-20-5 #1 and ER-20-5 #3 groundwaters were analyzed by XRD. The results of the analyses show that ER-20-5 #1 consists of zeolites (mordenite, clinoptilolite/heulandite), clays (illite, smectite), and cristobalite (SiO₂). The colloids collected from ER-20-5 #3 groundwaters consist of clays (illite, smectite), and minor zeolites.

The XRD patterns of the two samples were strikingly similar, primarily consisting of clays and zeolites. The major difference between the two samples was the higher concentration of clay minerals relative to zeolites in groundwater colloids from ER-20-5 #3. In contrast, the dominant colloid in ER-20-5 #1 groundwater was the zeolite, mordenite. It should be noted that even though clinoptilolite and heulandite are closely related, they are still distinct zeolites. However, these minerals are not easily distinguished on the basis of XRD or optical properties, therefore the term heulandite/clinoptilolite will be used. The colloidal minerals identified in the ER-20-5 #1 sample were the same as previously identified in groundwater collected in 1997. The two different filtration methods produced identical results, and we conclude that the filters do not chemically react with the colloids.

The physical appearance between the groundwater samples from ER-20-5 #1 and #3, as observed by SEM analysis, was dramatic. The SEM used in this study was a high-resolution Hitachi S4500 capable of imaging very small particles. Routine analysis using

this SEM can resolve images on the order of tens of nanometers (nm) in size. Figures 2 and 3 are SEM images taken of the groundwater colloids from ER-20-5 #1 and #3, respectively. The colloids in ER-20-5 #1 were predominantly rod shaped minerals, the rod shape being a common habit of mordenite. This is consistent with the quantitative results from the XRD analysis. In contrast, the dominant morphology in the ER-20-5 #3 sample was the rounded, platy minerals characteristic of clay minerals. This is again consistent with the quantitative results from the XRD analysis. The minerals were too small for quantitative identification by SEM.

Side-wall cores and rock cuttings taken from well ER-20-5#1 and #3 were also analyzed by XRD to determine if the minerals identified in the colloidal fraction of the groundwater were also present in the rock aquifers. Rock cuttings from well ER-20-5 #1 collected from 2400 ft, 2500 ft, 2600 ft depths were analyzed. These samples bracket the rock aquifer from ER-20-5 #1. No core was recovered from well ER-20-5 #1. Core samples from ER-20-5 #3, collected at depths of 3500 ft, 3750 ft, and 3890 ft, were analyzed. These samples bracket the rock aquifer in ER-20-5 #3.

The mineralogy of rock units from 2400 ft to 2600 ft in well ER-20-5 #1 is fairly uniform, consisting of common silicic volcanic minerals (quartz, sanidine and microcline) and minor secondary alteration minerals (clays and zeolites). The clays consist of illite/smectite and zeolites heulandite/clinoptilolite and mordenite. Although zeolites and clays are the minor phases in the rock aquifer, they dominate the groundwater colloids. The mineralogy of rock units from 3500 ft to 3890 ft in well ER-20-5 #3 is also fairly uniform. These rock units are strongly altered and are predominately clays and zeolites. Specifically, the zeolites are mordenite, and heulandite/clinoptilolite and the clay is illite/smectite. Both host aquifer rocks contain clays and zeolites. Therefore, it is not surprising that the colloidal minerals identified in the groundwaters from ER-20-5 well cluster are minerals also found in the host rock aquifer.

Cheshire drill-back (Well U20n PSI DDH)

The colloids collected in groundwater from both the upper and lower aquifers at Cheshire, were analyzed by XRD and predominantly consist of clays (illite, smectite), and zeolites (mordenite).

SEM photos of the different mineral morphologies are shown in Figure 4. Both samples had minor amounts of the rod shaped minerals indicative of zeolites, while the minerals with the more platy appearance, had the common habit of clay minerals. Again, the individual minerals were much too small for quantitative analysis using the SEM. Energy dispersive analysis (EDS), however, gave an average chemical analysis of a single area of

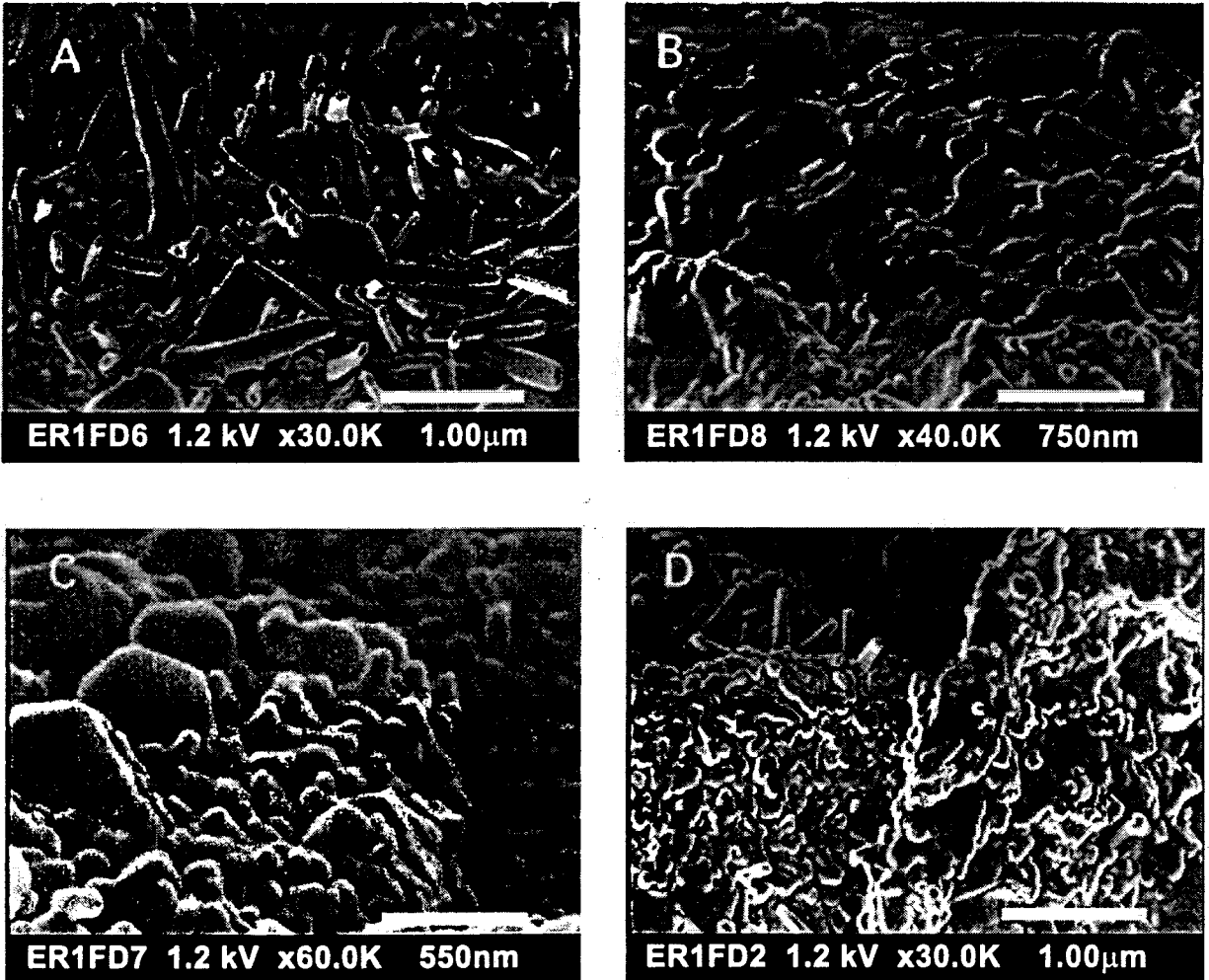


Figure 2: SEM photos of colloids in ER-20-5 #1 groundwater. The rod-shaped minerals shown in (A) are mordenite. The flat, platy appearing minerals in (B) are clays. The blocky minerals shown in (A) and (C) are probably heulandite. All minerals were identified by XRD and only tentatively identified here by their characteristic morphology. Scale bars are shown as the white lines displayed in the bottom right.

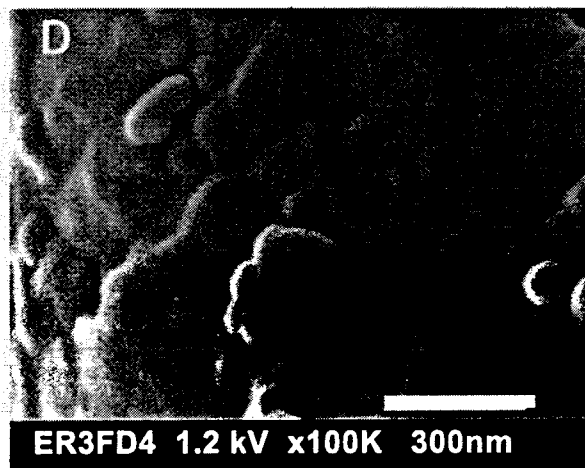
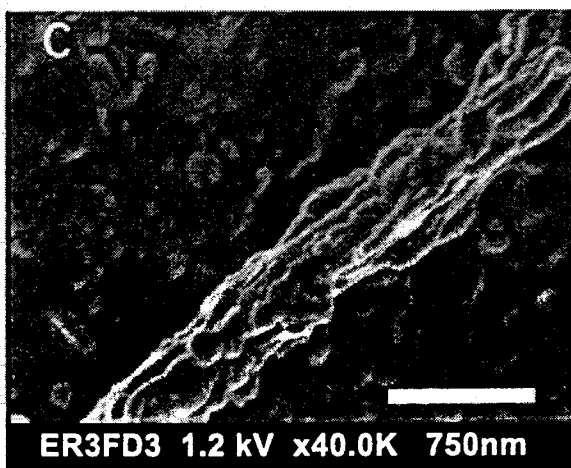
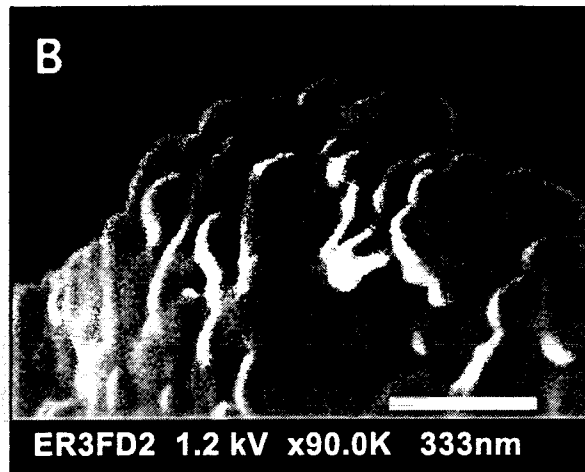
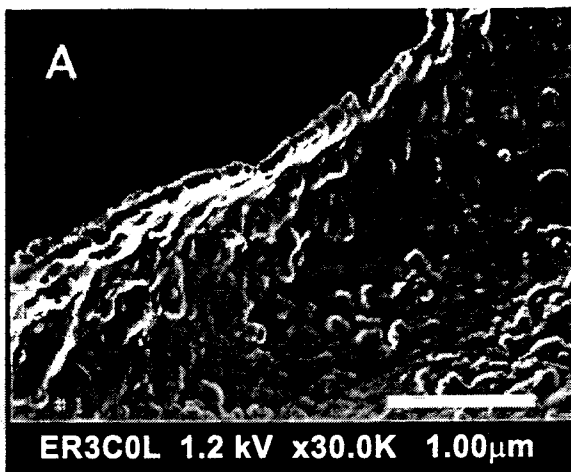


Figure 3: SEM photos of colloids in ER-20-5 #3 groundwater. The minerals shown in (A) are predominantly clays. Mordenite appears infrequently as small rod-shaped laths. All minerals were identified by XRD and only tentatively identified here by their characteristic morphology. Scale bars are shown the white lines displayed at the bottom right.

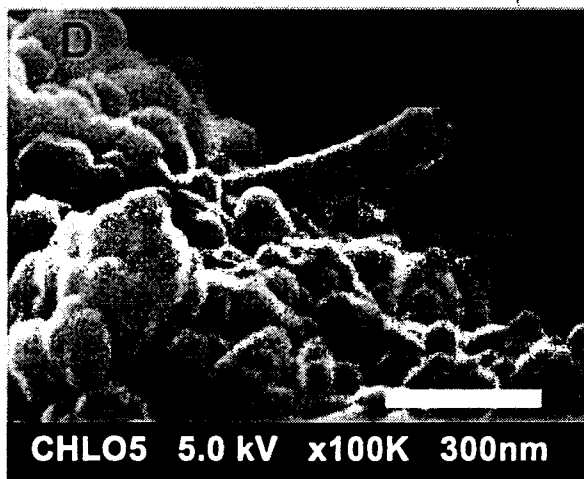
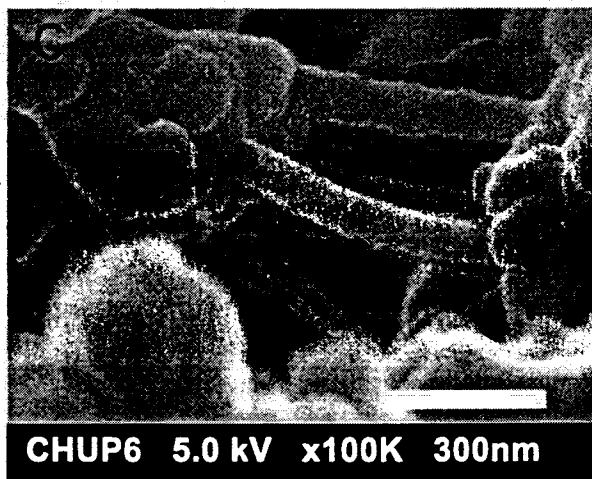
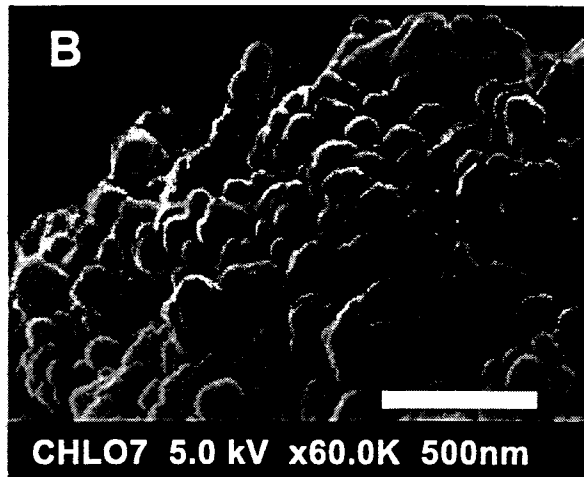
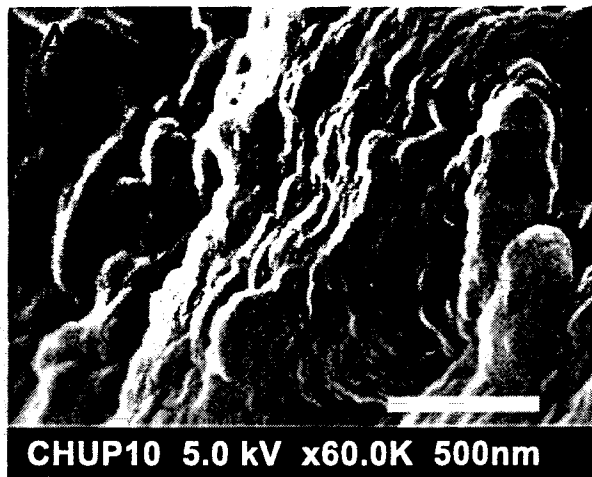


Figure 4: SEM photos of colloids in groundwater from U20n PS1 DDH. The rod-shaped minerals shown in (C) and (D) are thought to be the zeolites identified in the XRD patterns. The flat, platy appearing minerals that dominate the morphology are thought to be clays. All minerals were identified by XRD and only tentatively identified here by their characteristic morphology. Scale bars are shown as the white lines displayed in the bottom right.

colloids that was consistent with, but not diagnostic of silicates, zeolites, and clays. The EDS analysis consisted of Si>Al>Na>Fe+Ca. This is similar to the chemical spectra obtained for the colloids in ER-20-5 samples.

Unfortunately, no rock cuttings were available for mineral analysis from either aquifer unit at CHESHIRE. However, the host rocks are classified as fractured silicic rhyolites and thus it would not be unexpected to observe both clays and zeolites in the host units at the CHESHIRE site.

Size Distribution and Concentration of Colloids

Our objectives for this study were to determine: 1) the concentration and particle size of the colloids, 2) whether the type of sampling container compromised the analyses, 3) if micro-bacterial growth compromised the analyses, and 4) if the length of the storage time compromised the analyses.

In order to answer these questions, samples were collected in plastic, glass, and Teflon containers. All sample containers were acid-leached and rinsed prior to sampling. One set of containers was spiked with preservative (NaNO_3) to kill any potential micro-bacterial growth. In addition, samples were analyzed repeatedly over a period of several months.

Photon correlation spectroscopy (PCS) was used to measure the size distribution and concentration of colloids in the ER-20-5 groundwaters. PCS is a well established particle sizing technique used to determine particle size distribution for a wide variety of scientific and industrial fields (e.g. Allen, 1981; Chu, 1974). PCS is commonly used in the fields of physics and chemistry to characterize colloidal and polymer dispersions, gels, nucleation and aggregation processes, chemical reaction kinetics, and phase transitions.

One of the characteristics of particles in the nanometer to micrometer range that are suspended in a fluid is that they perform a constant, random thermal, or Brownian motion. This causes the intensity of light scattered by the particles to vary with time. Since larger particles move more slowly than smaller particles, the rate of fluctuations of the scattered light will also be slower. The PCS method uses the fluctuation rate of the scattered light to determine the size distribution of the particles suspended in the fluid.

For particle concentration analysis, the static intensity of the scattered light is used. Since standard particle solutions provide the calibration over the concentration range of interest, a set of standards allows the calculation of the concentration calibration functions for each desired particle size. To calibrate the light scattering intensity as a function of particle size and concentration, polystyrene particle standards are used (54 nm, 105 nm, 198 nm, 496 nm and 895 nm). The calibration curves are then fitted to linear equations, the y - intercept being a function of the particle concentration. As a result, the particle concentration can be derived from the light scattering intensity.

The PCS system at LLNL was designed using a INNOVA 70 Ar-ion laser and MALVERN K7032-8 correlator, manufactured by MALVERN Instruments Ltd., Malvern, Worcs., UK (Fig. 5). For each analysis, 4 ml of sample was placed in the sample chamber and analyzed. No dilutions were necessary, although filtrations were performed to determine if there were multiple population sizes in each individual sample.

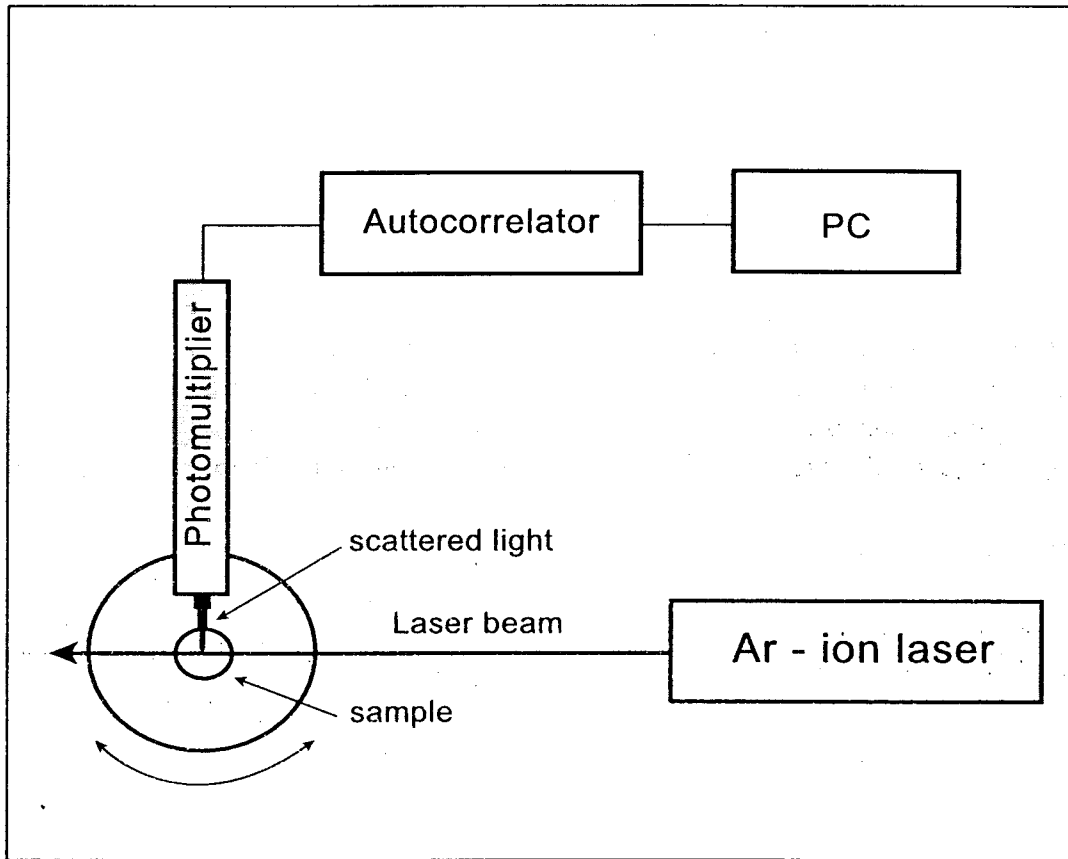


Figure 5: Schematic diagram of the PCS experimental set-up.

ER-20-5 well cluster

The size distribution of colloids measured from ER-20-5 #1 is shown in Figure 6 and 7, and Table 1. Figure 6 shows the variation in colloid size for a representative sample. The samples were filtered to determine if there were multiple size populations. The samples were all mono-modal, with all measured colloids falling within a narrow range from 80 to 100 nm. The average colloid size was 90.9 nm (Table 1). The SEM photos qualitatively confirm this result, since the average size of the colloids in the photos is around 100 nm.

Table 1: Colloid size for ER-20-5 #1.

Container Type	Time in container Following sampling	Average Colloid Size	Standard Error
----------------	--------------------------------------	----------------------	----------------

	(days)	(nm)	
LDPE*	6	86.47	5.85
	20	95.62	4.19
LDPE	7	93.00	3.23
(with preservative)	20	93.73	6.47
	72	90.02	3.25
Glass	7	87.74	5.14
	20	87.70	6.94
Glass	7	96.30	4.84
(with preservative)	20	91.82	6.38
	72	85.37	3.41
Teflon	6	96.34	3.68
	20	86.82	6.56
Teflon	7	89.26	6.44
(with preservative)	20	93.15	0.59
	72	90.12	2.14
	Summed Average:	90.90	

* low density polyethylene plastic

Figure 7 is a plot of the particle size versus time for the samples stored in different containers. The plot shows that the size distribution the colloids in this sample is independent of the type of sampling container used (polyethylene, glass, or Teflon), addition of preservative, or time between sampling and analysis.

The size distribution of the colloids measured from ER-20-5 #3 is shown in Figure 6, 8 and Table 2. Samples were not collected in Teflon containers. All measured colloids were mono-modal and fell within a narrow range of 70 to 85 nm. The average colloid size was 80.8 nm (Table 2). As observed with the colloids from ER-20-5 #1, these data were independent of sample container, addition of preservative, or time between sampling and analysis. The average size of colloids from the ER-20-5 #3 sample was slightly smaller than colloids from ER-20-5 #1.

The colloid concentrations in groundwaters from both ER-20-5 #1 and #3 are shown in Figure 9 and Table 3, and Figure 10 and Table 4, respectively. The average number of colloids in groundwater from ER-20-5 #1 was 3.02×10^{10} colloid particles/ml. In contrast, the average number for ER-20-5 #3 was 7.85×10^{10} colloid particles/ml, indicating that groundwater from ER-20-5 #3 contains approximately 2.6 times more colloids than groundwater from ER-20-5 #1. These differences represent qualitative observations during the filtration process. It was noted that more groundwater had to be

filtered from ER-20-5 #1 than from ER-20-5 #3 for approximately the same volume of colloidal material. Groundwater was pumped from both wells at the same rate (0.03 m³/min).

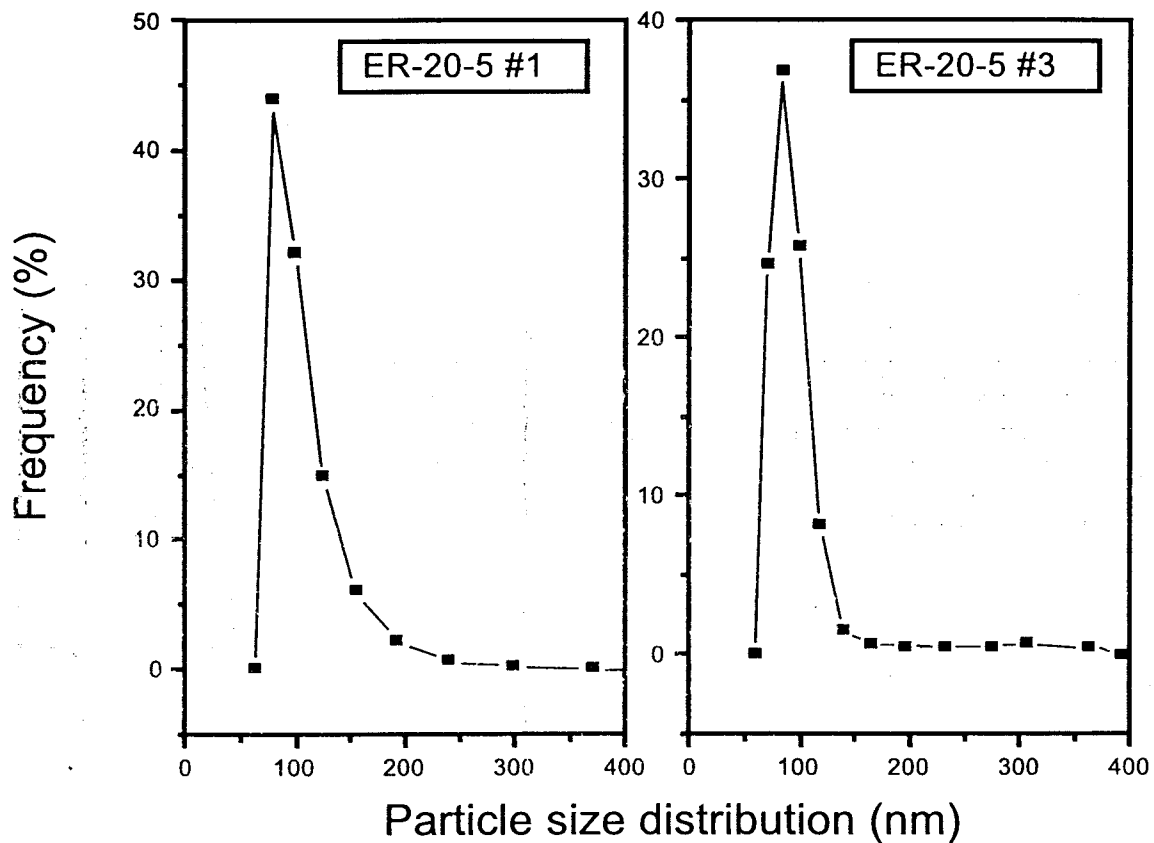


Figure 6: Representative particle size distribution for groundwaters from ER-20-5 #1 and ER-20-5 #3.

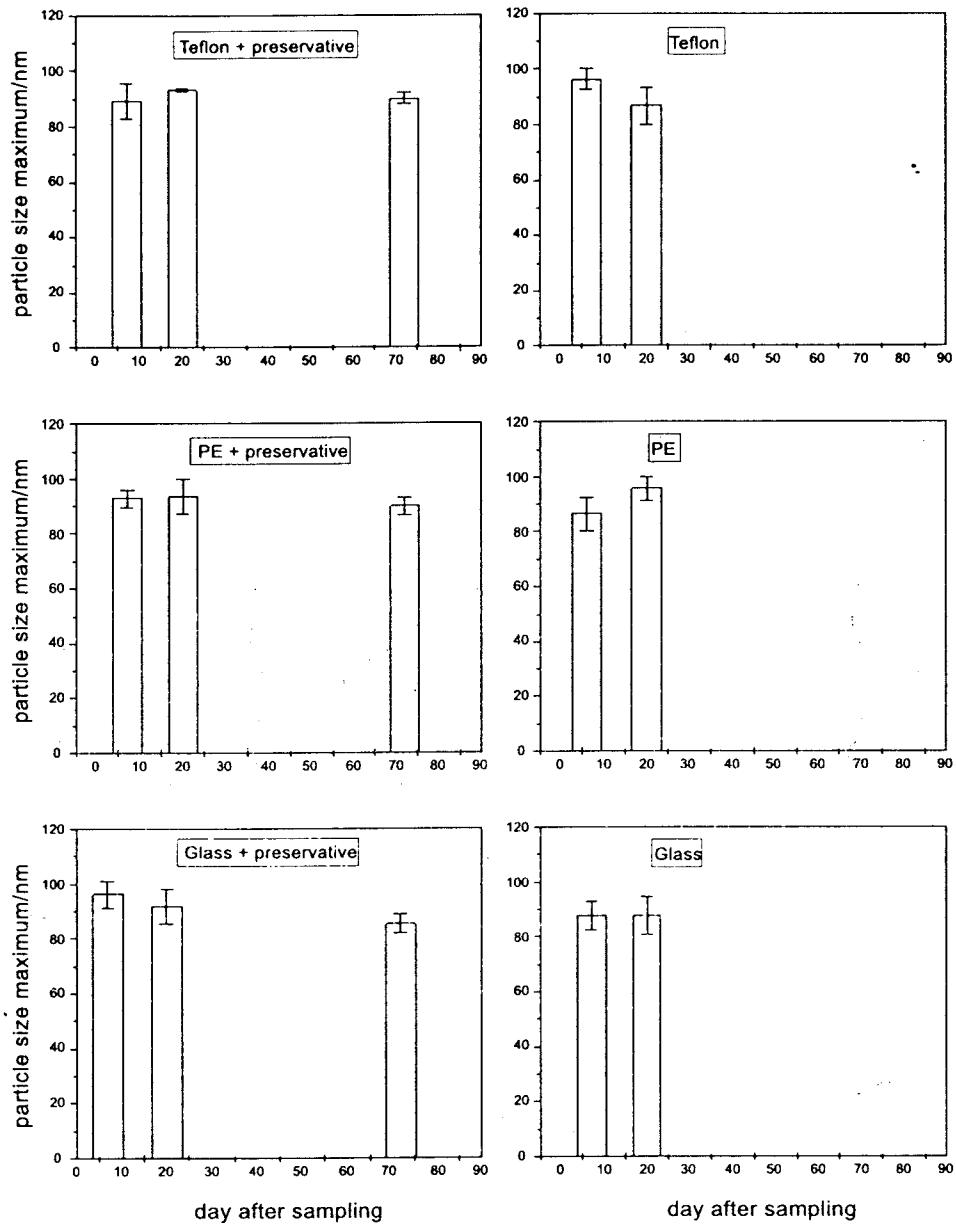


Figure 7: Colloid Size Distribution for groundwater samples from ER-20-5 #1 as a function of time, preservative, and container type. Containers used were glass, teflon, and polyethylene plastic (PE).

Table 2: Colloid size for ER-20-5 #3.

Container Type	Time in container Following sampling (days)	Average Colloid Size (nm)	Standard Error
LDPE	21	81.47	4.01
	30	79.34	4.61
	35	77.35	4.93
	41	80.74	2.39
	48	77.36	3.64
	133	79.59	2.70
LDPE (with preservative)	22	81.85	4.24
	29	76.64	2.87
	30	84.78	7.8
	35	79.89	2.70
	41	84.94	5.95
	48	79.90	5.47
	133	82.78	3.65
Glass	21	81.67	4.23
	29	82.60	4.84
	35	85.30	4.11
	41	80.96	3.87
	48	81.64	3.48
	133	76.40	5.79
	Summed Average:	80.80	

Table 3: Colloid Concentration for ER-20-5 #1.

Container Type	Time in container Following sampling (days)	Number of Colloids (particles/ml)	Standard Error
LDPE	6	3.60×10^{10}	5.57×10^8
	20	2.32×10^{10}	3.59×10^8
	63	2.95×10^{10}	8.80×10^8
LDPE (with preservative)	7	2.72×10^{10}	4.22×10^8
	20	2.57×10^{10}	3.98×10^8
	63	2.72×10^{10}	4.34×10^8
	72	2.94×10^{10}	1.97×10^8
Glass	7	3.42×10^{10}	5.29×10^8
	20	3.60×10^{10}	5.57×10^8
	63	3.59×10^{10}	8.4×10^8
Glass (with preservative)	7	2.31×10^{10}	3.58×10^8
	63	2.82×10^{10}	2.64×10^8
	72	3.83×10^{10}	2.23×10^8
Teflon	6	2.04×10^{10}	3.16×10^8
	20	3.76×10^{10}	5.83×10^8
	63	2.86×10^{10}	7.55×10^8
Teflon (with preservative)	7	3.28×10^{10}	5.07×10^8
	20	1.97×10^{10}	3.05×10^8
	63	2.90×10^{10}	2.14×10^8
	72	2.87×10^{10}	4.14×10^8
	Summed Average:	3.02×10^{10}	

Table 4: Colloid concentration for ER-20-5 #3.

Container Type	Time in container Following sampling (days)	Number of Colloids (particles/ml)	Standard Error
LDPE	21	7.48×10^{10}	1.66×10^9
	30	9.02×10^{10}	1.58×10^9
	35	9.60×10^{10}	1.76×10^9
	41	7.59×10^{10}	9.14×10^8
	48	9.47×10^{10}	7.34×10^8
	133	7.95×10^{10}	1.25×10^8
LDPE	22	7.03×10^{10}	5.76×10^8
(with preservative)	29	1.04×10^{11}	7.00×10^8
	30	6.61×10^{10}	1.03×10^9
	35	8.43×10^{10}	1.04×10^9
	41	5.75×10^{10}	3.68×10^8
	48	7.98×10^{10}	9.27×10^8
	133	6.50×10^{10}	6.55×10^8
Glass	21	6.77×10^{10}	3.24×10^9
	29	7.24×10^{10}	7.50×10^8
	35	5.80×10^{10}	3.05×10^8
	41	7.65×10^{10}	6.85×10^8
	48	7.68×10^{10}	1.29×10^9
	133	1.03×10^{11}	2.56×10^9
	Summed Average:	7.86×10^{10}	

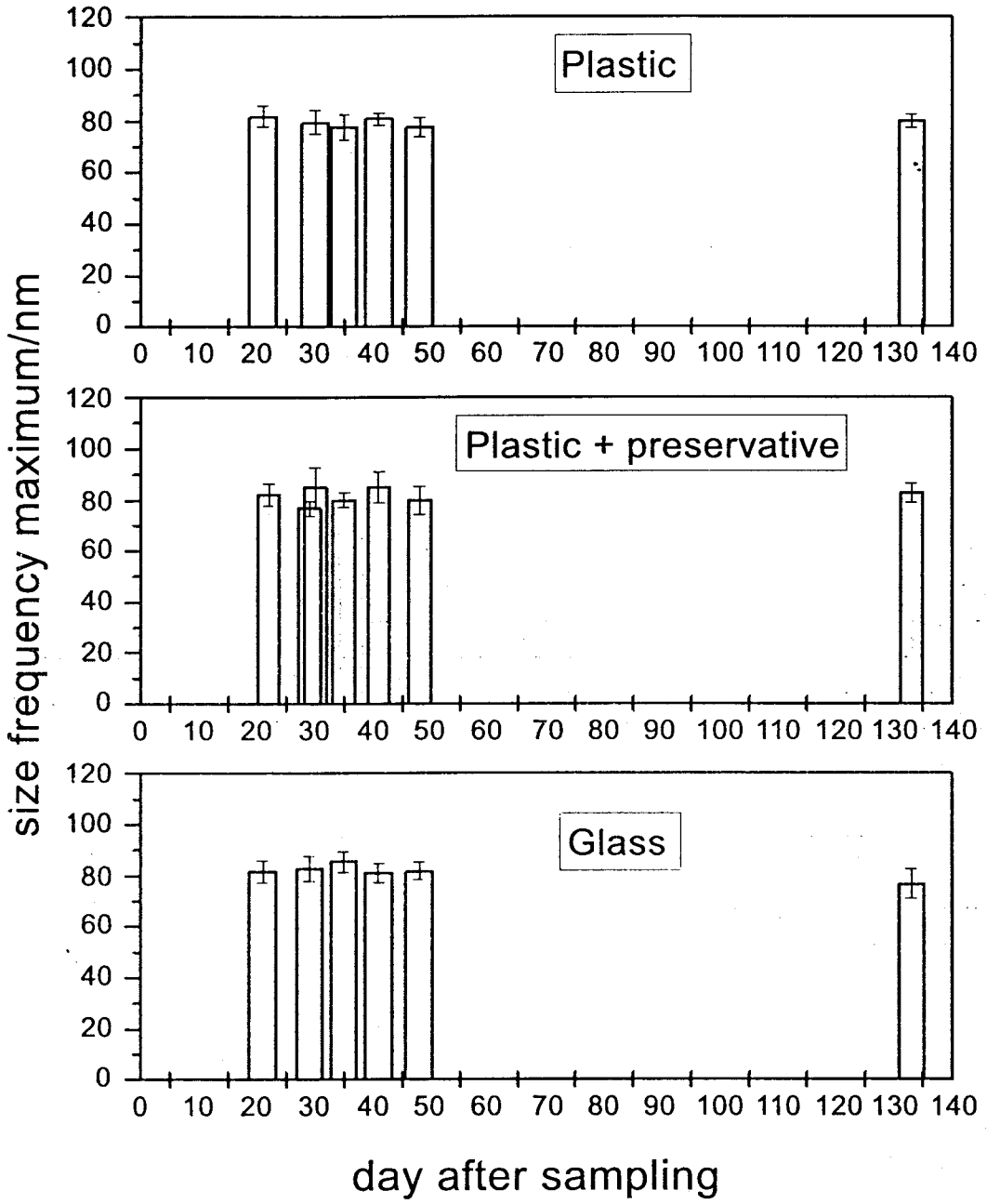


Figure 8: Colloid size distribution for groundwater samples from ER-20-5 #3.

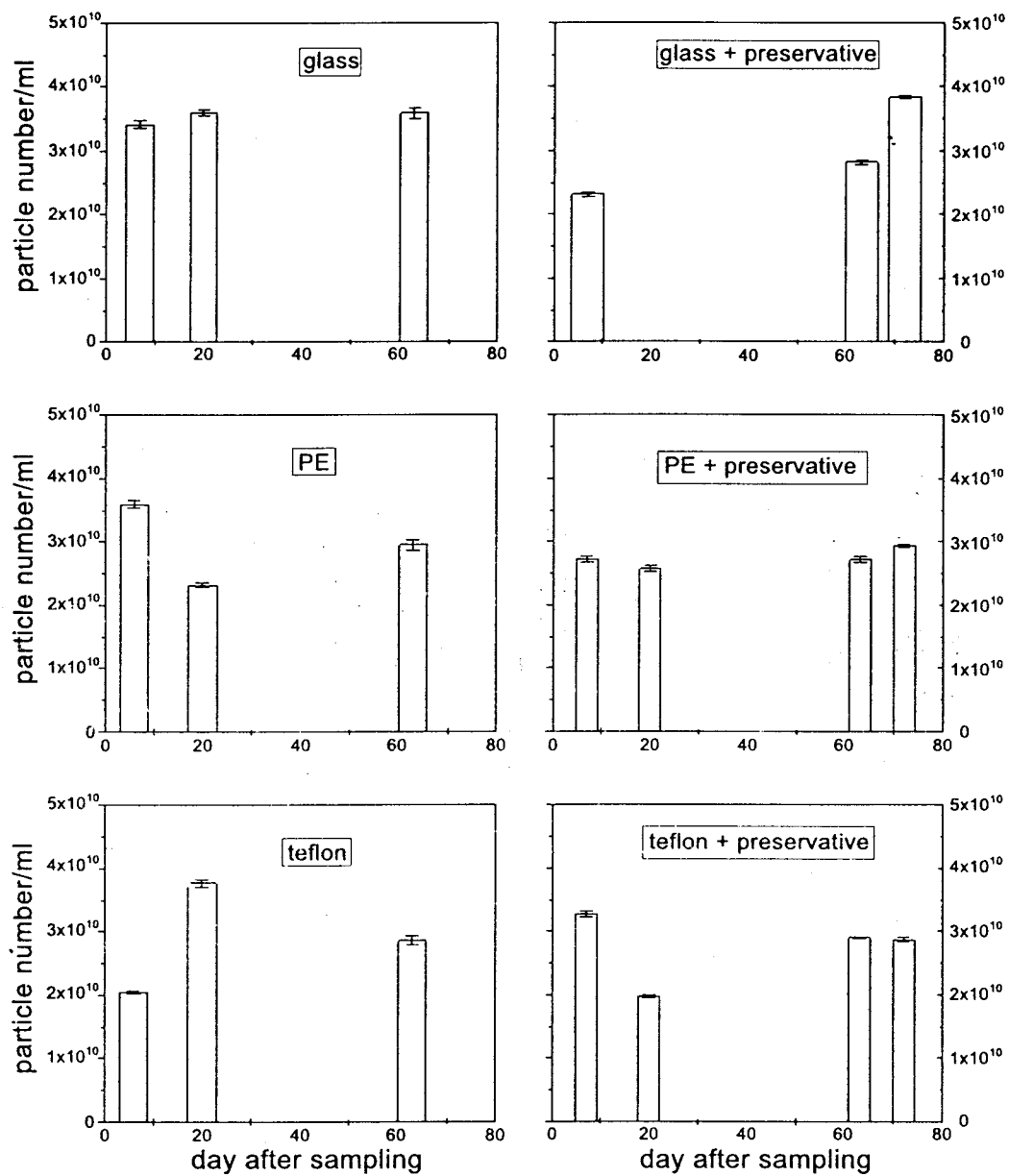


Figure 9: Concentration of colloids in groundwater from ER-20-5 #1 as a function of time.

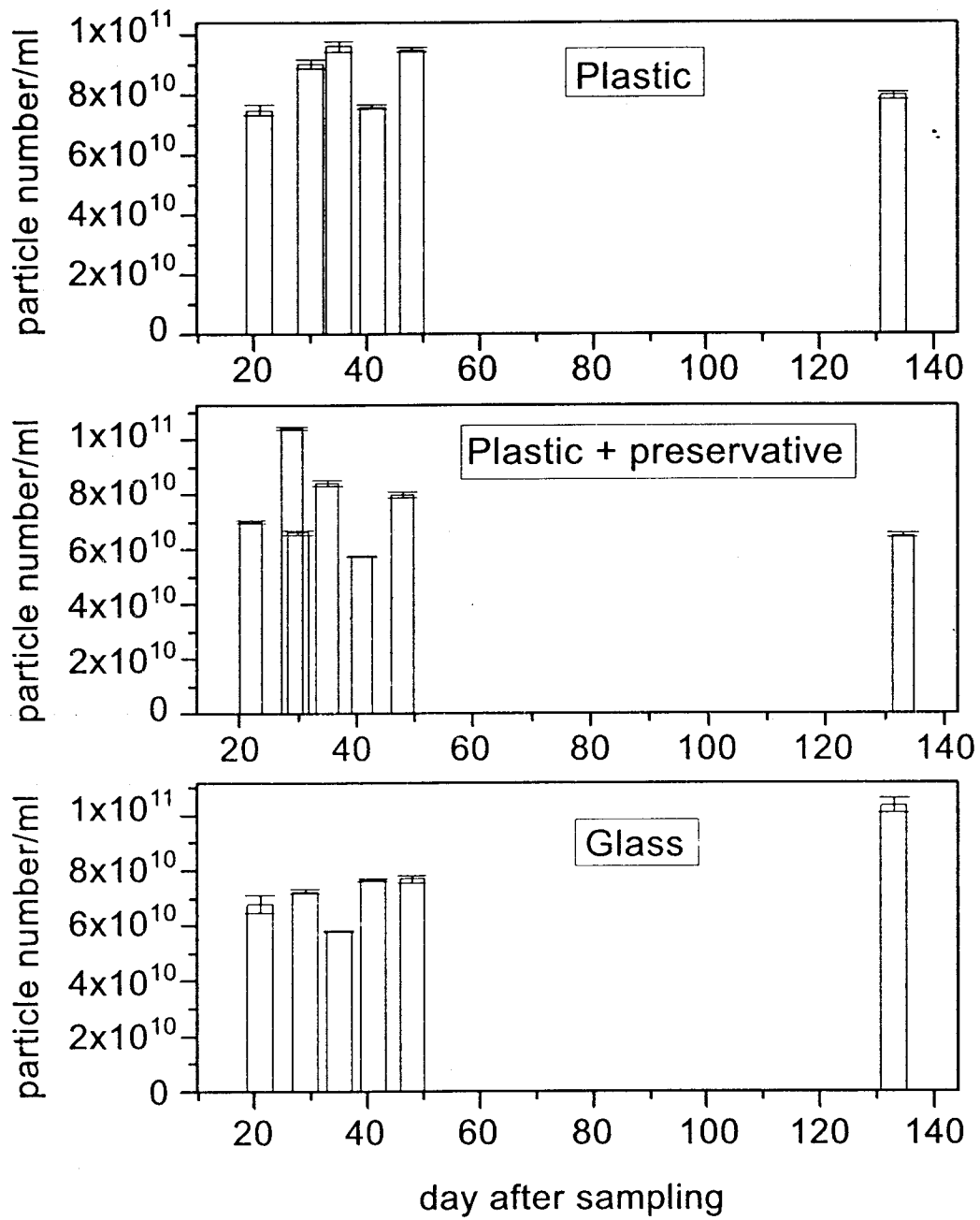


Figure 10: Concentration of colloids in groundwater from ER-20-5#3 as a function of time.

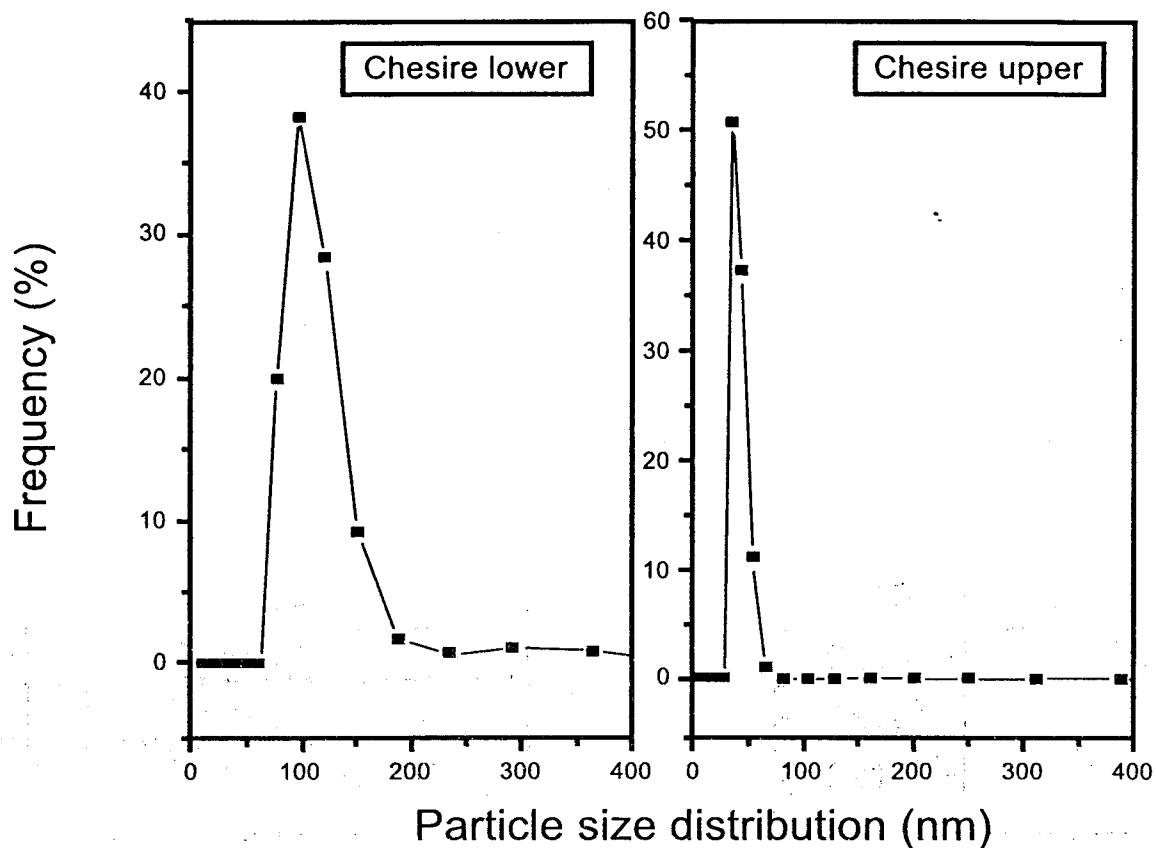


Figure 11: Representative particle size distribution for groundwaters from the upper and lower aquifer at CHESHIRE.

CHESHIRE drill-back (Well U20n PSI DDH)

Having determined that the results from colloid analyses are independent of the sample container used, we collected all of the CHESHIRE samples in plastic 1-liter bottles. All sample bottles were acid-leached prior to sampling. Samples were kept very cool (on ice) until they could be analyzed at LLNL.

Figure 11 shows the variation in colloid size for a representative sample from both the upper and lower aquifer units at CHESHIRE. The samples were filtered to determine if there were multiple size populations. The samples were all mono-modal, with all measured colloids falling within a narrow range from 60 to 100 nm. The average size of colloids from the lower CHESHIRE sample was approximately 90 nm. The average size of colloids from the upper CHESHIRE sample was smaller, averaging approximately 60-70 nm. The SEM photos qualitatively confirm this result, as the average size colloids in the photos are small ($\ll 500$ nm).

All four colloid samples had mono-modal colloid size distributions. Although the average colloid size was different, ranging from 60 to 100 nm, the range was still quite small over

all. It is likely, that under the hydrologic conditions on Pahute Mesa the 100 nm size colloid is dominant.

Conclusions

The combination of XRD, SEM, and PCS analysis was successfully used to characterize the colloids in groundwater collected from four different aquifers on Pahute Mesa at the NTS. To date, from these results we can conclude:

- The colloids in the NTS groundwater samples are mineralogically similar, although the actual abundances of each mineral may vary from aquifer to aquifer.
- The colloidal material is composed primarily of clays and zeolites. This suggests that the potentially important Pu-sorbing minerals are limited to clays and zeolites for groundwaters hosted in silicic volcanic units.
- The same clays and zeolites identified in the groundwater samples are also present in the host rock aquifer at ER-20-5. The colloid minerals mimic the host rock from which they originated.
- The size distribution of the colloids from all four groundwater samples is mono-modal, consisting of small particles between 60 and 100 nm. We suggest that the relatively small colloid size is a reflection of the maximum size that the aquifer has the ability to transport. The ability of aquifers to transport colloids is a function of the host rock mineralogy, water chemistry, width of the fractures, and groundwater flow rate.
- The concentration of colloids in ER-20-5 #1 is approximately 3×10^{10} colloids/ml; ER-20-5 #3 is 8×10^{10} colloids/ml. Groundwater from ER-20-5 #3 has ~ 2.6 times more colloids/ml than ER-20-5 #1 (groundwater was pumped from both wells at the same rate of $0.03 \text{ m}^3/\text{min}$).
- The results of the PCS measurements are independent of sample container used, addition of preservative, or time between sampling and analysis. This result gives us confidence that the size, composition, and concentration of the colloids that we measure reflect what is actually present in the aquifer. The actual concentration of the colloids must be interpreted with caution however, since the pumping rates during sampling were very high. These high pumping rates may have produced an artificially high value for the measured colloid load. Therefore, the concentrations measured in this study most likely represent maximum concentrations of colloidal material.

Future Work

We have identified colloid minerals that may sorb Pu, facilitating transport of Pu by groundwater flowing through the fractured volcanic rocks of Pahute Mesa. We know that

clays and zeolites have the capacity to sorb radionuclides, yet the actual sorption coefficients for these specific minerals, at the sizes measured, are unknown. Since these sorption coefficients are critical in determining the maximum amount of Pu being transported by the colloidal material identified in this study, we plan to continue our Pu-sorption experiments on the minerals identified in the ER-20-5 and CHESHIRE groundwaters, and thus determine the competing geochemical controls on Pu mobility. Based on the results of this study, we will focus our experiments on zeolite and clay minerals found in the NTS groundwaters.

By determining the size distribution and concentration of colloids in groundwaters from Pahute Mesa, these data, in conjunction with colloid identification, will be necessary to predict the concentration of actinides in solution. In addition, these data will also aid efforts to model colloid flow in fractured media and in estimating how far and under what conditions Pu would be expected to migrate. Ultimately, these data will feed numerical models concerned with prediction of a contaminant dose boundary for Western Pahute Mesa.

References

- Allen, T. (1981) Particle Size Measurement. 3rd ed. Chapman & Hall, New York, 678 p.
- Chu, B. (1974) Laser Light Scattering. Academic Press, New York, 317 p.
- Kersting, A.B., Efurud, D.W., Finnegan, D.L., Rokop, D.J., Smith, D.K., and Thompson, J.L. (1999), Migration of plutonium in groundwater at the Nevada Test Site. *Nature*, v. 397, p. 56-59.
- Smith, D.K., Kersting, A.B., Rose, T.P., Kenneally, J.M., Hudson, G.B., Eaton, G.F. and Davisson, M.L. (1998), Hydrologic Resources Management Program and Underground Test Area Operable Unit FY 1997 Progress Report. Lawrence Livermore National Laboratory Report, UCRL-ID-130792, 92 pp.
- Thompson, J.L., Dozier, B.L., Duncan, D.W., Efurud D.W., Finnegan D.L., Kersting A.B., Martinez B.A., Ortego P.K., Rokop, D.J., Smith, D.K., and Thompson, B.K. (1998) Laboratory and Field Studies Related to Radionuclide Migration at the Nevada Test Site October 1, 1996- September 30, 1997 (J.L. Thompson ed). Los Alamos National Laboratory Report, LA-13419-PR, 31 p.

— Chapter 3 —

Measurements of Technetium-99 in Nevada Test Site Well Water Samples

Jeffrey E. McAninch, Roger E. Martinelli, and David K. Smith:

Introduction

In FY99, measurements of Technetium-99 in Nevada Test Site (NTS) well water samples were performed using accelerator mass spectrometry (AMS) at the 10 MV FN tandem accelerator operated by the Lawrence Livermore National Laboratory (LLNL) Center for Accelerator Mass Spectrometry (CAMS). The results reported here constitute some of the first environmental samples measured at CAMS using this newly developed technique (Bergquist et al., 2000). As such, while they demonstrate both the sensitivity and relative ease of the AMS measurements, these data also suffer from some quantitation and sample preparation issues which were not fully resolved when the samples were prepared.

A summary of the results is presented in Table 1, and more detailed data is provided in Tables 2 and 3. Since at this time there is essentially no literature on our methods available in a generally accessible form, a detailed discussion of our measurement protocols, the caveats which apply to the present data, and changes which will be applied in future work is given in the bulleted sections below.

The purpose of this work was to develop an analytical procedure for routine, low-level measurements of ^{99}Tc in groundwaters which are impacted by underground testing at the Nevada Test Site. Technetium-99 is a long-lived ($t_{1/2}=2.13\times 10^5$ a), abundant (6% yield) fission product of ^{235}U and ^{239}Pu . Technetium-99 has previously been detected in NTS waters using liquid scintillation counting. Because NTS groundwaters are oxidizing with near-neutral pH, Tc occurs in these waters primarily as the pertechnetate ion (TcO_4^-), which is not expected to be readily sorbed, and which has the potential to migrate conservatively with tritium. Analysis using AMS provides detection sensitivity and precision which is not available through β -counting methods.

Results

Water samples of 2-90 g were taken for AMS analysis. In March, 1999, a survey of the samples was performed to establish the approximate ^{99}Tc levels. Final results, using triplicates plus a recovery spike aliquot, were measured in August, 1999. The majority of the results listed in Table 1 relate to the August data, however 2 samples were not available for the second round. Measured concentrations ranged from <1 to 1150 mBq/kg. Total measured ^{99}Tc masses per aliquot ranged <15 to 4000 fg.

Samples were normalized to a set of ^{99}Tc secondary standards prepared from serial dilution of a NIST-traceable ^{99}Tc standard. To evaluate the accuracy of our methods, the August data set

included measurements of an IAEA reference material (IAEA-381 Irish Sea water), for which a ^{99}Tc activity concentration of 217 ± 11 mBq/kg has been reported (Povinec et al., 1999). Good agreement to this value was observed in these measurements.

Reproducibility in the measured results is presently ~25%, limited by time-dependent variability in the measured AMS ratios. Uncertainty arising from this variability has been included in the final uncertainties reported in Table 1.

Sensitivity in this data set was limited by high ruthenium interference which was introduced with the process reagents (see detailed discussion). The minimum detectable ^{99}Tc level (3σ above the Ru background) was ~15 fg (~10 μBq , or 1×10^8 atoms) ^{99}Tc per aliquot. Standards containing 20 fg ^{99}Tc were readily measured above background (see Table 2).

Some of the larger aliquots in this data set had problems with high matrix content (see discussion below), but with some additional changes to the methods which were developed for large soil samples, water samples as large as 1 L should be readily measurable. For 1 L aliquots, the minimum detectable activity concentration would be ~0.01 mBq/kg (~ 3×10^{-4} pCi/L).

Following the methods development program, some of which was aimed specifically at the data presented here, ^{99}Tc measurement is now a routine capability at CAMS. Ultimately, with minor modifications to the methods, a factor of 3-10 improvement in ^{99}Tc sensitivity is expected along with improved reproducibility/accuracy.

Summary of FY99 measurement protocol

- 3 AMS aliquots were taken for each sample; aliquot sizes were 2-90 g, depending on the expected ^{99}Tc concentration;
- an additional aliquot, spiked with $^{95\text{m}}\text{Tc}$, was taken for recovery determination;
- samples were boiled with nitric acid and hydrogen peroxide to destroy organics and drive technetium to the pertechnetate form;
- a technetium-specific affinity column (Eichrom TEVA-Spec™) was used for concentration and purification of the Tc; following rinsing with 0.1 M and 1 M nitric acid, Tc was eluted into a teflon vial;
- niobium carrier (approximately 2 mg Nb as peroxoniobium) was added gravimetrically to the eluant; samples were taken to dryness with gentle heating, transferred to a borosilicate test tube, then baked at 400 C; the baked pellet was weighed, crushed and homogenized, then pressed into an AMS target holder;
- $^{99}\text{Tc}/\text{Nb}$ ratios were quantified using AMS; after passing through the spectrometer, ^{99}Tc and ^{99}Ru ions (125 MeV) were detected using a gas ionization detector, allowing measurement and subtraction of the ^{99}Ru isobaric background;
- $^{95\text{m}}\text{Tc}$ recovery was determined by high-resolution gamma counting of the loaded column.

Discussion and changes for future work

- ***Niobium Carrier:*** For the August samples, we implemented for the first time a major modification of our methods. Niobium carrier is now added to the samples in a soluble form (peroxoniobium in a concentrated hydrogen peroxide/nitric acid matrix). This allows a precise gravimetric determination of the amount of Nb which is added, and improves the mixing of the Tc and Nb, both of which significantly improve the reproducibility/accuracy of the measurements. However, for this set of samples, this also increased the level of Ru background by 5-10 times, ultimately degrading the sensitivity of the measurements. The source of this Ru is the large amount of (reagent grade) hydrogen peroxide that was used in preparing the Nb stock. In future work much smaller quantities of ultra-pure hydrogen peroxide will be used.
- ***Detection Sensitivity:*** Sensitivity is determined by the level of Ru present in the final prepared sample. For the present data, this interference was very large equivalent to ~0.2-1 pg ⁹⁹Ru per sample). Even so, the ⁹⁹Tc sensitivity, as evidenced by the blanks and low level standards was typically <15 fg (3σ) per sample following background subtraction. The 20 fg standards shown in Table 2 were readily measurable above background. This level corresponds to an activity concentration of ~0.1 mBq/kg for a 100 g sample. Samples as large as 1 L (and therefore activities as low as 0.01 mBq/kg, or ~3×10⁻⁴ pCi/L) would be quantifiable if sufficient material is available for a given sample.
- ***Reproducibility:*** At present the AMS reproducibility is limited by time-dependent variations in the measured ⁹⁹Tc/⁹³Nb ratios for a given sample. This variation leads to scatter in the results of approximately ± 25%.[†] This scatter can be seen in the standards shown in Table 2. While our experience shows that this variability can be reduced with longer measurement times, and is averaged out with multiple aliquots, for the data presented here we have included an additional ± 25% uncertainty in quadrature with the standard deviation observed in the sample aliquots.
- ***Low-currents in larger aliquots:*** Several of the larger aliquots were not measureable because of large amounts (milligrams) of sample matrix (possibly dissolved salts) which were not fully washed out of the TEVA-Spec™ column and remained in the final eluant. This material has the effect of diluting the Tc and Nb to the point where ion currents are too low for measurement. (Note that not all large aliquots suffered from this problem). For later work with soil samples as large as 200 g, we have included a more aggressive oxidation using persulfate, and a precipitation step using calcium and barium salts which remove this problem.

[†] This variability has also been observed by the only other group measuring ⁹⁹Tc by AMS (K. Fifield, personal communication [1999]).

- *^{95m}Tc spike solution*: The ^{95m}Tc spike solution used in the work was extracted from spallation targets exposed to high energy protons. This material had very high ⁹⁹Tc levels (⁹⁹Tc/^{95m}Tc atom ratio was greater than 1 at the time the measurements were made). Because of this, separate aliquots had to be used for spike recovery measurements. For future work, we will attempt to obtain ^{95m}Tc which is produced by activation of ⁹³Nb with high energy alpha particles. Material produced this way has very low ⁹⁹Tc levels and should be appropriate for addition to every aliquot prepared for AMS.
- *^{95m}Tc spike recovery measurements*: For the August data set, ^{95m}Tc recoveries were measured by high resolution gamma counting of the loaded TEVA-Spec™ column. This leads to large variability in the measured recovery and recoveries greater than 100% (see Table 1). This variability is caused by small variations in the location of the Tc on the loaded column, leading to variations in the geometric efficiency of the gamma measurement. For future work, recovery measurements will be made of the eluant, so that geometry is fixed more precisely.

References

- Povinec, P.P., et al. (1999) Report on the Intercomparison Run and Certified Reference Material IAEA-381: Radionuclides in Irish Sea Water. International Atomic Energy Agency, Monaco.
- Bergquist, B.A., Marchetti, A.A., Martinelli, R.E., McAninch, J.E., Nimz, G.J., Proctor, I.D., Southon J.R., and Vogel, J.S. (2000) Technetium measurements by accelerator mass spectrometry at LLNL. (in press: *in Nuclear Instruments and Methods B*).

Table 1: Measured ⁹⁹Tc concentrations in well water samples. Summary of the results for the water samples. Detailed results are shown in Table 2. The recommended uncertainties ($\pm 1\sigma$) are calculated by adding the standard deviation in quadrature with an overall measurement uncertainty of $\pm 25\%$ as discussed in the text.

Sample Identification	Sampling Date	^{95m} Tc Spike Recovery	Measurements Included	⁹⁹ Tc Concentration (mBq/kg)	⁹⁹ Tc Concentration (pCi/L)	Standard Deviation	Recommended Uncertainty
IAEA-381 Irish Sea Water	07-Sep-93	—	3	220 [†]	5.9	$\pm 15\%$	$\pm 29\%$
GCP20510	13-May-98	124 %	1	< 0.3	< 0.008		
GCP20508	14-May-98	93 %	1	< 1	< 0.03		
GCP20505	30-Apr-98	110 %	1	< 1	< 0.03		
UE3e#4P2 (Area 3 Gamma Scan)	23-Sep-98	90 %	3	1.1	0.030	$\pm 2\%$	$\pm 25\%$
GCP20542	20-Oct-98	113 %	3	3.1	0.084	$\pm 22\%$	$\pm 33\%$
GCP20501	09-Jul-98	100 %	3	9.9	0.27	$\pm 20\%$	$\pm 32\%$
GCP20518	21-Sep-98	97 %	3	745	20	$\pm 2\%$	$\pm 25\%$
UE3e#4P1 (Area 3 Gamma Scan)	23-Sep-98	108 %	3	474	13	$\pm 14\%$	$\pm 29\%$
GCP20519	28-Jul-98	109 %	3	1147	31	$\pm 22\%$	$\pm 34\%$
U-4uPS#2A	23-Sep-98	119 %	3	590	16	$\pm 4\%$	$\pm 25\%$
U19V Run#2 (Area 19 Gamma Scan)	23-Sep-98	not measured	2 [†]	8	0.2	$\pm 7\%$	$\pm 26\%$

[†] A ⁹⁹Tc concentration of 217 ± 11 mBq/kg in IAEA-381 was reported by the IAEA (see P.P. Povinec, *et al.*, "Report on the Intercomparison Run and Certified Reference Material IAEA-381: Radionuclides in Irish Sea Water", International Atomic Energy Agency, Monaco, 1999).

[‡] Sample "U19V Run#2 (Area 19 Gamma Scan)" was unavailable for measurement with the August 1999 data set, so only the preliminary measurements (March 1999 data) are reported.

Table 2: Detailed results for blanks and standards. Blanks and standards from the August, 1999 measurement run.

Sample Identification	^{95m} Tc Recovery	Aliquot ID	Aliquot Mass (g)	Background ⁹⁹ Ru (fg)	Measured ⁹⁹ Tc in Aliquot (fg)	
<u>Instrument/process Blanks</u>						
niobium oxide				330	5	± 4
niobium stock blank				83	1	± 1
Nb stock blank				140	3	± 3
reagent blank				739	-8	± 8
reagent blank				677	-6	± 8
process blank				818	13	± 9
process blank				422	1	± 5
B151 Process Blank (high purity water)		1	100	308	1	± 4
		2	100	184	-4	± 2
		3	100	324	0	± 4
		4	100	353	-4	± 4
				average (± std dev):	-2	± 3
<u>Calibration standards</u>						
2010 fg		A		652	2673	± 33
2000 fg		B		650	1549	± 21
1020 fg		A		475	796	± 13
1010 fg		B		446	1026	± 14
220 fg		A		308	180	± 5
215 fg		B		624	273	± 8
110 fg		A		897	115	± 10
100 fg		B		477	60	± 6
20 fg		A		308	16	± 4
20 fg		B		515	21	± 6

Table 3: Detailed results for ^{99}Tc concentrations in well water samples. Detailed results of measurements of individual aliquots. Unless otherwise indicated, the results shown are from the August, 1999 measurement run.

Sample Identification	^{95m}Tc Recovery ID	Aliquot Mass (g)	Aliquot Mass (g)	Bkgd ^{99}Ru (fg)	Measured ^{99}Tc in Aliquot (fg)	Measured ^{99}Tc in Aliquot (fg)	^{99}Tc Concentration (mBq/kg)	Included in Average	Comments
Evaluation material: IAEA-381 Irish Seawater									
IAEA-381 Irish Sea water	A	2.0	202	627	± 10	193	± 3	✓	
	B	5.1	470	1727	± 24	212	± 3	✓	
	C	10.2	472	4154	± 52	255	± 3	✓	
				average (\pm std dev)		220	$\pm 15\%$		
NTS water samples (detailed results)									
GCP20510 13-May-98	*1A	50.9				0.10	± 0.11		March '99
	*1B	50.0				0.12	± 0.08		March '99
	A	90.0	289	-1	± 4	-0.01	± 0.03	✓	No current
	B	90.0							Low Current
	C	90.0	745	-14	± 9	-0.10	± 0.06	✓	
				recommended value:		< 0.3			
GCP20508 14-May-98	*2A	50.6				0.34	± 0.26		March '99
	*2B	50.4				-0.06	± 0.11		March '99
	A	90.0	836	105	± 17	0.73	± 0.12		Very Low Current
	B	90.0	895	9	± 12	0.07	± 0.08	✓	
	C	90.0	1134	117	± 17	0.81	± 0.12		Very Low Current
				recommended value:		< 1			
GCP20505 30-Apr-98	*4A	50				0.27	± 0.15		March '99
	*4B	50				0.62	± 0.12		March '99
	A	80.0	745	-33	± 12	-0.26	± 0.09		Low Current
	B	80.0	588	5	± 8	0.04	± 0.07		Low Current
	C	80.0	327	49	± 5	0.38	± 0.04	✓	
				recommended value:		< 1			

Table 3: Continued.

Sample Identification	^{95m} Tc Recovery	Aliquot ID	Aliquot Mass (g)	Bkgd ⁹⁹ Ru (fg)	Measured ⁹⁹ Tc in Aliquot (fg)	Measured ⁹⁹ Tc Concentration (mBq/kg)	Included in Average	Comments	
UE3e#4P2 (Area 3 Gamma Scan) 23-Sep-98	90 %	*3A	100			1.11	± 0.13	March '99	
		*3B	100			1.23	± 0.12	March '99	
		A	200	991	337 ± 14	1.06	± 0.04	✓	
		B	200	795	346 ± 12	1.09	± 0.04	✓	
		C	200	206	135 ± 4	0.42	± 0.01		known sample loss
					average (± % std dev):	1.07	± 2 %		
GCP20542 20-Oct-98	113 %	*6A	5.0			4.15	± 1.32	March '99	
		*6B	5.0			6.87	± 1.09	March '99	
		A	100	1002	621 ± 15	3.90	± 0.09	✓	
		B	100	449	479 ± 13	3.01	± 0.08	✓	
		C	100	585	402 ± 11	2.52	± 0.07	✓	
					average (± % std dev):	3.1	± 22 %		
GCP20501 09-Jul-98	100 %	*9A	2.0			61.4	± 18.0	March '99	
		*9B	2.0			25.7	± 5.5	March '99	
		A	25.0	458	337 ± 9	8.5	± 0.2	✓	
		B	25.0	341	362 ± 9	9.1	± 0.2	✓	
		C	25.0	356	483 ± 12	12.1	± 0.3	✓	
					average (± % std dev):	9.9	± 20 %		

Table 3: Continued

Sample Identification	^{95m} Tc Recovery ID	Aliquot Mass (g)	Aliquot Mass (⁹⁹ Ru Bkgd)	Measured ⁹⁹ Tc in Aliquot (fg)	⁹⁹ Tc Concentration (mBq/kg)	Included in Average	Comments
GCP20518 21-Sep-98	*10A	2.0			748 ± 35		March '99
	*10B	2.0			609 ± 23		March '99
	A	2.0	449	2369 ± 30	744 ± 10	✓	
	B	2.0	378	2422 ± 32	760 ± 10	✓	
	C	2.0	462	2329 ± 30	731 ± 9	✓	
				average (± % std dev):	745 ± 2 %		
UE3e#4P1 (Area 3 Gamma Scan) 23-Sep-98	*5A	10.0			484 ± 16		March '99
	*5B	10.0			323 ± 11		March '99
	A	4.0	550	3499 ± 44	549 ± 7	✓	
	B	4.0	452	2807 ± 41	441 ± 6	✓	
	C	4.0	450	2754 ± 35	432 ± 6	✓	
				average (± % std dev):	474 ± 14 %		
GCP20519 28-Jul-98	*7A	2.0			881 ± 31		March '99
	*7B	2.0			820 ± 30		March '99
	A	2.0	433	2867 ± 37	900 ± 12	✓	
	B	2.0	651	4504 ± 57	1414 ± 18	✓	
	C	2.0	425	3589 ± 44	1127 ± 14	✓	
				average (± % std dev):	1147 ± 22 %		

Table 3: Continued

Sample Identification	^{95m} Tc Recovery ID	Aliquot Mass (g)	Aliquot ⁹⁹ Tc Bkgd (fg)	Measured ⁹⁹ Tc in Aliquot (fg)	Measured ⁹⁹ Tc Concentration (mBq/kg)	Included in Average	Comments
U-4uPS#2A 23-Sep-98	*8A	2.0			385	± 15	March '99
	*8B	2.0			395	± 15	March '99
	A	4.0	467	3807 ± 46	598	± 7	✓
	B	4.0	514	3592 ± 48	564	± 8	✓
	C	4.0	678	3874 ± 55	608	± 9	✓
				average (± % std dev):	590	± 4 %	
U19v Run#2 (Area 19 Gamma Scan) 23-Sep-98	NS	2.0			7.5	± 2.6	✓
	*11A	2.0			8.2	± 2.8	✓
	A			no measurement			
	B			no measurement			
				no measurement			
				average (± % std dev):	7.9	± 7 %	
							March '99 data only

— Chapter 4 —

Secondary Ion Mass Spectrometry Measurements of Volcanic Tuffs Containing Radionuclides from Underground Nuclear Tests

Timothy P. Rose, David K. Smith, Douglas L. Phinney

Summary

The *in situ* distribution of anthropogenic radionuclides in volcanic tuffs was measured using secondary ion mass spectrometry (SIMS). Samples were obtained from boreholes drilled in close proximity to expended underground nuclear test cavities at the Nevada Test Site, USA. SIMS measurements revealed the presence of ^{22}Na , ^{137}Cs , and enriched $^{235}\text{U}/^{238}\text{U}$ ratios. The radionuclides are distributed heterogeneously and occur at concentrations ranging from 1 to <0.1 ppm. Two processes govern the distribution of radionuclides outside the nuclear test cavity region: the prompt injection of radionuclides along fractures at the time of the nuclear detonation, and the post-test sorption of radionuclides from groundwater. A zone of prompt injection 37 m above the static water table is characterized by the correlated presence of all three radionuclides – in one case, all within a single (60 μm) point of analysis. ^{137}Cs is the only radionuclide detected in rocks from the saturated zone. Since these volcanic tuffs are highly zeolitized, containing up to 60 wt % clinoptilolite, it is likely that zeolite minerals control ^{137}Cs sorption from groundwater. However, the heterogeneous distribution of radionuclides within the zeolitized samples indicates that micro-fractures in the rock are also important in determining where the radionuclides are deposited.

Introduction

Radionuclide transport in the environment is controlled by a variety of processes including the hydrogeologic and geochemical conditions of the system, the physiochemical nature of the source term, and interactions between dissolved species and the aquifer matrix (Borg et al., 1976; Ticknor et al., 1991; Lieser et al., 1995). An understanding of these processes is essential to designing methods for the cleanup of contaminated sites, for assessing the potential long-term performance of radioactive waste repositories, and for developing engineered barriers for waste isolation (Patera et al., 1990; Silva & Nitsche, 1995; Jedináková-Krizová, 1998). In the United States, efforts are underway to assess the potential health and environmental risks related to radionuclide migration from underground nuclear tests at the Nevada Test Site (NTS), situated ~100 km northwest of Las Vegas, Nevada. The NTS was the location of 828 underground nuclear tests conducted between 1951 and 1992 (DOE/NVOO, 1994), approximately 300 of which were detonated near or below the water table (Laczniaik et al., 1996). Recent drilling projects in the near-field environment have afforded the opportunity for field observations of the occurrence, distribution, and transport of radionuclides derived from these tests (e.g. Buddemeier & Hunt, 1988; Buddemeier et al., 1991; Thompson, 1991; Smith, 1998; Kersting et al., 1999). Data obtained from these

field studies has been essential to the development of models to predict radionuclide transport at the NTS. However, among the critical data that are lacking is specific information on how the radionuclides are distributed in the rock.

The initial distribution of radionuclides following a nuclear test is primarily determined by the relative volatilities of the radionuclide species (or their precursors), and by the extent to which the test was contained by the surrounding rock (Borg et al., 1976; Levy, 1972; U.S. Congress, 1989). Leaching of the nuclear test debris in the aqueous environment can cause the radionuclides to dissolve, form ligand complexes, or attach to colloidal particles, thereby mobilizing "soluble" species in solution (Silva & Nitsche, 1995; Nitsche et al., 1992; Lieser et al., 1990; Kim, 1991). However, the mobility of the dissolved species may subsequently be retarded due to sorption processes (Beall & Allard, 1981; Stumm & Morgan, 1981), depending on the constituent mineralogy of the aquifer rocks.

To investigate the occurrence and distribution of radionuclides in rocks from the near-field environment, volcanic tuff samples were obtained from deep boreholes drilled within a few hundred meters of underground nuclear tests at the NTS. The rock samples were selected from intervals where downhole spectral gamma logs indicated elevated radioactivity. The micro-distribution of radionuclides in the rocks was investigated using secondary ion mass spectrometry (SIMS or ion microprobe). A key advantage of this technique over bulk analytical methods is the ability to detect virtually all elements and their isotopes to trace levels (commonly in the ppb range) with high spatial resolution (Benninghoven et al., 1987; Metson, 1990; MacRae, 1995). SIMS data are presented for radionuclide concentrations at point locations in the samples, and the results are discussed in the context of processes influencing the observed distribution. The SIMS data are complemented by electron microprobe measurements, which provide the means to quantify radionuclide abundances, and elucidate possible mineralogical controls on their occurrence.

Sample acquisition

Drill core samples were obtained from two different near-field wells located on Pahute Mesa, in the northwestern part of the NTS (Fig. 1). ER-20-6 well #1 is located 166 m southwest of surface ground zero for the BULLION test, which was detonated in June 1990. ER-20-5 well #3 is located 290 m southwest of surface ground zero for the TYBO test, detonated in May 1975. Rock samples were drawn from percussion and rotary sidewall core collected after the wells were drilled. Sampling intervals were selected on the basis of anomalies in borehole spectral gamma logs. Additional information regarding the well sites and radionuclide concentrations in groundwater from these wells is found in the literature (Smith, 1998; Kersting et al., 1999).

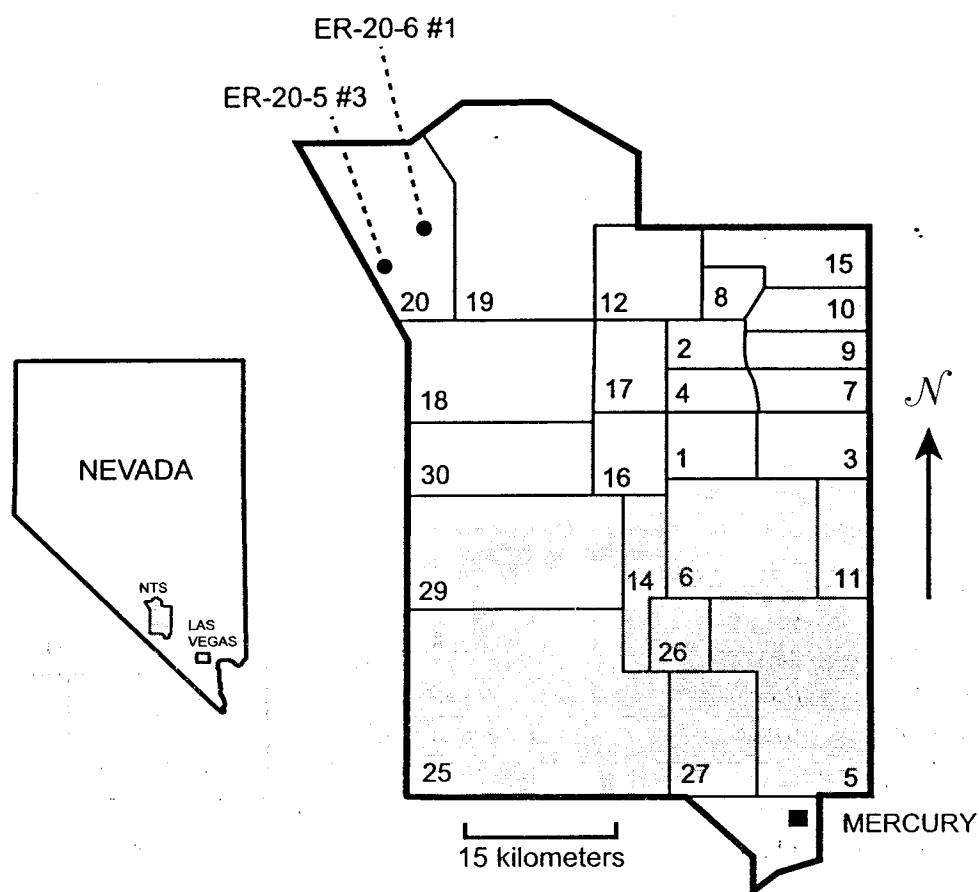


Figure 1: Map showing the location of ER-20-6 well #1 and ER-20-5 well #3, in Area 20 of the Nevada Test Site.

Experimental

Sample Descriptions and Preparation

Three rock samples were selected for analysis. Two of the samples are from ER-20-6 well #1 (581 and 669 m below the surface), and one is from ER-20-5 well #3 (1,143 m below the surface). The samples consist of rhyolitic tuff or lava containing sparse crystals of feldspar and quartz. The glassy matrix that comprises the majority of these rocks has been pervasively altered to zeolite minerals. The sample from ER-20-6 #1 (581 m) is soft, friable, and intensely fractured, whereas the other samples consist of well-indurated, fractured rhyolite.

A strong excursion in the borehole gamma log was observed in ER-20-6 #1 at 581 m depth, indicating the presence of ^{134}Cs , ^{137}Cs , ^{106}Ru , and ^{125}Sb within a 3 m thick interval. This interval is of interest because it lies 37 m above the static water level, and is inferred to represent a zone where radionuclides were emplaced at the time of the BULLION test. Prompt or late time emplacement of volatile radionuclides is expected along regions

where there is a contrast in rock strength (Smith et al., 1996), and lithologic logs suggest “weak” (ash-fall tuff) and “strong” (welded tuff) volcanic rocks may be juxtaposed at this depth interval. Although we cannot rule out the possibility that groundwater briefly rose into this interval immediately following the nuclear test (see discussion below), the relatively narrow region of high gamma activity is consistent with the prompt injection model (Smith et al., 1996). The samples from ER-20-6 #1 (669 m) and ER-20-5 #3 (1,143 m) were both collected below the water table.

Laboratory measurements of gamma spectra using fixed Ge(Li) detectors provided data for ^{22}Na , ^{125}Sb , ^{137}Cs and ^{155}Eu activities in the bulk samples. Measured activities are reported in Table 1 for both the count time (the time of data acquisition) and the decay-corrected zero time of the nuclear detonation. All four species were observed in ER-20-6 #1 (581 m) whereas only ^{137}Cs was observed in ER-20-6 #1 (669 m). Gamma activity was not detected in ER-20-5 #3 (1143 m), and this sample was chosen primarily to provide a baseline for comparison with the ion microprobe results of the other two samples.

Table 1: Laboratory gamma spectra measurements.

Radionuclide	ER-20-6 #1 (581 m)	ER-20-6 #1 (691 m)	ER-20-5 #3 (1143 m)
^{22}Na ($t_{1/2}=2.61$ yrs)			
count time (Bq/g)	1.66×10^{-03}	n.d.	n.d.
zero time (Bq/g)	1.07×10^{-02}	n.d.	n.d.
^{125}Sb ($t_{1/2}=2.76$ yrs)			
count time (Bq/g)	8.63×10^{-02}	n.d.	n.d.
zero time (Bq/g)	5.00×10^{-01}	n.d.	n.d.
^{137}Cs ($t_{1/2}=30.17$ yrs)			
count time (Bq/g)	2.51×10^{-02}	6.16×10^{-02}	n.d.
zero time (Bq/g)	2.96×10^{-02}	7.06×10^{-02}	n.d.
^{155}Eu ($t_{1/2}=4.71$ yrs)			
count time (Bq/g)	1.92×10^{-02}	n.d.	n.d.
zero time (Bq/g)	2.75×10^{-02}	n.d.	n.d.

n.d. = not detected

count time = activity at the time of data acquisition (Jan 1997).

Zero time = decay corrected activity at the time of the nuclear detonation:

ER-20-6 #1 is drilled near the BULLION test cavity, detonated on 13 June 1990.

ER-20-5 #3 is drilled near the TYBO test cavity, detonated on 14 May 1975.

In preparation for ion and electron microprobe analysis, rock cores were sliced into 1 cm wafers using a low speed diamond wafering blade cooled with mineral oil. The wafers were wiped clean using ethanol, mounted in epoxy, and polished with successively finer abrasives down to a 1 μm alumina finish. Water was not used during specimen preparation in order to minimize the possibility of disturbing the *in situ* distribution of radionuclides. Finished sample mounts were coated with a carbon film to alleviate sample charging during microbeam analysis.

SIMS Analytical Methods

Radionuclide concentrations were measured with a modified CAMECA IMS-3f secondary ion mass spectrometer at Lawrence Livermore National Laboratory. Secondary ions were generated by sample bombardment with a 10 nA $^{16}\text{O}^-$ primary beam with a net energy of 17 keV. Analysis typically involved rastering a focused ion beam over a 100 μm x 100 μm area centered on the point of interest, followed by data acquisition using a focused ~60 μm diameter beam. To suppress molecular interferences, an energy filtering technique was used (Shimizu et al., 1978; Zinner & Crozaz, 1986). This involved offsetting the +4.5 kV secondary ion accelerating voltage by -100V relative to the voltage at which the $^{30}\text{Si}^+$ intensity decreased to 10% of its maximum value on the low-energy side. Signals were collected on an electron-multiplier detector, and corrections were applied for counting-system deadtime and background. Each analysis consisted of 5 cycles through 49 masses that targeted 10 different radionuclides: ^3H , ^{22}Na , ^{36}Cl , ^{90}Sr , ^{99}Tc , ^{106}Ru , ^{125}Sb , ^{137}Cs , ^{155}Eu , and ^{235}U . Details regarding isobaric interference corrections are given below.

Secondary-ion intensities measured on “unknown” materials are quantified by comparison with a standard material of known trace element chemistry that has a major element composition similar to that of the unknown (Hinton et al., 1995). Analytical precision is improved by measuring the ratio of the peak intensity of the element of interest to that of a major species (such as $^{30}\text{Si}^+$ in silicates) (MacRae, 1995). Calculation of concentrations from ion intensity ratios was achieved by using relative sensitivity factors (RSF) in a manner analogous to that described in Wilson et al., 1989. RSF values were determined from measurements on the NIST standard reference material SRM-610, a silicate glass containing known concentrations of 61 trace elements. Concentrations in the sample matrix were calculated from the following expression (Zinner & Crozaz, 1986):

$$[\text{X}]_i = (I(\text{X}^+)_i / I(^{30}\text{Si}^+)_i) \times [\text{SiO}_2]_i \times \text{RSF} \quad (1)$$

where the subscript *i* refers to the sample matrix, and $[\text{X}]_i$ is the ppm concentration of the species of interest; $I(\text{X}^+)_i / I(^{30}\text{Si}^+)_i$ is the measured ion intensity ratio of ion species X relative to that of ^{30}Si , corrected for mass interferences; and $[\text{SiO}_2]_i$ is the ppm concentration of SiO_2 in the sample, measured independently on an electron microprobe. Uncertainties in concentrations are dominated by mass interferences or ion counting

statistics, and are reported as one standard deviation of the mean for the respective $I(X^+)_i / I(^{30}\text{Si}^+)_i$ values, based on five measurement cycles.

Measured concentrations of radionuclides were converted into activities using the equation:

$$-\frac{dN}{dt} = \lambda N = \left[\frac{\ln 2}{t_{1/2}} \right] \cdot \left[\frac{X}{A} \cdot N_A \right] \quad (2)$$

where dN/dt is the decay rate for the radionuclide of interest; λ is its characteristic decay constant ($= [\ln 2]/[t_{1/2}]$, where $t_{1/2}$ is the characteristic half-life); X is the concentration of the radionuclide in the sample (in ppm); A is the radionuclide mass number (e.g. for ^{137}Cs , $A = 137$); and N_A is Avogadro's Number. The resulting activity is in units of disintegrations per second (Bq) per unit sample mass.

Isobaric interference corrections

A number of mass peaks corresponding to species of interest were found to have isobaric interferences that were not eliminated by the energy-filtering technique cited in the preceding section. These peaks therefore required a peak deconvolution technique (e.g. Nicolescu et al., 1998). For example, to determine the contribution of ^{137}Cs to the total measured ion intensity at mass 137, a correction must be made for ^{137}Ba inherent in the rock. This is accomplished by taking the product of the natural $^{137}\text{Ba}/^{138}\text{Ba}$ ratio multiplied by the measured $^{138}\text{Ba}^+/^{30}\text{Si}^+$ ion ratio, and subtracting it from the measured $(^{137}\text{Cs}^+ + ^{137}\text{Ba}^+)/^{30}\text{Si}^+$ ion ratio:

$$\left(\frac{I(^{137}\text{Cs}^+)}{I(^{30}\text{Si}^+)} \right) = \left(\frac{I(^{137}\text{Cs}^+ + ^{137}\text{Ba}^+)}{I(^{30}\text{Si}^+)} \right)_{\text{measured}} - \left(\frac{^{137}\text{Ba}}{^{138}\text{Ba}} \right)_{\text{natural}} * \left(\frac{I(^{138}\text{Ba}^+)}{I(^{30}\text{Si}^+)} \right)_{\text{measured}} \quad (3)$$

In this case, the $^{138}\text{Ba}^+/^{30}\text{Si}^+$ ion ratio was initially corrected for a small mass interference from ^{138}Ce . Similar corrections were made for the other radionuclides detected during this study, and are discussed in the results section. Oxide and hydride ion interferences represented less than 1% of the total ion intensity for the respective species of interest, and did not require additional corrections.

Electron Microprobe Analytical Methods

Electron microprobe analyses provide both SiO_2 concentration data for calculating radionuclide concentrations, and quantitative information regarding the mineralogical composition of the sample. In order to correlate the ion probe results with the matrix mineralogy, reflected light and back scattered electron photomicrograph maps were created and used to plot the location of each crater produced during ion bombardment.

These craters were then analyzed using an electron microprobe to determine their major element compositions. Electron probe analyses were made with a JEOL 733 superprobe operated at 15 KeV accelerating voltage and 10 nA beam current with beam stabilization. Four wavelength dispersive X-ray spectrometers were calibrated against oxide mineral standards. ZAF corrections compensated for matrix effects in the conversion of intensity data to oxide concentrations. Several electron microprobe measurements were made at the bottom of each SIMS crater, although the analytical totals were often ≤ 80 wt % due to the presence of hydrous phases (see section: *Sample Mineralogy and Mineral Chemistry*). Independent measurements within individual craters commonly showed small variations in their (Na + K)/Ca ratios. For a given crater, the measurement with the highest analytical total is reported in Tables 3a & 3b.

Results

SIMS Analytical Results

The ion microprobe was used to investigate radionuclide concentrations in both the bulk sample matrix and in phenocrysts. Of 35 individual spots measured on three samples, radionuclides were detected at only six spots – three each in the samples from 581 m and 669 m depth (ER-20-6 well #1). Only three of the 10 species originally targeted for analysis were observed at concentrations greater than their minimum detection limits, following isobaric interference corrections. These are ^{22}Na , ^{137}Cs , and “enriched” ^{235}U . The radionuclides were associated with the zeolitized sample matrix, although ^{137}Cs was detected at one spot in association with a quartz phenocryst. In the latter case, the cesium was probably sorbed to secondary minerals occurring along the margin of the quartz grain.

The SIMS analytical results are reported in Table 2. For comparison, both the measured and the interference-corrected ion intensity ratios ($X^{+}/^{30}\text{Si}^{+}$) are reported. The ratio of these two values (I/I_0) indicates the relative magnitude of the correction (Table 2). In some cases, the mass interference corrections reduced the calculated radionuclide concentrations by more than an order of magnitude. Analytical errors were assigned using standard statistical methods of error propagation. Errors on individual analyses vary from 9% up to 160%, with larger errors corresponding to fewer secondary ions detected. The corrected ion intensity ratios were converted to concentration data (in ppm) using the reported RSF values (determined from NBS-610) and SiO_2 concentrations measured on the electron microprobe. These results are illustrated in a bar graph (Fig. 2) showing radionuclide concentrations at the six spots where quantitative data were obtained. Note that two of the spots in the 581 m sample (from the unsaturated zone) contain more than one species. The correlated occurrence of species with substantially different volatilities (e.g. Na and U) is consistent with the rapid deposition of radionuclides in a zone of prompt injection (see discussion).

Radionuclide activities (in Bq/ng) were calculated from the concentration data in Table 2. Whereas the ppm concentrations of the different species vary by <2 orders of magnitude,

Table 2: SIMS analytical results.

Species	Relative Sensitivity Factor (NBS-610)	Isobaric Interference	Sample	SiO ₂ Conc. (wt %)	Ion Intensity Ratio (X ⁺ / ³⁰ Si ⁺) (measured)	Ion Intensity Ratio (X ⁺ / ³⁰ Si ⁺) (corrected for Mass Interference)	Magnitude of Interference Correction (I/I ₀ in %)	Radionuclide Conc. (ppm)	Radionuclide Activity (Bq/ng)
²² Na	1.59 x 10 ⁻²	⁴⁴ Ca ⁺⁺	20-6#1 (581m) spot.2	59.89	8.83 x 10 ⁻⁴	(1.55 ± 0.64) x 10 ⁻⁴	17.6	1.48 ± 0.61	3.4 x 10 ⁻¹
			20-6#1 (581m) spot.3	67.78	5.81 x 10 ⁻⁴	(3.04 ± 4.26) x 10 ⁻⁵	5.2	1.33 ± 0.46	7.6 x 10 ⁻²
¹³⁷ Cs	1.50 x 10 ⁻²	¹³⁷ Ba ⁺	20-6#1 (581m) spot.1	59.89	1.84 x 10 ⁻⁴	(0.91 ± 1.47) x 10 ⁻⁵	4.9	0.08 ± 0.13	2.6 x 10 ⁻⁴
			20-6#1 (669m) spot.2	100.0	5.67 x 10 ⁻⁵	(2.30 ± 1.05) x 10 ⁻⁵	40.6	0.35 ± 0.16	1.1 x 10 ⁻³
			20-6#1 (669m) spot.6	67.61	9.17 x 10 ⁻⁵	(4.81 ± 6.67) x 10 ⁻⁶	5.2	0.05 ± 0.07	1.6 x 10 ⁻⁴
			20-6#1 (669m) spot.8	62.86	6.09 x 10 ⁻⁵	(4.03 ± 1.48) x 10 ⁻⁶	6.6	0.04 ± 0.01	1.3 x 10 ⁻⁴
¹³⁷ Cs	9.21 x 10 ⁻²	²³⁵ U natural	20-6#1 (581m) spot.2	59.89	4.13 x 10 ⁻⁶	(2.96 ± 1.58) x 10 ⁻⁶	71.7	0.16 ± 0.09	1.3 x 10 ⁻¹¹
			20-6#1 (581m) spot.3	67.78	8.49 x 10 ⁻⁶	(5.67 ± 1.34) x 10 ⁻⁶	66.8	0.35 ± 0.08	2.8 x 10 ⁻¹¹
			20-6#1 (581m) spot.4	59.71	1.24 x 10 ⁻⁵	(9.25 ± 0.85) x 10 ⁻⁶	74.6	0.51 ± 0.05	4.1 x 10 ⁻¹¹

Table 3a: Representative Major Element Analyses for ER-20-5 and ER-20-6 Zeolites in Weight Percent

	ER-20-6 #1 581 m Spot 2	ER-20-6 #1 581 m Spot 3	ER-20-6 #1 581 m Spot 4	ER-20-6 #1 581 m Spot 6	ER-20-6 #1 669 m Spot 4	ER-20-6 #1 669 m Spot 6	ER-20-6 #1 669 m Spot 8	ER-20-5 #3 1143 m Spot 2	ER-20-5 #3 1143 m Spot 3
SiO ₂	59.89	67.78	59.71	61.47	65.67	67.61	62.86	60.90	63.63
TiO ₂	0.00	0.01	0.13	0.08	0.02	0.06	0.03	0.00	0.01
Al ₂ O ₃	10.70	12.41	11.36	10.13	9.73	11.10	10.49	10.21	11.11
FeO	0.16	0.10	1.01	0.60	0.15	0.26	0.35	0.06	0.59
MnO	0.00	0.02	0.05	0.03	0.00	0.00	0.01	0.01	0.00
MgO	0.13	0.09	1.30	0.16	0.02	0.00	0.03	0.00	0.00
CaO	1.02	1.09	0.68	0.96	1.01	0.45	1.01	0.92	0.60
Na ₂ O	3.69	2.01	1.08	1.97	9.56	3.36	6.88	4.84	4.73
K ₂ O	4.21	3.97	3.41	3.61	4.30	3.78	5.83	2.51	4.46
P ₂ O ₅	0.00	0.02	0.00	0.02	0.00	0.02	0.02	0.05	0.00
Total	79.79	87.50	78.73	79.02	90.46	86.65	87.51	79.50	84.61

Table 3b: Unit Cell Composition Based on 72 Oxygens

	ER-20-6 #1 581 m Spot 2	ER-20-6 #1 581 m Spot 3	ER-20-6 #1 581 m Spot 4	ER-20-6 #1 581 m Spot 6	ER-20-6 #1 669 m Spot 4	ER-20-6 #1 669 m Spot 6	ER-20-6 #1 669 m Spot 8	ER-20-5 #3 1143 m Spot 2	ER-20-5 #3 1143 m Spot 3
Si	29.46	29.86	29.35	30.14	29.22	30.16	28.98	29.77	29.46
Ti	0.00	0.00	0.05	0.03	0.01	0.02	0.01	0.00	0.00
Al	6.20	6.45	6.58	5.85	5.10	5.83	5.70	5.88	6.06
Fe ⁺²	0.06	0.04	0.41	0.24	0.06	0.10	0.13	0.03	0.23
Mn	0.00	0.01	0.02	0.01	0.00	0.00	0.00	0.00	0.00
Mg	0.10	0.06	0.95	0.12	0.01	0.00	0.02	0.00	0.00
Ca	0.54	0.51	0.36	0.50	0.48	0.21	0.50	0.48	0.30
Na	3.52	1.72	1.03	1.87	8.25	2.91	6.15	4.58	4.25
K	2.64	2.23	2.14	2.26	2.44	2.15	3.42	1.57	2.63
P	0.00	0.01	0.00	0.01	0.00	0.01	0.01	0.20	0.00
(Al+Fe)/(2Mg+2Ca+Na+K)	0.84	1.27	1.21	1.13	0.44	1.08	0.55	0.83	0.84
Si/Al	4.75	4.62	4.46	5.15	5.73	5.17	5.08	5.06	4.85

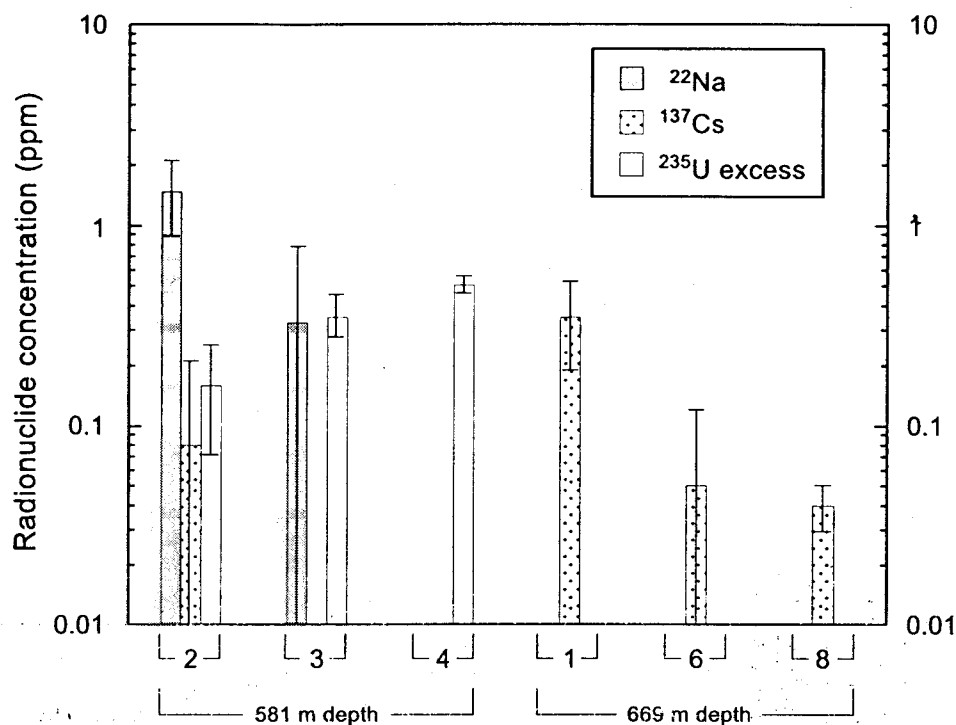


Figure 2: Bar graph showing the concentrations of radionuclides (in ppm) measured at six different spots in samples from ER-20-6 well #1. 1σ analytical error bars indicate relative uncertainties in the analyses. The sample from 581 m depth is from a prompt injection zone that lies above the water table. The 669 m sample is from the saturated zone.

the activities span 10 orders of magnitude due to large differences in the decay rates of different species (e.g. ^{22}Na has a half-life of 2.6 years whereas ^{235}U has a half-life of 7×10^8 years). The actual mass of material sputtered by the incident ion beam is estimated to be on the order of $\sim 5\text{-}10$ ng. Hence, the reported activity values provide an approximate indication of the radionuclide activity at the point of analysis. Note that reporting individual SIMS measurements in units of Bq/g results in anomalously high activities. For example, the SIMS results for ^{137}Cs scale up to values on the order of 10^5 to 10^6 Bq/g, whereas bulk gamma spectra measurements for ^{137}Cs (Table 1) indicate values of only 10^{-1} to 10^{-2} Bq/g. The per-gram difference in SIMS versus gamma spectra data for ^{22}Na is even larger. The large variance in these two types of measurements clearly highlights the heterogeneous distribution of radionuclides in these samples.

^{22}Na was detected only in the 581 m sample from the unsaturated zone. If ^{22}Na were present in groundwater at the 669 m level, significant sorption to the rock would be unlikely given the high solubility of sodium in groundwater (Hem, 1992). Alkali metals generally have high secondary ion yields during SIMS analysis, and the minimum counting system detection limit for sodium is ≤ 1 ppb. The largest ^{22}Na concentration that

was observed during this study is 1.48 ± 0.61 ppm. Although this value is several orders of magnitude above the counting system detection limit, the effective detection limit is related to uncertainties in the interference correction. The primary interference ($^{44}\text{Ca}^{++}$) was corrected from the measured $^{40}\text{Ca}^{++}$ ion intensity, in a manner analogous to that of equation (3). By increasing the mass resolution ($M/\Delta M$) of the instrument, it was also possible to separate the $^{44}\text{Ca}^{++}$ and the $^{22}\text{Na}^+$ peaks. Spots containing ^{22}Na were revisited using high mass resolving power in order to: 1) confirm the initial observation made at low mass resolving power, and 2) to test the use of a charge-coupled detector (CCD) for “mapping” radionuclide distributions. The CCD showed the presence of an irregular patch of ^{22}Na consisting of individual spots ≤ 5 μm in diameter. This technique may be used more extensively in future studies to produce images of the radionuclide distribution in a sample.

^{137}Cs is relatively widely distributed in the ER-20-6 samples, occurring in four of the six spots where radionuclides were detected. It was the only species observed in the 669 m sample, collected below the water table (Fig. 2). Cesium has an ion yield very similar to that of sodium (Wilson et al., 1989), and therefore has a minimum counting system detection limit near 1 ppb. However, quantitative determinations of low level ^{137}Cs were compromised by a strong interference from ^{137}Ba , requiring large interference corrections associated with large error bars. A potential mass interference related to the production of $^{121}\text{Sb}^+ + ^{16}\text{O}^+$ dimers was not treated because of the low sputtering efficiency for Sb^+ ions, and the presumed low concentration of Sb in the rock.

As was the case with ^{22}Na , “enriched” ^{235}U was observed only in the unsaturated zone (581 m depth). The low analytical errors associated with the ^{235}U measurements (Table 2) are related to a lack of isobaric interferences (other than natural ^{235}U). The minimum counting system detection limit for SIMS analyses of uranium is ~ 100 ppb. The presence of weapons-derived ^{235}U was verified by examining the $^{235}\text{U}/^{238}\text{U}$ ratios for these spots, which range from 0.0283 to 0.0218 – well above the natural $^{235}\text{U}/^{238}\text{U}$ ratio of 0.00725. To our knowledge, this is the first reported occurrence of weapons-derived actinides in a prompt injection zone. Although an attempt was made to look for ^{239}Pu in these samples, the interference associated with $^{238}\text{U} + ^1\text{H}$ prevented the quantitative determination of this species.

It is notable that several of the radionuclides sought during this study *may* have been present in the samples, but the analytical errors associated with their analyses were considered to be unacceptable. For example, “excess” mass 90 (possibly representing ^{90}Sr) was detected at several spots, but the mass correction for ^{90}Zr was sufficiently large that the propagated errors precluded the identification of ^{90}Sr . The possibility of making tritium measurements using SIMS is discussed separately later in this report.

Sample Mineralogy and Mineral Chemistry

X-ray diffraction analysis was used to determine the identity of individual minerals in the ER-20 samples. All three samples are predominantly composed of feldspar, quartz and zeolite minerals (heulandite and clinoptilolite). Petrographic analysis revealed that the volcanic glass comprising the rock matrix is extensively replaced by zeolites, and individual volcanic glass shards often have a glassy interior that is incompletely replaced by inward crystallizing clinoptilolite growth rings. Quantitative X-ray data indicates that 60% of ER-20-6 #1 (581 m) is composed of clinoptilolite (Warren, 1998). Similar zeolite mineral abundances (ranging from 54 to 75% of the rock mode) were found in samples returned from the 550-700 m depth interval of the BULLION emplacement hole.

Quantitative major element analyses of the zeolite-rich matrix were performed using the electron microprobe. The results of 9 analyses having analytical totals >79 weight percent are compiled in Tables 3a & 3b. "Spot" numbers represent individual analysis points, which are the same for both ion and electron microprobe analyses (see also Table 2). A majority of the spots have chemistries that are approximately consistent with clinoptilolite compositions [ideal formula: $(\text{Na}, \text{K}, \text{Ca}_{0.5}, \text{Ba}_{0.5}, \text{Mg}_{0.5})_6(\text{Al}_6\text{Si}_{30}\text{O}_{72}) \cdot \sim 20\text{H}_2\text{O}$; (Coombs et al., 1997)]. The structural formula of all zeolites necessitates $\text{Al} + \text{Fe} = \text{Na} + \text{K} + 2(\text{Ca} + \text{Mg})$. For six spots, this balance criteria is met to within 20%. Zeolites from both ER-20-5 and ER-20-6 have similar compositions, with Si/Al ratios clustering between 4.46 and 5.17. Figure 3 shows ratios of exchangeable cations in the ER-20 samples; the inset shows the same plot for clinoptilolite from Yucca Mountain, Nevada (Broxton et al., 1987). The ER-20 zeolites clearly show alkali enrichment relative to Ca + Mg, similar to the alkali-rich clinoptilolite compositions from Yucca Mountain. These exchangeable cation sites are likely to be important locations for the sequestration of radionuclides of similar size and charge.

The abundance of zeolites in the sample matrix appears to have strongly influenced the electron microprobe analytical totals, which were low for many samples. Zeolites have high water contents (up to ~20 wt %) that cannot be measured by the electron microprobe. Previous studies also reported low analytical totals due to sodium volatilization in zeolite-bearing rhyolites (Broxton et al., 1987; Sheppard et al., 1988). Low analytical totals may also be an artifact of the crater geometry left over from the ion probe analysis. The crater bottom created by depth profiling of the incident ion beam is uneven and may interfere with the generation of characteristic soft X-rays of the alkali metals. Finally, it is possible that the mineral oil used to lubricate the precision saw during sample preparation may have variably impregnated and contaminated the samples. Zeolite mineral analyses were accepted only if the structural formula balanced and analytical totals were in excess of 79 weight percent. This value is somewhat arbitrary, but is near the maximum value for the water content of zeolites.

To test the hypothesis that the low totals were due to sample preparation or ion probe cratering effects, polished thin sections were prepared from the same rock samples used

to prepare the epoxy mounted sections for ion microprobe analysis. The major element totals for electron microprobe analyses of zeolites were equivalent to the first set of measurements, indicating the low totals are most likely related to water content.

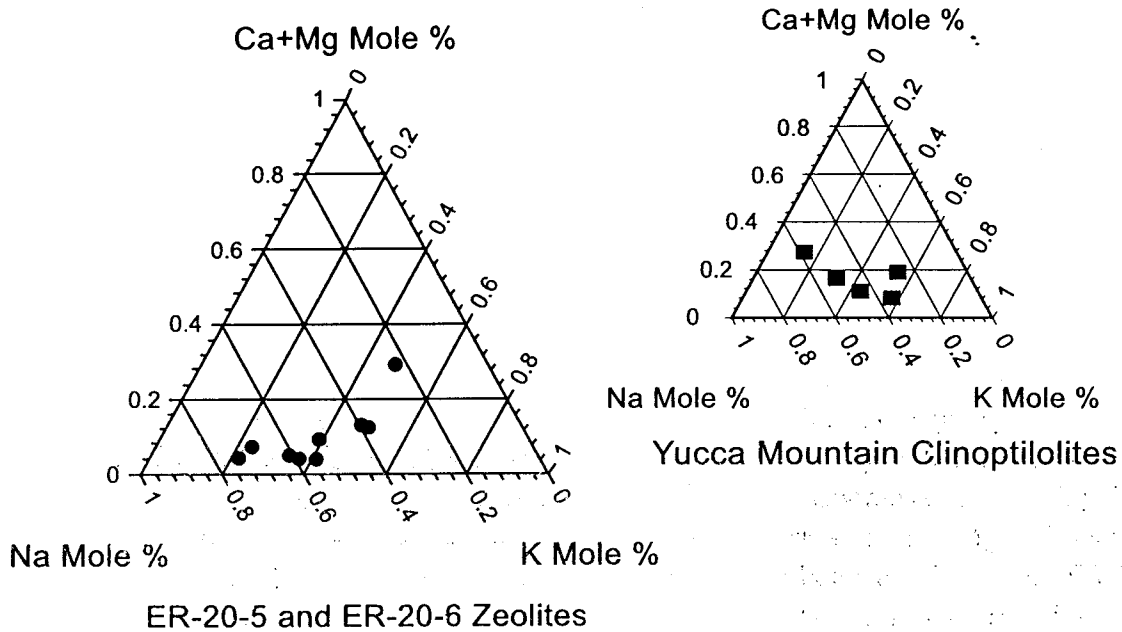


Figure 3: Tri-linear diagram showing the ratios of exchangeable cations in clinoptilolite- group minerals from the ER-20-5 and ER-20-6 boreholes. The inset shows a similar plot for clinoptilolites from Yucca Mountain, Nevada, reported by Broxton et al., (1987).

Discussion

Processes Influencing Radionuclide Distributions

Two distinct processes apparently influenced the distribution of radionuclides in the ER-20-6 samples: 1) the prompt injection of radionuclides at the time of the BULLION nuclear test, and 2) the sorption of radionuclides from groundwater. Whereas a prompt injection mechanism is unlikely for the 669 m sample, it provides a plausible explanation for the radionuclide distribution in the 581 m sample, which is situated 37 m above the water table.

During underground nuclear tests, fractures are both created and reactivated by the explosion. Conceptual models suggest the production and rapid displacement of high temperature and pressure gases and water vapor from the explosion enhance fracture growth (Smith et al., 1996). This expanding fluid is likely to facilitate the transport of radionuclides, which should fractionate during condensation according to their relative volatilities (Bedford & Jackson, 1965). It is notable that the results of this study indicate that species with vastly different volatilities (e.g. Na and U) may be deposited at precisely

the same location. This observation is consistent with “prompt fracture injection” models (Nimz & Thompson, 1992) wherein a quasi-homogeneous “plasma” produced by the detonation is rapidly injected along fractures. The spatial coexistence of species having different volatilities may suggest that condensation occurs under essentially closed-system conditions. Under these circumstances, the sorption capacity of the minerals present in the fracture is probably a second-order effect relative to the cooling history of the vapor phase.

Laczniak et al. (1996) note that water levels outside the detonation zone can increase by hundreds of feet following a nuclear test. In some cases, test-induced water level perturbations may persist for decades (Thordarson, 1987; Fenelon, 2000). The water level measured in the BULLION emplacement hole prior to testing was 621 m below the surface (Fenelon, 2000). Six years later, the water level in ER-20-6 #1 (166 m from ground zero) was 618 m, implying the water table had approximately returned to equilibrium. Although groundwater could have risen to the 581 m level immediately following the BULLION test, the restricted occurrence of radionuclides within only a 3 m interval of the unsaturated zone indicates that the “fluid” responsible for their deposition did not permeate the surrounding rock. Thus, if groundwater comprised an important component of this fluid, it apparently moved primarily along fractures.

^{137}Cs is the only radionuclide observed in the 669 m sample. The cesium is unlikely to have been directly deposited by prompt injection below the water table, particularly given that most ^{137}Cs is formed from the decay of short-lived gaseous fission precursors (principally ^{137}Xe and ^{137}I) (Smith et al., 1996). Hence, the ^{137}Cs in the 669 m sample was probably transported in groundwater following the nuclear test, and deposited by sorption processes. The sorption capacity of a rock is highly dependent on its constituent mineralogy. In the ER-20-6 core samples, zeolite minerals comprise a substantial proportion of the rock mode, and probably controlled ^{137}Cs sorption in the 669 m sample. Zeolites have large cation-exchange capacities due to structural features that are favorable to ion-exchange (Flanigan & Mumpton, 1977). Ion exchange of cesium with zeolite minerals has been documented in the literature (e.g. Ames, 1968; Mimura & Akiba, 1993; Rajec et al., 1998), and cesium is reported to have a strong affinity for sorption onto clinoptilolite (Ames, 1968).

The heterogeneous distribution of radionuclides in the ER-20-6 samples suggests that radionuclide deposition is controlled in part by the presence of micro-fractures in the rock, which permit the advective transport of fluids. Figure 4 is a SEM photomicrograph showing an ion microprobe crater (spot 2) in the 581 m sample, where ^{22}Na , ^{137}Cs , and ^{235}U were detected. Micron-size fractures are visible both within the crater, and in the surrounding matrix. At lower magnification, a distribution of fracture sizes is observed, with larger (5 to 20 μm wide) sub-parallel cracks occurring at ~ 1 mm intervals. Figure 5

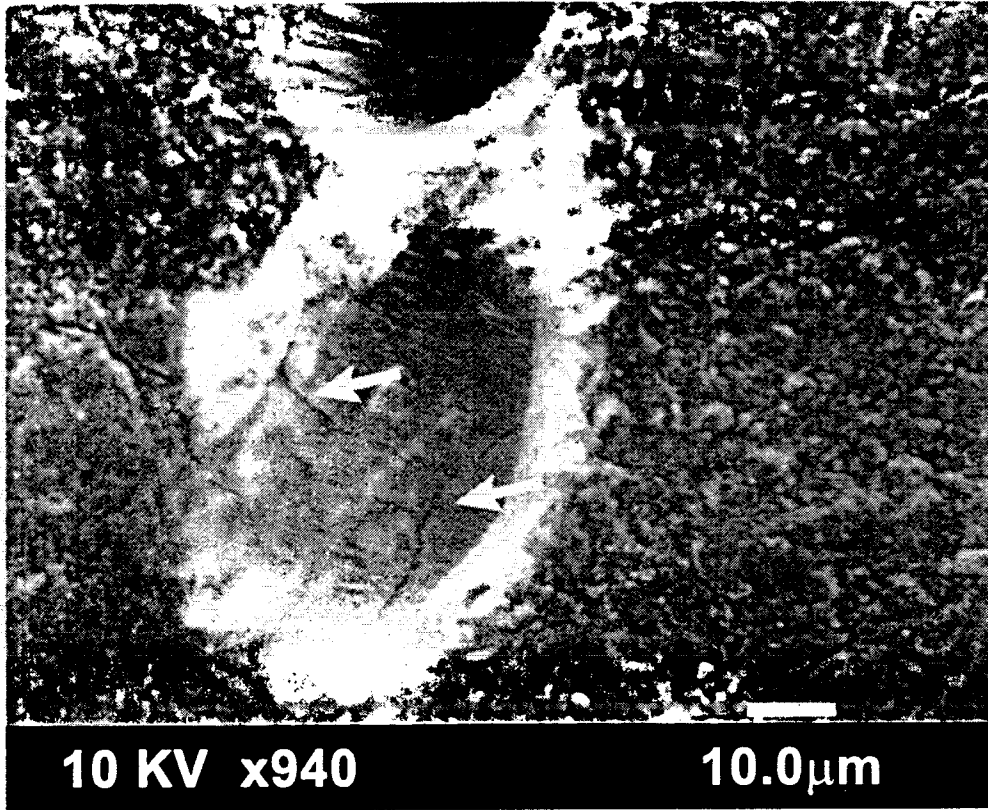


Figure 4: SEM photomicrograph of an ion microprobe crater (spot 2) in the ER-20-6#1 sample taken from 581 m below the surface. ^{22}Na , ^{137}Cs , and ^{235}U were all detected at this spot. Micron-size fractures are present both within the crater and in the surrounding matrix. These fractures may have helped facilitate radionuclide deposition in the sample. Scale bar is 10 μm .

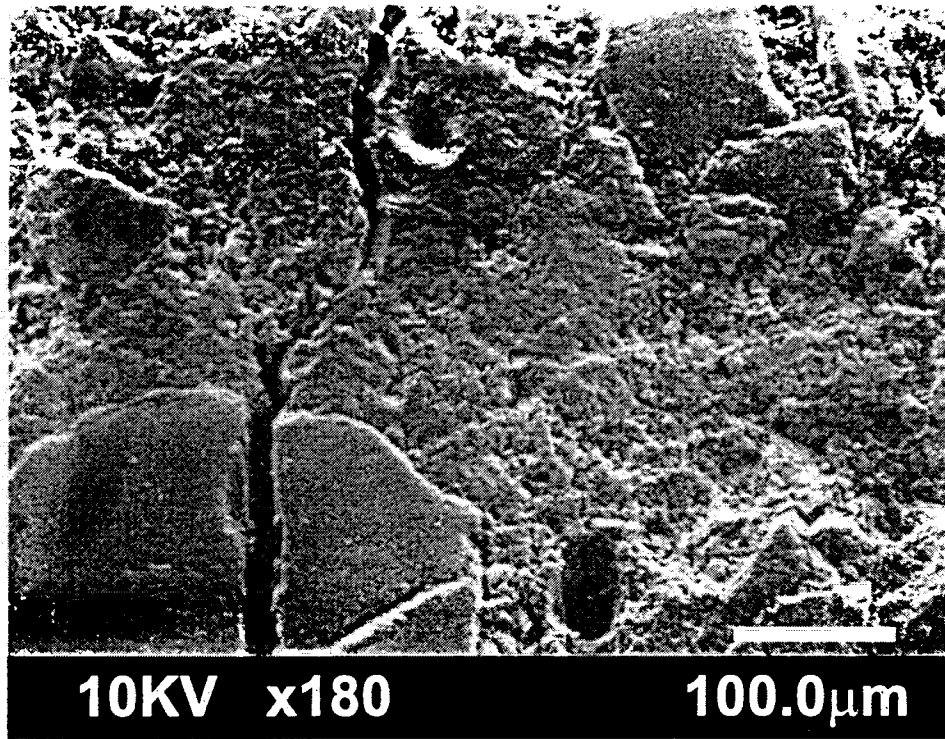


Figure 5: SEM photomicrograph of the 581 m sample illustrating the typical fracture pattern found in the ER-20 samples. Most of the granular matrix is composed of zeolitized volcanic glass. In general, radionuclides were observed in association with this type of matrix. The large grain in the lower left corner of the image is a feldspar crystal. Radionuclides were not detected in the ion probe crater located to the right of the feldspar grain. Scale bar is 100 µm.

shows one of these larger fractures, and illustrates the porous, granular texture of the rock. Petrographic thin-section analysis and electron microprobe results indicate the granular rock surface is largely composed of fine-grained zeolitized volcanic glass. The occurrence of radionuclides is highly correlated with this fractured, zeolitized matrix. Essentially identical conditions govern the radionuclide distribution in the 669 m sample, although the mean fracture density is lower.

Minerals along fractures are more likely to adsorb radionuclides than minerals within the bulk matrix, where diffusive transport mechanisms dominate. Moreover, the mineralogy of fracture-infillings may sometimes differ from that of the bulk mineralogy of the host rock, containing a higher proportion of "secondary" phases. This is particularly important with regard to the sorption of radionuclides from groundwater. Investigations of mineral-water interfaces emphasize the importance of excess free energy at mineral surfaces in controlling adsorptive interactions (Parks, 1990). For example, Lee & Jackson (1977) observed that ^{235}U is strongly adsorbed at "defects" on the surfaces of micaceous minerals (e.g. clays), particularly at steps along the edges of micaceous sheets. Mineral defect densities are likely to be highest along fractures, where individual mineral grains may be broken or exposed, enhancing the free surface area available for sorption.

SIMS Measurements of Tritium

The ion probe can reliably discriminate tritium (^3H) if the proper mass resolving power is used (Ross, 1994; Ottolini et al., 1995). During this study, ion microprobe analysis revealed a secondary ion signal above background at mass 3 in at least six spots within the ER-20 samples from the saturated zone. These ions have two potential sources: deuterium-hydrogen (DH) molecules and ^3H atoms. To unequivocally determine the source of the mass 3 ions, a tritium-implanted silicate glass reference standard is being developed. This material will permit the calibration of the instrument in order to distinguish DH from ^3H .

Although tritium is widely assumed to behave conservatively in groundwater, the common occurrence of zeolite minerals in the ER-20 samples suggests that partial tritium retention is plausible. Zeolites are characterized by an ability to lose and gain water molecules reversibly without changing their structure (Mumpton, 1977). Published data for the equilibrium isotope separation coefficient between tritiated water and synthetic zeolites suggests tritium is slightly enriched in the solid phase (Andreev & Polevoi, 1996). Tritium sorption was previously proposed to explain differences in observed and simulated breakthrough of ^3H associated with the pumped elution of radionuclides from an underground nuclear test cavity (Burbey & Wheatcraft, 1986).

Complimentary Aspects of SIMS and Bulk Radiochemical Analyses

One of the principal drawbacks of SIMS microanalysis is the difficulty in achieving representative sampling. As noted in section: *SIMS Analytical Results*, individual SIMS measurements cannot be extrapolated to yield meaningful average values. Moreover, if

the radionuclides had been uniformly dispersed in the samples examined during this study, it is unlikely that any of the species would have been detected. The average concentrations (as indicated by gamma spectroscopy) were simply too low. Although it is possible to set up automated SIMS runs wherein target species are analyzed at hundreds of points on a grid pattern, bulk radiochemical analyses still provide the best means of determining average concentrations. Nevertheless, SIMS data can compliment and extend the results from bulk analyses by providing comparative data at spot locations.

During this study, SIMS analysis provided insight into the correlated occurrence of different species, demonstrated the radionuclides were heterogeneously distributed, and revealed the significance of fracture-controlled deposition. The simple mineralogy of these samples precluded the evaluation of preferential uptake on selected phases. However, in samples containing multiple phases with high sorption capacities, SIMS microanalysis may allow the evaluation of competition between different sorption sites. This latter application may be well suited for laboratory studies of radionuclide sorption in mineralogically complex samples.

Conclusions

Models developed to predict the flux of radionuclides away from underground nuclear tests are greatly influenced by the presence and distribution clays, zeolites, and iron oxides and hydroxides in the near-field environment (Tompson et al, 1999). Microbeam analytical techniques provide spatial and compositional information on the controls and siting of radionuclides necessary to constrain and validate contaminant transport models. In this study, SIMS was used in tandem with electron microprobe analyses to determine the trace abundances of radionuclides at point locations in volcanic rock samples, and to identify the mineral compositions at these points. The radionuclides are heterogeneous in their occurrence within the samples, implying the distribution is affected in part by the presence of micro-fractures in the rock.

Two distinct processes apparently influenced the broad-scale distribution of radionuclides outside the nuclear test cavity: prompt injection, and sorption onto mineral surfaces. The prompt injection of radionuclides at the time of a nuclear test can emplace a diverse suite of radionuclides (including fission products, activation products, and residual nuclear fuel) distances of >150 m from the working point of the nuclear device. Evidence for this includes the observed coexistence of radionuclides with diverse volatilities at point locations, and the location of the injection zone above the water table. This study also documents the natural sorption of ^{137}Cs on zeolite minerals (clinoptilolite) in tuffaceous volcanic rocks from the groundwater-saturated zone.

One of the principal advantages of the SIMS technique is the ability to measure many species simultaneously at any given point, providing insight into correlated effects between different species. Drawbacks include the difficulty in achieving representative

sampling, and the fact that low abundance radionuclides are not readily detectable due to interfering masses. In some cases, increasing the mass resolution or using energy filtering techniques can help to increase abundance sensitivity. Work is in progress to develop a tritium-implanted reference standard to determine whether tritium mobility in groundwater is retarded by the exchange of water molecules with zeolite minerals. Our future applications of SIMS analyses to environmental radionuclide studies will focus also on using a charge-coupled detector (CCD) to provide images of the physical distribution of radionuclides within a sample.

Acknowledgments

We thank Ian Hutcheon, Adam Kent, and Ken Moody for valuable suggestions and guidance in preparing this paper. The manuscript was greatly improved by the comments of an anonymous reviewer. We also thank Rick Warren (Los Alamos National Laboratory) for performing the quantitative XRD analyses. This work was funded by the Underground Test Area (UGTA) project of the U.S. Department of Energy, Nevada Operations Office. The work was performed under the auspices of the U.S. Department of Energy by Lawrence Livermore National Laboratory under contract number W-7405-Eng-48.

References

- Ames, L.L. (1968) Cation exchange properties of heulandite-clinoptilolite series members. PNL Report BNWL-481-3, Pacific Northwest Laboratory, Richland, WA.
- Andreev, B.M., and Polevoi, A.S. (1996) Isotopic equilibrium of hydrogen in sorption of water by synthetic zeolites, silica gel, and alumina gel. *Radiochemistry*, v. 38, n. 2, p. 160-165.
- Beall, G.W., and Allard, B. (1981) Sorption of actinides from aqueous solutions under environmental conditions. In: *Adsorption from Aqueous Solutions* (P.H. Tewari, ed.), Plenum Press, New York, p. 193-212.
- Bedford, R.G., and Jackson, D.D. (1965) Volatilities of the fission product and uranium oxides. Lawrence Radiation Laboratory Report UCRL-12314, 216 p.
- Benninghoven, A., Rüdener, F.G., and Werner, H.W. (1987) *Secondary Ion Mass Spectrometry: Basic Concepts, Instrumental Aspects, Applications and Trends*. John Wiley and Sons, New York, 1264 p.
- Borg, I.Y., Stone, R., Levy, H.B., and Ramspott, L.D. (1976) Information pertinent to the migration of radionuclides in ground water at the Nevada Test Site. Lawrence Livermore National Laboratory Report UCRL-52078 Pt. 1, 216 p.
- Broxton, D.E., Bish, D.L., and Warren, R.G. (1987) Distribution and chemistry of diagenetic minerals at Yucca Mountain, Nye County, Nevada. *Clays and Clay Minerals* v. 35, n. 2, p. 89-110.
- Buddemeier, R.W., and Hunt, J.R. (1988) Transport of colloidal contaminants in groundwater: radionuclide migration at the Nevada Test Site. *Applied Geochemistry*, v. 3, p. 535-548.

- Buddemeier, R.W., Finkel, R.C., Marsh, K.V., Ruggieri, M.R., Rego, J.H., and Silva, R.J. (1991) Hydrology and radionuclide migration at the Nevada Test Site. *Radiochimica Acta*, v. 52/53, p. 275-282.
- Burbey, T.J. and Wheatcraft, S.W. (1986) Tritium and chlorine-36 migration from a nuclear explosion cavity. Desert Research Institute, Water Resources Center Publication 45050, Las Vegas, NV.
- Coombs, D.S., Alberti, A., Armbruster, T., Artioli, G., Colella, C., Galli, E., Grice, J.D., Liebau, F., Mandarino, J.A., Minato, H., Nickel, E.H., Passaglia, E., Peacor, D.R., Quartieri, S., Rinaldi, R., Ross, M., Sheppard, R.A., Tillmanns, E., and Vezzalini, G. (1997) Recommended nomenclature for zeolite minerals: Report of the Subcommittee on Zeolites of the International Mineralogical Association, Commission on New Minerals and Mineral Names. *Canadian Minerals*, v. 35, p. 1571-1606.
- Fenelon, J.M. (2000) Quality assurance and analysis of water levels in wells on Pahute Mesa and vicinity, Nevada Test Site, Nye County, Nevada. U.S. Geological Survey Water-Resources Investigations Report 00-4014, 68 p.
- Flanigan, E.M. and Mumpton, F.A. (1977) Commercial properties of natural zeolites. In: *Mineralogy and Geology of Natural Zeolites* (F.A. Mumpton, ed.) Rev. Mineralogy, vol. 4, Mineralogical Society of America, Washington, D.C., p. 165-175.
- Hem, J.D. (1992) Study and interpretation of the chemical characteristics of natural water, 3rd edition. U.S. Geological Survey Water-Supply Paper 2254, 263 p.
- Hinton, R.W., Harte, B., and Witt-Eickschen, G. (1995) Ion probe measurements of National Institute of Standards and Technology Standard Reference Material SRM 610 glass, trace elements. *Analyst*, v. 120, p. 1315-1319.
- Jedináková-Krizová, V. (1998) Migration of radionuclides in the environment. *J. of Radioanalytical and Nuclear Chemistry*, v. 229, n. 1-2, p. 13-18.
- Kersting, A.B., Efurud, D.W., Finnegan, D.L., Rokop, D.J., Smith, D.K., and Thompson, J.L. (1999) Migration of plutonium in ground water at the Nevada Test Site. *Nature*, v. 397, p. 56-59.
- Kim, J.I. (1991) Actinide colloid generation in groundwater. *Radiochimica Acta*, v. 52/53, p. 71-81.
- Laczniak, R.J., Cole, J.C., Sawyer, D.A., and Trudeau, D.A. (1996) Summary of hydrogeologic controls on ground-water flow at the Nevada Test Site, Nye County, Nevada. U.S. Geological Survey Water-Resources Investigations Report 96-4190, 59 p.
- Lee, S.Y. and Jackson, M.L. (1977) Surface charge density determination of micaceous minerals by ^{235}U fission particle track method. *Clays and Clay Minerals* v. 25, n. 4, p. 295-301.
- Levy, H.B. (1972) On evaluating the hazards of groundwater contamination by radioactivity from an underground nuclear explosion. Lawrence Livermore National Laboratory Report UCRL-51278, 23 p.
- Lieser, K.H. (1995) Radionuclides in the geosphere: sources, mobility, reactions in natural waters and interactions with solids. *Radiochimica Acta*, v. 70/71, p. 355-375.

- Lieser, K.H., Ament, A., Hill, R., Singli, R.N., Stingl, U., and Thybusch, B. (1990) Colloids in groundwater and their influence on migration of trace elements and radionuclides. *Radiochimica Acta*, v. 49, n. 2, p. 83-100.
- MacRae, N.D. (1995) Secondary-ion mass spectrometry and geology. *Canadian Mineralogist*, v. 33, p. 219-236.
- Metson, J. (1990) Secondary ion mass spectrometry. In: *Instrumental Surface Analysis of Geologic Materials* (D.L. Perry, ed.), VCH Publishers, New York, 1990, p. 311-352.
- Mimura, H., and Akiba, K. (1993) Adsorption behavior of cesium and strontium on synthetic zeolite P. *Journal of Nuclear Science and Technology*, v. 30, n. 5, p. 436-443.
- Mumpton, F.A. (1977) Natural zeolites. In: *Mineralogy and Geology of Natural Zeolites* (F.A. Mumpton, ed.) *Rev. Mineralogy*, vol. 4, Mineralogical Society of America, Washington, D.C., p. 1-17.
- Nicolescu, S., Cornell, D.H., Södervall, U., and Odelius, H. (1998) Secondary ion mass spectrometry analysis of rare earth elements in grandite garnet and other skarn related silicates. *European Journal of Mineralogy*, v. 10, p. 251-259.
- Nimz, G.J., and Thompson, J.L. (1992) Underground radionuclide migration at the Nevada Test Site. U.S. Department of Energy Report DOE/NV-346, 10 p.
- Nitsche, H., Müller, A., Standifer, E.M., Deinhammer, R.S., Becraft, K., Prussin, T., and Gatti, R.C. (1992) Dependence of actinide solubility and speciation on carbonate concentration and ionic strength in groundwater. *Radiochimica Acta*, v. 58/59, p. 27-32.
- Ottolmi, L., Bottazzi, P., Zanetti, A., and Vannucci, R. (1995) Determination of hydrogen in silicates by secondary ion mass spectrometry. *Analyst*, v. 120, n. 5, p. 1309-1313.
- Parks, G.A. (1990) Surface energy and adsorption at mineral/water interfaces: an introduction. In: *Mineral-Water Interface Geochemistry* (M.F. Hochella, A.F. White, eds.). *Rev. Mineralogy*, vol. 23, Mineral. Soc. Amer., Washington D.C., pp. 133-175.
- Patera, E.S., Hobart, D.E., Meijer, A., and Rundberg, R.S. (1990) Chemical and physical processes of radionuclide migration at Yucca Mountain, Nevada. *J. of Radioanalytical and Nuclear Chemistry*, v. 142, n. 1, p. 331-347.
- Rajec, P., Macášek, F., Féder, M., Misadlides, P., and Šamajová, E. (1998) Sorption of caesium and strontium on clinoptilolite- and mordenite-containing sedimentary rocks. *Journal of Radioanalytical and Nuclear Chemistry*, v. 229, p. 49-55.
- Ross, G.G. (1994) Analysis of hydrogen isotopes in materials by secondary ion mass spectrometry and nuclear microanalysis. *Vacuum*, v. 45, n. 4, p. 375-387.
- Sheppard, R.A., Gude, A.J., and Fitzpatrick, J.J. (1988) Distribution, characterization, and genesis of mordenite in Miocene silicic tuffs at Yucca Mountain, Nye County, Nevada. *U.S. Geological Survey Bulletin* 1777, 22 p.

- Shimizu, N., Semet, M.P., and Allègre, C.J. (1978) Geochemical applications of quantitative ion-microprobe analysis. *Geochimica et Cosmochimica Acta*, v. 42, p. 1321-1334.
- Silva, R.J. and Nitsche, H. (1995) Actinide environmental chemistry. *Radiochimica Acta*, v. 70/71, p. 377-396.
- Smith, D.K. (1998) A recent drilling program to investigate radionuclide migration at the Nevada Test Site. *Journal of Radioanalytical and Nuclear Chemistry*, v. 235, n 1-2, p. 159-166.
- Smith, D.K., Nagle, R.J., and Kenneally, J.M. (1996) Transport of gaseous fission products adjacent to an underground nuclear test cavity. *Radiochimica Acta*, v. 73, n. 4, p. 177-183.
- Stumm, W. and Morgan, J.J. (1981) *Aquatic Chemistry*, 2nd ed., John Wiley and Sons, New York, 780 p.
- Thompson, J.L. (1991) Radionuclide migration studies at the Nevada Test Site. *Radiochimica Acta*, v. 54, p. 149-154.
- Thordarson, W. (1987) Hydrogeology of the Faultless site, Nye County, Nevada. U.S. Geological Survey Water-Resources Investigations Report 86-4342, 40 p.
- Ticknor, K.V., Kamineni, D.C., and Vandergraaf, T.T. (1991) Flow path mineralogy: its effect on radionuclide retardation in the geosphere. *Material Research Society Symposium Proceedings*, v. 212, p. 661-668.
- Tompson, A.F.B., Bruton, C.J., and Pawloski, G.A. (1999) Evaluation of the hydrologic source term from underground nuclear tests in Frenchman Flat at the Nevada Test Site: the CAMBRIC test. Lawrence Livermore National Laboratory Report UCRL-ID-132300, 355 p.
- U.S. Congress, Office of Technology Assessment (1989) *The Containment of Underground Nuclear Explosions*. OTA-ISC-414, U.S. Government Printing Office, Washington, DC.
- U.S. Department of Energy, Nevada Operations Office (1994) *United States Nuclear Tests, July 1945 through September 1992*. Report DOE/NV-209 (Rev. 14), 38 p.
- Warren, R.G. (1998) unpublished results. Los Alamos National Laboratory, Los Alamos, NM.
- Wilson, R.G., Stevie, F.A., and Magee, C.W. (1989) *Secondary Ion Mass Spectrometry: A Practical Handbook for Depth Profiling and Bulk Impurity Analysis*. John Wiley and Sons, New York, 385 p.
- Zinner, E., and Crozaz, G. (1986) A method for the quantitative measurement of rare earth elements in the ion microprobe. *International Journal of Mass Spectrometry and Ion Processes*, v. 69, p. 17-38.

— Chapter 5 —

Quadrupole ICP-MS and Multi-Collector ICP-MS: Nevada Test Site Applications

Jean E. Moran

Introduction

Inductively coupled plasma mass spectrometry (ICP-MS), using both quadrupole (QICP-MS) and sector field (MC-ICP-MS) mass analyzers, is seeing increased use in routine environmental and specialized analytical applications. Groundwaters are routinely analyzed for both major and trace metals to a high precision and accuracy using ICP-MS. In addition to the ability to complete rapid, multi-element analyses, the major advantage of using an ICP-MS over competing technologies is the flexibility in sample introduction methods that include various nebulization processes. Some recent reviews of ICP-MS applications can be found in Jarvis et al. (1992), Jakubowski et al. (1998), Halliday et al. (1998), and Eggins et al. (1997).

Groundwater samples from the Nevada Test Site (NTS) present a particular challenge for analysis by ICP-MS due to total dissolved solids (TDS) in the groundwater, which range in concentration from 0.01 up to 1 part per thousand. Samples with high TDS concentrations are transported less efficiently by the sample introduction system of the ICP-MS and they have different ionization efficiencies relative to standards used to calibrate the apparatus. For most major and some trace element analyses, this is circumvented by diluting the samples 10 to 1000 fold before analyzing them, since diluting the samples reduces the concentration of TDS in the samples thereby increasing the ionization efficiencies. In addition, dilution reduces the effect of polyatomic isobars (produced when atoms from the sample and the plasma gas combine at the same mass as a given analyte) by reducing space charge effects in the plasma source. Furthermore, quantitation through the use of internal standards can improve the quality of the resultant data by compensating for matrix effects (Eggins et al., 1997), such as differences in transport in the nebulizer or interface. However, many elements and isotopes that are possible contaminants in NTS groundwaters are present at such low concentrations, that dilution can not be used as a means for compensating for matrix effects. This introduces an entire new set of difficulties that can be treated by consideration of any potential interfering isobars, methods to pre-concentrate the samples, and instrument options for maximizing sensitivity for each analyte.

This paper is divided into four sections according to the analyte(s) being discussed. The first and second sections describe use of QICP-MS for analysis of low level actinides under specially optimized conditions, in particular Np and Pu. The third and fourth sections outline the use of an MC-ICP-MS for the determination of isotope ratios of U, Sr, and I in NTS groundwater samples. These techniques represent relatively recent

developments in plasma mass spectrometry. As use of this instrumentation at facilities doing fission product and actinide-based research becomes more commonplace, the applications described here are certain to grow in number.

²³⁷Np Concentrations in NTS Waters by QICP-MS

Background

Of the actinides potentially present in NTS groundwaters, ²³⁷Np is unique since it has no significant molecular isobars when measured by QICP-MS. Mass 237 is also the only isotope of significant abundance. Therefore, a method was developed to measure Np in whole (unfiltered) groundwater samples by QICP-MS that required no chemical sample preparation, other than acidification using high purity nitric acid (HNO₃).

Experimental

Measurements were made using a Hewlett-Packard model 4500 QICP-MS. The instrument parameters for trace level actinide determination are as follows:

Plasma gas flow rate	16.0 L/min
Aux. Gas glow rate	0.95 L/min
Carrier gas flow rate	1.10 L/min
RF power	1228 W
Nebulizer	PEEK, Babington-type
Spray chamber temp.	1 C
Sample uptake rate	0.5 mL/min
Sampling depth	12.1 mm
Masses	103, 209, 235-238
Points/Mass	3
Integration Time/mass	60 s (236-238)
Replicates	3
Total acquisition time/sample	550 s
Interface	shield torch

Under normal operating conditions, the sensitivity of the instrument is approximately 30 MHz/ppm. Under the operating conditions listed above, and after optimizing the lens system, the sensitivity is increased to 85 MHz/ppm. It should be noted that the essential difference from standard operating conditions is the use of the shield torch while maintaining a high forward power and standard gas flow rates---which keeps the plasma "hot." By keeping the plasma hot, the ionization efficiency, especially for heavy elements, is maximized.

Instrument calibration was done by using a NIST-traceable ²³⁷Np solution with a stock solution concentration of 0.834 ± 0.009 ng/ml. Six standards with concentrations 0, 0.8, 2.1, 4.2, 8.3, and 16.4 ppt (pg/ml) were used for the calibration. The standards were prepared immediately before analysis, and two internal standards (Rh and Bi) were

monitored at the 1 ppb level--but were not used in quantification of sample concentrations. The detection limit was calculated using three times the standard deviation of seven analyses of the zero concentration standard (blank).

Results

The detection limit for ^{237}Np is 0.8 ppt. The calculated correlation coefficient of 0.9993 demonstrates the excellent linearity of the calibration line. Close examination of ^{237}U and ^{238}U peaks from the water sample analyses reveal that the U tail did not interfere at a level significantly higher than the background level. Great care must be taken in the tuning of the peak shape, as broadened peaks will result in U tailing into the mass 237 peak. The very high concentration of ^{238}U in sample GCP20501 may have caused a U tail in the mass 237 range. A concentration of 1.1 ppt ($\pm 3.4\%$) was determined for sample GCP20501, however, these results must be confirmed on a chemically separated sample, due to the possibility of U tailing. Two other samples, GCP20519A and GCP20519B were below the detection limit. However, these two samples (GCP20519A and GCP20519B) were spiked Np standard material at 5 ppt and spike recovery was approximately 90%, suggesting that this technique is appropriate for low level Np measurement in untreated groundwater.

Measurement of Pu concentration and Pu isotopes by QICP-MS

Background

NTS groundwater presents a particular challenge in doing QICP-MS analyses since it can contain relatively high U concentrations, while having very low Pu concentrations. Formation of U hydride (mass 239) makes doing QICP-MS analyses for Pu problematic, since formation of Pu hydride under wet plasma conditions generally precludes measurement of Pu in samples that have not been chemically separated. Some tests were carried out to determine the level of hydride generation, and the performance of the Hewlett-Packard model 4500 QICP-MS at LLNL by using the shield torch and hot plasma on Pu standards.

Experimental

The instrument parameters for the QICP-MS are the same as those described above for trace Np measurements; but the masses being monitored in this case are 238-242. The level of hydride generation was determined by running a 10 ppb U standard, and monitoring mass 237 (no molecular isobar expected) and mass 239 (only U hydride formation is expected). The instrument background is then determined by analyzing the "dry" plasma (no solution introduced into the plasma). The hydride generation level was $\sim 7 \times 10^{-5}$ of the U signal, or 0.7 ppt on the 10 ppb standard solution. As previously mentioned, since U concentrations of NTS groundwater samples are typically high, measurement of Pu by QICP-MS is not possible without doing a chemical separation of the Pu from the U. This separation was made by first digesting the samples in 50% high purity HNO_3 . The solution was then loaded onto TEVA resin. Hydroiodic acid (HI) was added to reduce Pu to the +3 state, with the expectation that this would cause the Pu to

pass through the resin. Since the U has a different charge state than the reduced Pu, it will adhere to (rather than passing through) the resin. Poor recovery from these samples (<10% as measured on the 242 spikes) indicated that additional HCl was needed to prevent HI from becoming I₂ since this will decrease the amount of Pu being reduced to the +3 state. Development work on the separation chemistry is continuing in order to improve the amount of U recovery from these water samples.

Calibration and detection limits were determined using a NBS traceable Pu standard. The composition of this standard is shown in Table 1.

Table 1: Compositions of the NBS traceable Pu standard used in this study.

Pu Standard	Composition (ng/mL)
²³⁸ Pu	4.14 x 10 ⁻⁵
²³⁹ Pu	1.165 ± 0.012
²⁴⁰ Pu	3.37 x 10 ⁻²
²⁴¹ Pu	3.26 x 10 ⁻⁴
²⁴² Pu	7.28 x 10 ⁻⁵

Results

For the sake of comparison between the QICP-MS analyses and more widely accepted analytical methods, quantities of the chemically separated Pu oxide were analyzed using the QICP-MS, high-resolution gamma (γ) counting, and thermal ionization mass spectrometry (TIMS). For the QICP-MS, the detection limit at mass 239 was 0.9 ppt and the one sigma (σ) precision of the mass ratio 239/240 was 2%, while the total Pu consumed for each analysis was 5 ng. The results for this sample are shown in Figure 1. In addition, a separation chemistry using anion exchange resin (AG-8) was attempted on a blank consisting of acidified deionized (DI) water, a blank containing a ²⁴²Pu spike, two NTS groundwater samples, and a spiked NTS groundwater sample. The results of the comparison (Fig. 1; Table 2) indicate that the QICP-MS shows definite promise for both chemically separated samples and for samples with low natural U concentrations, since agreement is good, but sample preparation and analysis time are significantly less.

U and Sr isotopic ratios using a MC-ICP-MS

Background

Historically, U and Sr isotope measurements of NTS groundwater were made by TIMS. However, the MC-ICP-MS offers an excellent alternative to TIMS for determination of high precision U and Sr isotope ratios, since it offers advantages over TIMS technology.

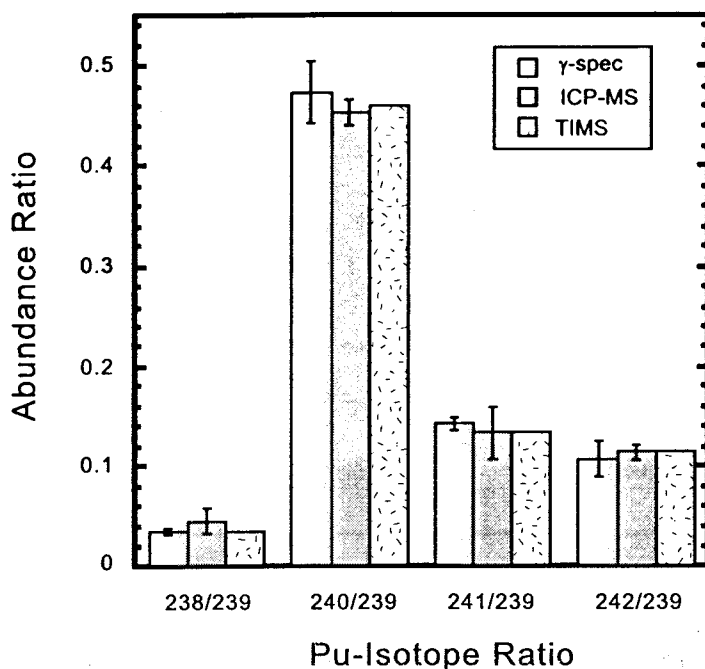


Figure 1: Graphical representation of Pu isotope data comparison. These data represent an internal sample prepared in the lab, and are not representative of NTS cavity or ground water. Error bars are $\pm 1\sigma$.

Table 2: Low level Pu determination---comparison of three techniques.

Isotope Ratio	γ-spectrometry	ICP-MS	TIMS
$^{238}\text{Pu}/^{239}\text{Pu}$	0.0345 ± 0.0020	0.046 ± 0.012	0.03431 ± 0.00018
$^{240}\text{Pu}/^{239}\text{Pu}$	0.474 ± 0.030	0.453 ± 0.013	0.4602 ± 0.0024
$^{241}\text{Pu}/^{239}\text{Pu}$	0.1439 ± 0.0066	0.133 ± 0.026	0.13530 ± 0.00068
$^{242}\text{Pu}/^{239}\text{Pu}$	0.108 ± 0.017	0.1146 ± 0.0070	0.11583 ± 0.00058

The most important advantage of the MC-ICP-MS is the plasma source, which allows solutions to be introduced directly into the mass spectrometer (MS). This direct introduction of samples allows groundwaters with relatively high concentrations of U and Sr to be measured without any sample preparation.

Experimental

Measurements were made using a VG Plasma 54 MC-ICP-MS, equipped with a standard, Meinhardt-type nebulizer. For the $^{234}\text{U}/^{238}\text{U}$ and $^{235}\text{U}/^{238}\text{U}$ analyses, the Daly detector was positioned to measure masses 234 and 235; and 238 was measured on a high-end Faraday cup. Approximately 35 ng U was consumed during each analysis. All

measurements were calibrated against a pair of NIST U500 standards. Two analyses of both U010 and U020 standards were made following the sample analyses, and were used to give an indication of reproducibility and accuracy.

Results

The NTS groundwater samples in Table 3 were measured without any sample preparation, besides routine filtering (0.45µm) and acidification with HNO₃. However, results for a 234/238 sample that was separated using UTEVA resin is included (Table 4).

Table 3: U isotope results from MC-ICP-MS for untreated NTS groundwaters.

Sample Name	235/238 Daly Detector		234/238 Daly Detector	
	Mean	Std Error	Mean	Std Error
<u>Corrected Data</u>				
GCP20505 (n=1)	0.00722	0.33	0.000171	1.91
Ave GCP20519	0.00734		0.000218	
Std Deviation	0.00027		0.000004	
%RSD	3.5		2.0	
n = 2				
Ave GCP20501	0.00719		0.000159	
Std Deviation	0.00008		0.000004	
%RSD	1.1		2.1	
n = 2				

For the ⁸⁷Sr/⁸⁶Sr analysis, the detectors on the MC-ICP-MS were set with mass 85 on the axial Daly detectors, and masses 86, 87, and 88 on the high-end Faraday cups. A complicating factor in making accurate Sr ratio measurements are an isobar introduced by impurities in the Ar gas stream used to generate the plasma, and an isobar from Rb in the sample. For example, Rb has a major isotope at mass 87, while Kr has a major isotope at mass 86. The multi-collector allows simultaneous monitoring of these masses, so that corrections to the 87/86 ratio can be made. A 100 ppb NIST ⁸⁷Sr/⁸⁶Sr standard was used for calibration. A correction for the Rb that was detected during the standard analysis

was then made based on both: a) the intensity of Rb measured at mass 85, and b) the sum of the intensity measured at mass 87 (Rb+Sr). In addition, a correction was made to account for mass fractionation. A single sample of NTS groundwater was then analyzed (Table 5), with a total of approximately 100 ng of Sr consumed in the analysis. It should be noted that relative to the large Sr ion beam generated by the sample (GCP20542), the Kr interference was insignificant.

Table 4: Result for NTS groundwater sample after U separation chemistry

Sample Name	Mean (234/238)	Std Error	Total U current (nanoamps)
GCP20542	0.000162	1.25	0.0055
GCP20542	0.000167	1.44	0.0055
Average	0.000165		0.0055

Table 5: Result of the Sr analysis.

Sample Identification	$^{87}\text{Sr}/^{86}\text{Sr}$
<u>Corrected Data</u>	
Ave GCP20542	0.7126
Std Deviation	0.0066
RSD%	1%
n = 3	

 $^{129}\text{I}/^{127}\text{I}$ Measurement by MC-ICP-MS**Background**

The long-lived isotope of iodine, ^{129}I , is an extremely useful isotope for studying NTS hydrologic systems. As a direct fission product, ^{129}I has a high abundance relative to natural concentrations in contaminated water from NTS, and is extremely mobile in reduced groundwater. Furthermore, its long half-life and tendency to concentrate in the human thyroid make it an important component of long-term dose assessment.

Due to the high counting efficiency and lack of molecular isobars inherent in accelerator mass spectrometry (AMS), which result in superior accuracy and very low detection limit (10^{-14}) for both anthropogenic and pre-anthropogenic ^{129}I levels, measurements of $^{129}\text{I}/^{127}\text{I}$ ratios are typically made using AMS. However, there are significant constraints to using this method that include both the high financial cost of AMS analyses, and the effort involved in preparing each sample for analysis. Therefore, these constraints have severely limited the routine application of $^{129}\text{I}/^{127}\text{I}$ ratios to hydrologic problems.

For measurement of $^{129}\text{I}/^{127}\text{I}$ at anthropogenic levels in hydrologic systems, MC-ICP-MS offers an important and under-utilized alternative to AMS. By allowing solutions to be analyzed directly, avoiding lengthy sample preparation times, sample throughput is greatly enhanced making MC-ICP-MS analyses much more cost effective. In addition, the detection system offers a high precision ratio determination making the resulting

analyses potentially more precise (1%) than those by AMS (routinely 10%). There are some complicating factors in using MC-ICP-MS for iodine analysis however. These factors include the relatively poor ionization efficiency of iodine (about 20%, compared to 95% for most metals), and the interference caused by the competing mass from ^{129}Xe . ^{129}Xe is present in the Ar gas stream used to generate the plasma, and can also occur naturally as a dissolved gas in groundwater.

Experimental

In order to make iodine isotope measurements on the MC-ICP-MS, the detector array on the multi-collector was set up with 129 on the axial Daly detector. Mass 127 was detected on the low #1 Faraday (L1), while the high-side Faradays H1, H2, H3 and H4 were used to detect Xe isotopes at masses 131, 132, 134, and 136 respectively. Sample solutions containing dissolved potassium iodide salt (KI) were sparged immediately before analysis to remove xenon present in the solution. Sparging was accomplished by bubbling gaseous nitrogen in the sample solution for several minutes. Both wet and dry plasmas were then examined.

Results

For a solution concentration of 100 ppb of iodide, a beam of about 700 femptoamps (fA) is generated. This corresponds to a count rate of about 50 MHz/ppm. The Xe at mass 132 (27% abundance) generates a beam of ~1.4 fA. The indicated $^{129}\text{I}/^{127}\text{I}$ detection limit for the analyses was 1×10^{-3} . If complete removal of Xe were made possible, the detection limit could be greatly lowered to 1.0×10^{-8} . This lower detection limit would allow fast, precise analysis of many NTS groundwater samples since typical ratios for affected waters are in the 1.0×10^{-5} to 1.0×10^{-7} range.

Since sparging the sample immediately prior to analysis results in only a 20% reduction in Xe, the remaining xenon present is being introduced by the Ar stream used to generate the plasma. Examination of the peak patterns for wet versus dry plasmas clearly illustrates that the source of interference at mass 129 is Xe from the "high purity" Ar stream (Fig. 2). Even though one possible solution to this problem would be to place a chilled charcoal trap on the Ar stream (Xe and Ar freeze at different temperatures causing the Xe to be removed by freezing it onto the charcoal while allowing the Ar to pass through freely), there is a new technique that could be used to remove Xe called a "collision cell." By bleeding a small amount of oxygen gas (O_2) into the Ar stream in the collision cell, Xe is eliminated by combining with the O_2 , and mass 129 is thus free of isobaric interferences from Xe. It is important to note that LLNL has recently acquired the next generation of MC-ICP-MS, equipped with collision cell technology. This makes development work for ^{129}I analyses by MC-ICP-MS possible, and this development work is currently in progress.

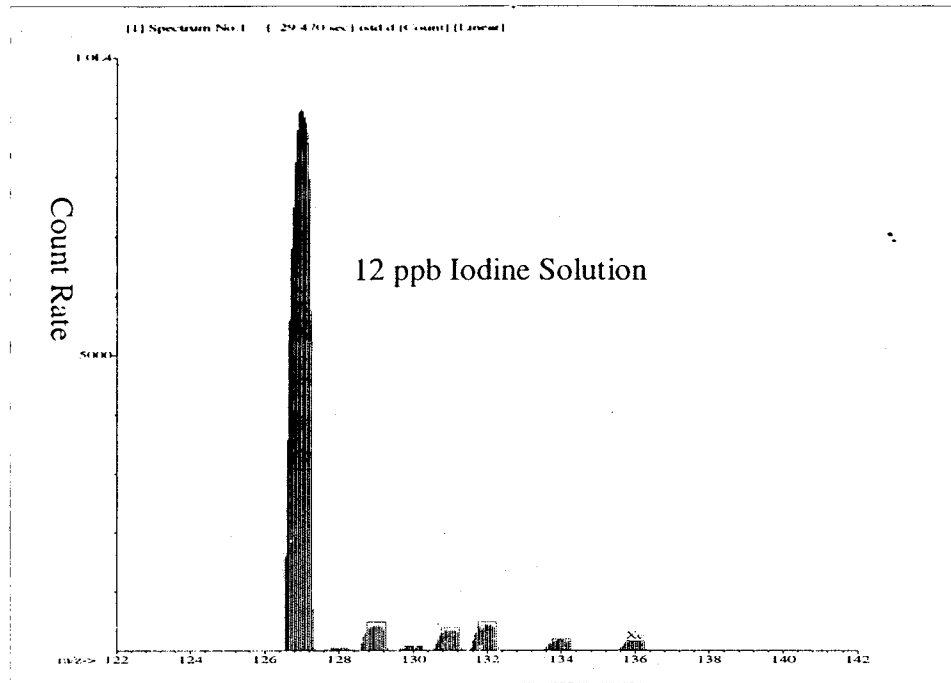


Figure 2: Count rate versus mass for a 12 ppb iodine standard, sparged immediately prior to analysis. Relative abundances at other masses confirm that Xe is present in the plasma gas.

Conclusions

For this study, quadrupole ICP-MS and multi-collector ICP-MS were used to make elemental and isotopic measurements on groundwater from the NTS. Several examples, including low-level actinide concentration measurements, and high precision U and Sr isotope ratios are illustrated here. These technologies offer significant advantages over thermal ionization mass spectrometry, counting methods, and accelerator mass spectrometry---most important being the great reduction in necessary sample preparation. Other advantages are smaller sample volumes, and higher sample throughput, which in turn lead to lower cost, and to the possibility of applying these isotope systems on a larger scale, to solve the most critical issues regarding radionuclide transport at the NTS. Further research is currently being developed for analytical methods that will allow fast, precise measurement of key isotopes in both water and glass samples.

References

Eggins, S.M., Woodhead, J.D., Kinsley, L.P.J., Mortimer, G.E., Sylvester, P., McCullough, M.T., Hergt, J.M. and Handler, M.R. (1997) A simple method for the precise determination of >40 trace elements in geological samples by ICPMS using enriched isotope internal standardisation. *Chemical Geology*, v. 134, p. 311-326.

- Halliday, A.N., Lee, D-C, Christensen, J.N., Rehkamper, M., Yi, W., Luo, X., Hall, C.M., Ballentine, C.J., Pettke, T., and Stirling, C. (1998) Applications of multiple collector ICPMS to cosmochemistry, geochemistry, and paleoceanography. *Geochimica et Cosmochimica Acta*, v. 62, no. 6, p. 919-940.
- Jakubowski, N., Moens, L., and Vanhaecke, F. (1998) Sector field mass spectrometers in ICP-MS. *Spectrochimica Acta Part B*, v. 53, p. 1739-1763.
- Jarvis, K.E., Gray, A.L., and Houk, R.S. (1992) *Handbook of Inductively Coupled Plasma Mass Spectrometry*, Blackie, London, 443 p.
- Yamasaki, S.I., Tsumura, A., and Tkaku, Y. (1994) Ultratrace elements in terrestrial water as determined by high-resolution ICP-MS. *Microchemical Journal*, v. 49, p. 305-318.

— Chapter 6 —

Lithologic, Mineralogic, and Petrographic Characterization of Alluvium from the U-1a 102C and 102D Drifts of the U-1a Tunnel Complex, Nevada Test Site

Timothy P. Rose, David K. Smith, and J. Kent Werner, Jr.*

Summary

This report describes the lithology, mineralogy and petrology of alluvium samples from the 102C and 102D drifts of the U-1a tunnel complex, located ~300 m beneath the surface of Yucca Flat, in Area 1 of the Nevada Test Site. The objective of this study is to provide detailed information on the geologic characteristics of the alluvium in Yucca Flat for the purpose of developing radionuclide transport models for the unsaturated zone. Emphasis is placed on evaluating the mineralogy of the fine-grained matrix, which is likely to contain the greatest abundance of minerals that affect radionuclide migration.

The U-1a alluvium is composed of moderately to poorly sorted sands and gravels representing channel fill and slope-wash sediments transported by ephemeral streams from the surrounding highlands. The deposits are a heterogeneous mixture of detritus derived from Tertiary volcanic rocks and Paleozoic carbonate and clastic sediments. The dominant mineral constituents of the bulk rock are quartz, feldspar, calcite, dolomite and clays. Other minerals include iron oxides, biotite, muscovite, clinocllore, and hornblende. Clay minerals, detrital crystal fragments, and sand-sized lithic fragments comprise the majority of the fine-grained matrix. The clays commonly form banded or matted textures that suggest an authigenic origin. X-ray diffraction and semi-quantitative energy dispersive spectra analyses suggest kaolinite is the dominant clay mineral, although smectite is widespread in lower abundance. The clays are frequently associated with fine-grained secondary calcite and disseminated iron oxide minerals. Zeolite minerals were not observed in the matrix. Carbon isotope ($\delta^{13}\text{C}$) analyses indicate the secondary calcite is derived from two sources: dissolved bicarbonate in groundwater, and weathered Paleozoic carbonate clasts. Oxygen isotope ($\delta^{18}\text{O}$) measurements of the calcites indicate they formed from evaporating groundwater under ambient conditions.

Introduction

The Yucca Flat alluvial basin was the location of 661 underground nuclear tests, approximately two-thirds of which had working points more than 5 cavity radii above the water table (Laczniak et al., 1996). Given that the annual precipitation rate in Yucca Flat averages less than 18 cm yr^{-1} (French, 1986), the rate at which the “unsaturated” radiological source term is transported downward to the water table is expected to be

* United States Naval Academy, P.O. Box 14693, Annapolis, MD 21412

slow. Nevertheless, concerns have been raised regarding the possibility of radionuclide transport due to enhanced recharge along nuclear subsidence craters (Tyler et al., 1992; Pohll et al., 1996). Significant infiltration of surface water in Yucca Flat is known to occur along deep fractures associated with nuclear detonations and geologic faults (e.g. Kao et al., 1994). However, the extent to which this seepage affects the unsaturated test cavity environment is not known.

The development of predictive models for radionuclide transport in the unsaturated zone will require an understanding of the processes that facilitate radionuclide release, as well as those processes that enhance or abate transport. With regard to the latter, the mobilities of many dissolved radionuclides are significantly attenuated by sorption processes (e.g. Wolfsberg, 1978; Benedict et al., 1997). However, the effectiveness of this process depends in large part on the mineralogical composition of the host rock surrounding a nuclear test cavity. Certain minerals are known to have a high affinity for radionuclide sorption, including clays, iron oxides and zeolites. Hence, the characterization of geologic materials present in the unsaturated zone is one of the necessary components of model development.

This report describes the lithology, mineralogy, and petrographic characteristics of geologic samples collected from the U-1a horizontal drift complex, located in Area 1 of the Nevada Test Site (NTS). The U-1a (formerly LYNER) complex affords a unique opportunity to study the *in situ* compositional variations of alluvium nearly 300 meters below the surface of Yucca Flat. In this study, particular emphasis is placed on determining the mineralogical composition of the fine-grained matrix comprising the U-1a alluvium, as these minerals are likely to have the greatest influence on radionuclide migration. This report also includes the results of stable isotope analyses ($^{18}\text{O}/^{16}\text{O}$ and $^{13}\text{C}/^{12}\text{C}$ ratios) of secondary calcite mineralization. These data are useful in inferring both the origin of the calcite, and the conditions under which it formed. This study is a part of a larger collaboration between Lawrence Livermore National Laboratory, Desert Research Institute, IT Corporation and Los Alamos National Laboratory aimed at determining the statistical variation in mineralogical, physical and hydraulic parameters of geologic materials from the unsaturated zone.

U-1a Drift Complex

The U-1a horizontal drift complex is a reuseable underground tunnel facility designed to house research experiments in support of U.S. Department of Energy defense programs. It is situated within unsaturated basin fill deposits of late Tertiary and Quaternary age in southwestern Yucca Flat. The U-1a.01 main drift is located at an invert-level (see Appendix A for definition) of approximately 293 to 296 m (962 to 971 ft) below the surface (Allen, 1995). The main access to the complex is via the U-1a vertical shaft, although the U-1a.01 main drift also connects with the U-1g vertical borehole at a location ~335 m (1100 ft) north of the U-1a shaft. For additional details, including maps

of the U-1a drift complex, the reader is referred to reports by Allen (1995; 1996a; 1996b; 1999).

Geology of Yucca Flat

Yucca Flat is an intermontane basin that was formed during late Miocene extensional faulting. The mountains surrounding Yucca Flat consist of Precambrian and Paleozoic sedimentary rocks, Mesozoic intrusive rocks, and Tertiary volcanic rocks. Basin fill deposits of late Tertiary and Quaternary age overlie a highly irregular basement surface formed principally on Tertiary volcanics. The basin fill deposits consist of coalescing colluvial and alluvial fan sequences of moderately consolidated to unconsolidated detrital material transported by ephemeral streams from the surrounding highlands. Particle sizes range from clay to boulder size, but are dominated by sand and gravel. In general, the sedimentary lithology closely reflects the adjacent bedrock in the upland areas (Johnson & Hibbard, 1957; Fernald et al., 1968).

Yucca Flat is transected by a major west-dipping high-angle thrust fault (the Tippinip Fault) that strikes NW-SE through the center of the basin. A series of younger north-south striking normal faults (including the Yucca and Carpetbag Faults) are related to subsidence of the basin (Hinrichs, 1968). The depth to basement is greatest in the south-central part of Yucca Flat, where alluvial sequences attain a thickness in excess of 600 m (2000 ft). The water table in central Yucca Flat ranges from approximately 450 m below the surface in the south to >550 m depth in the north (Winograd & Thordarson, 1975). In the vicinity of the U-1a complex, the water table is estimated to be 478 m (1568 ft) below the surface (Allen, 1996b).

Geology of the U-1a Drift Complex

Detailed descriptions of the geology of the U-1a complex are found in Drellack et al. (1989) and Allen (1995; 1996a; 1996b). Most of the information summarized here was drawn from these reports. The alluvium in the U-1a complex is composed of poorly to moderately consolidated stream, slope wash or debris flow deposits. These deposits are a heterogeneous mixture of detritus derived from Tertiary volcanic rocks and Paleozoic carbonate and clastic sediments. The alluvium was deposited intermittently, forming locally discontinuous, poorly stratified deposits. Many of the beds have a lenticular form that implies deposition in a channel or semi-confined slope wash (Drellack et al., 1989). The alluvium is predominantly composed of moderately to poorly sorted sands and gravels. Drellack et al. (1989) developed a mapping unit nomenclature for the U-1a.01 complex that describes the relative abundance of particle sizes for individual beds. Five mapping units were defined (Table 1), with particle sizes classified according to the Wentworth grade scale (see Table 2; Wentworth, 1922). Detailed descriptions of the lithology and bed characteristics of the U-1a map units are found in Drellack et al. (1989) and Allen (1995). Samples collected during the present study are identified with respect to these mapping units in Appendix A.

Table 1: Map unit nomenclature for the U-1a complex (Drellack et al., 1989)

Map Unit (bed type)	Cobbles %	Pebbles %	Sand %	Silt %	Clay %
Type 1 (sand bed)	0 – 1	6 – 19	64 – 85	4 – 16	1 – 4
Type 2 (sandy pebble bed)	0 – 5	10 – 50	46 – 72	3 – 9	0 – 3
Type 3 (pebbly cobbly sand bed)	5 – 20	10 – 30	42 – 65	2 – 11	1 – 6
Type 4 (cobbly sandy pebble bed)	0 – 10	25 – 54	36 – 62	3 – 5	1 – 2
Type 5 (cobble bed)	25 – 40	10 – 30	40 – 60	8 – 9	2 – 3

Table 2: Wentworth grain size classification scale

Particle Size	Particle Diameter (mm)
Boulder	> 256
Cobble	64 – 256
Pebble	2 – 64
Sand	0.0625 – 2
Silt	0.0039 – 0.0625
Clay	< 0.0039

The largest clasts in the U-1a alluvium predominantly consist of Paleozoic limestone and dolomite, with less frequent quartzite and rare Tertiary tuff fragments. In contrast, the better-sorted, finer-grained beds are composed primarily of tuffaceous lithologies. Small pebbles in these beds are derived from both tuff fragments and Paleozoic lithologies, whereas the sand component tends to be rich in pumice and mineral fragments weathered from the tuffaceous rocks (Drellack et al., 1989). The alluvium as a whole is estimated to contain 25-35% Paleozoic clasts (Allen, 1995). In addition to the alluvial deposits, the erosional remnant of an air-fall tuff bed is exposed in portions of the U-1a drift complex. This bed is typically less than 0.6 m (2 ft) in thickness, and is fairly persistent laterally. Petrographic examination suggests it is equivalent to the Rhyolite of Obsidian Butte (~8 Ma), or less likely the Rhyolite of Shoshone Mountain (~9 Ma) (Allen, 1996a).

Secondary calcite (CaCO_3) is widespread in occurrence within the U-1a alluvium, and is found as finely disseminated cement, as thin rinds on individual clasts, as poorly-developed horizontal or vertical caliche stringers, and as rare isolated pockets of euhedral spar crystals <10 cm in diameter (Allen, 1995, 1996b). Calcite cement is generally poorly developed, and probably contributes little to the consolidation of the sediments.

Calculated porosity values for the alluvium section penetrated by the U-1g borehole is approximately 36%. Calculated values from the drift level interval (293-296 m) of U-1g average about 35%. These values are consistent with calculated porosity values from other drill holes in southern Yucca Flat (Allen, 1995). Measured permeability values from the alluvium in the U-1a shaft range from 0.18 to 19 darcys (1.8×10^{-9} to 1.9×10^{-7} cm^2), and generally decrease with depth (Allen, 1995). Permeability values determined at 26 locations in the U-1a.01 LEDOUX drifts (now inaccessible) ranged from 0.02 to 3.0 darcys (2.0×10^{-10} to 3.0×10^{-8} cm^2) (Lowry et al., 1989).

Numerous minor faults have been observed within the U-1a complex. These faults typically trend to the north-northeast and dip at high angles ($>75^\circ$) to the east-southeast. Where measurable, the displacements along the faults are usually small (<1 m). Fault traces are thin (typically <5 mm) and are filled with fine-grained gouge (Allen, 1996b). Clear evidence for fault related secondary mineralization has not been observed, although a sample of fault gouge collected from the U-1a.02 drift (2+60 ft) in 1995 was found to contain disseminated calcite.

Sampling and Analytical Methods

Alluvium samples were collected from the U-1a.102C and 102D drifts on 10 November 1998. Recent mining activities provided spectacular exposures on tunnel walls from which to collect samples. In the 102C drift, a total of 10 samples were collected from the working face at 0+77 ft west of the U-1a.102 drift centerline. The geology of this face was mapped by Brian Allen (Bechtel Nevada) and is shown in Figure 1. Samples were collected along two different transects: a horizontal transect (samples H1–H5) that followed one type of lithology across the face, and a vertical transect (samples V1–V5) that sampled down through the stratigraphic sequence. The sample locations are plotted on Figure 1. Two additional samples were collected along the right rib of the 102D drift at 0+21 ft east of the U-1a.102 drift centerline. These included a sample of the air-fall tuff bed. Allen (1999) notes that the 102C and 102D drifts underwent further excavation after samples were collected for this study. This entailed mining an additional six feet down through the muck/invert level of the drift, increasing the distance between the invert (floor) and the back (ceiling) from 12 ft to 18 ft. Hence, the invert level in Figure 1 of this report is now 6 feet above the current invert level. Comprehensive maps of the geology of the 102C and 102D drifts are found in Allen (1999).

Polished thin sections of the alluvium samples were prepared at the University of California, Davis for the purpose of petrographic and energy dispersive analyses. The alluvium samples were characteristically friable, and it was necessary to impregnate the samples with epoxy prior to thin section preparation. In many cases, it was possible to prepare thin sections that preserved intact sedimentary textures for petrographic study. Petrologic characterization of the U-1a alluvium included: 1) petrographic descriptions of the samples, 2) particle size analysis of two of the samples to determine the weight fraction of component sediments, 3) X-ray diffraction of the different size fractions to evaluate mineralogical variations as a function of particle size, 4) scanning electron microscopy of two bulk samples to document sedimentary textures, and 5) energy dispersive analysis of polished sections using an electron microprobe, to provide semi-quantitative elemental data for mineral identification. In addition, both secondary calcite and carbonate rock samples were analyzed for their stable carbon and oxygen isotope ratios ($^{13}\text{C}/^{12}\text{C}$ and $^{18}\text{O}/^{16}\text{O}$) to provide information regarding the origin and conditions of formation of the secondary calcite.

Lithology of the U-1a.102C and 102D drifts

Descriptions of the lithology and occurrence of individual samples collected during this study are found in Appendix A. This section summarizes the general lithologic characteristics of the alluvium in the U-1a.102C and 102D drifts. The exposure in the 102C drift at 0+77 ft is dominated by type 1 and 2 lithologies; although beds and lenses of type 3 and 4 lithologies were also observed (see Fig. 1 and Table 1). Most of the alluvium consists of moderately to poorly sorted gravelly sands that represent channel fill and overbank flood sediments deposited at medium to high energy. Bedding units dip to the west-southwest at about 3 to 5° (Allen, 1999). Many of the individual beds are laterally continuous across the 20 ft wide exposure of the 102C working face, although bedding thicknesses tend to pinch and swell. Due to the heterogeneous nature of these deposits, coarse- and fine-grained sediments are commonly juxtaposed over vertical intervals of only a few inches. Graded bedding was observed in some of the type 2 lithologic units, but is not common.

Cobble and pebble sized clasts are characteristically 1 to 3 inches in size, but occasionally reach sizes up to ~15 inches (in type 4 lithology). Clasts are typically subangular to subrounded, and consist of both tuffaceous volcanic rocks and Paleozoic carbonate and clastic sedimentary rocks. Clast imbrication was rarely observed, although elongated clasts were sometimes orientated parallel to bedding. Secondary calcite rinds are common, especially on carbonate clasts. Most of the sediments are moderately to poorly indurated and easily friable. The most notable exception is the type 1 bed from which sample V2 was obtained. This unit is relatively well indurated, and is distinguished by the presence of thin (1-2 mm) secondary veinlets of chalcedony and calcite. In general, the alluvial matrix consists of yellowish-brown sand- and silt-sized lithic and crystal fragments and abundant clay minerals derived from the weathering of

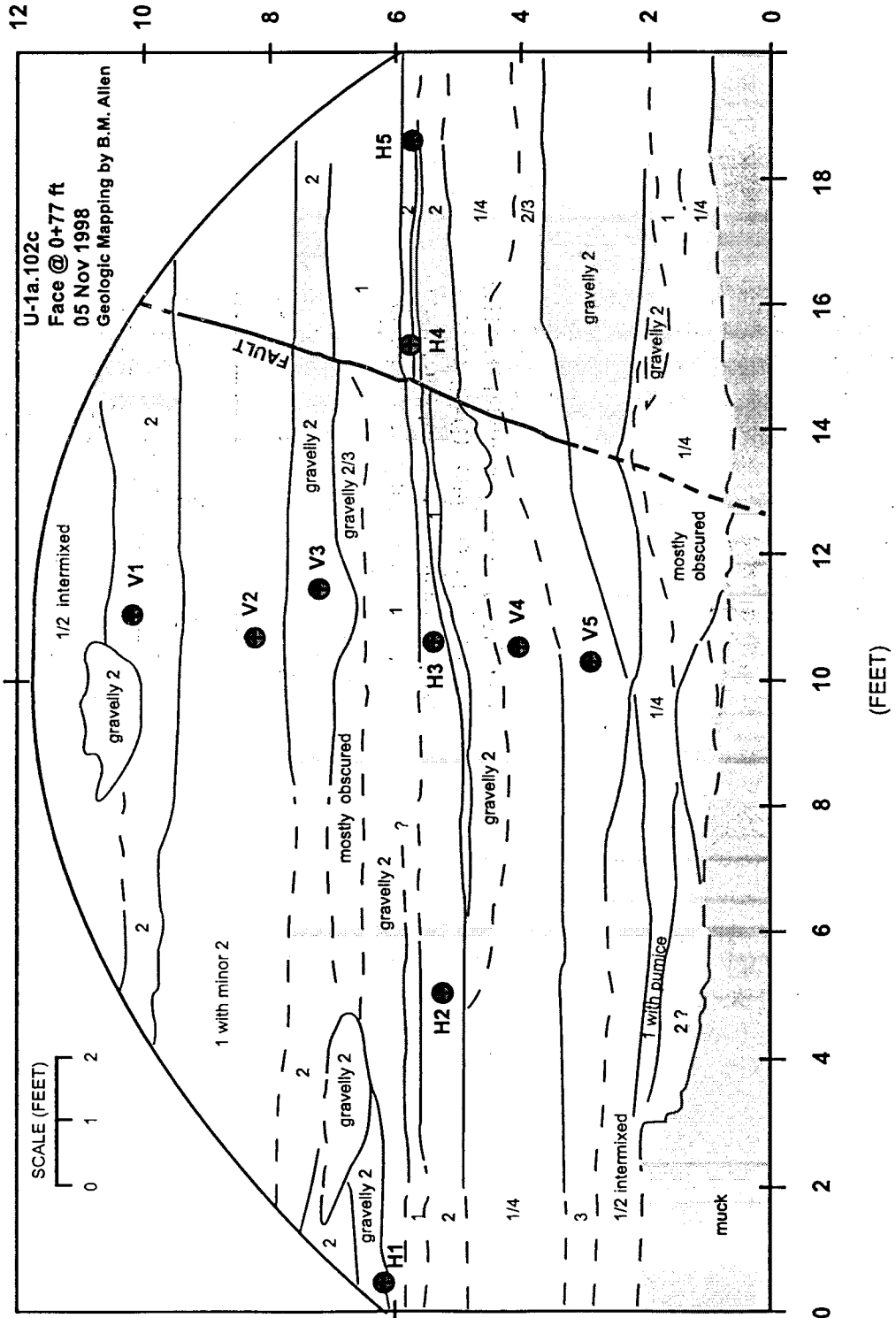


Figure 1: Geology of the U-1a.102c drift face at 0+77 ft, from a preliminary field map drawn by Brian Allen (Bechtel Nevada). Beds are labeled according to lithologic type, using the mapping unit nomenclature developed for the U-1a complex (Drellack et al., 1989). Locations of samples collected along vertical (V1-V5) and horizontal (H1-H5) transects are shown as red dots.

volcanic and sedimentary rocks. The mineralogy of the 102C and 102D drift samples is described in more detail later in this report.

The air-fall tuff unit described by Allen (1996a) was not observed by the authors in the 102C drift, but was exposed in the 102D drift as a compact layer of light greyish-brown vitric tuff, generally lacking in pumice and phenocrysts. The ash bed has been reworked and channelized in most places (Allen, 1999), and was only 1-2 inches in thickness where it was sampled (along the right rib of the 102D drift at 0+21 ft). The sample obtained for this study was well indurated, possibly due to the presence of fine-grained secondary calcite cement. Additional details regarding the geology of the U-1a.102C and 102D drifts are found in Allen (1999).

Particle Size Analysis

Two bulk alluvium samples were sieved to determine the size of their component grains. Sieving required the samples to be disaggregated. Whereas sample V4 was completely unconsolidated, sample V2 had to be gently broken in a mortar and pestle to obtain loose grains. The samples were dry sieved through a sequential series of 8 sizing screens: 2.0 mm, 850 μm , 425 μm , 250 μm , 180 μm , 90 μm , 53 μm , and 45 μm . The particulates captured on each screen were weighed and compared against the total weight of the sample prior to sieving. The results were normalized to 100% and are plotted in Figure 2.

Additional size fraction measurements for samples from the U-1a.102C and 102D drifts are reported in Allen (1999). It is notable that Allen measured the size fractions for samples taken from precisely the same beds where samples V2 and V4 were collected. The sample that is equivalent to V2 was found to contain 23% pebble/cobble, 53% sand, 9% silt and 15% clay. When compared with the data in Figure 2, these results suggest that sample V2 was incompletely disaggregated. The V4 equivalent sample contained 18% pebble/cobble, 60% sand, 10% silt and 12% clay (Allen, 1999). In this case, the results are similar to those obtained for V4 (Fig. 2), although the smallest size fraction in V4 was apparently underestimated.

X-Ray Diffraction Measurements

For sample V4, the eight sieve fractions plus the $<0.45 \mu\text{m}$ size fraction were analyzed by X-ray diffraction to determine whether differences in grain size are correlated with changes in mineralogy. An aliquot of each size fraction was pulverized using a mechanical WC ball mill. The resulting powder was packed into a sample holder and analyzed with an X-ray diffractometer using Cu K α radiation. Individual scans were run from 2° to 62° 2θ , with a 0.02-degree step size and a 2-second count time. A mineral search/match procedure was conducted after computer identification of the major X-ray lines. Due to the reconnaissance nature of the X-ray study, clays were not separated from the bulk sample prior to analysis. The mineral compositions of the nine size fractions are compiled in Table 3.

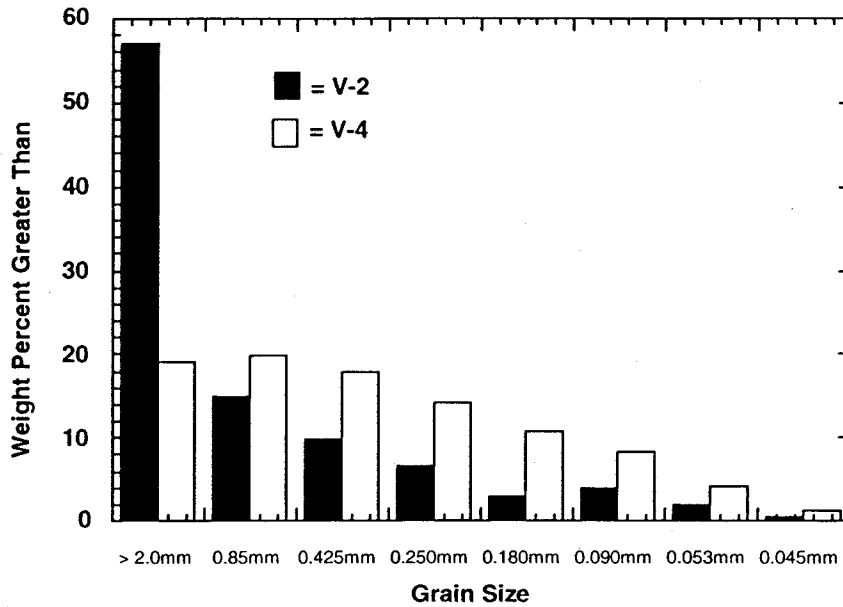


Figure 2: Histogram of weight percent of grain size for samples V2 and V4. Sample V4 exhibits a more uniform grain size distribution than sample V2. The difference in grain size between the two samples may be the result of sample V2 being more cemented and less friable than sample V4. In particular, there is a marked disparity in the relative abundance of the >2 mm size fraction between the two samples.

The results of the X-ray diffraction analyses indicate there is little variation in the mineralogy of the V4 sample due to differences in grain size. The most abundant minerals include quartz, plagioclase feldspar (albite and anorthite), calcite, dolomite, and clay minerals (kaolinite and montmorillonite). This mineral assemblage is not surprising given the heterogeneous nature of the source rocks from which the Yucca Flat alluvium is derived. The quartz and feldspar originates from the weathering of tuffaceous volcanic and clastic sedimentary rocks, whereas the calcite and dolomite reflect the presence of abundant carbonate rock clasts. The principal clay mineral is kaolinite, although the results suggest some of the clays may consist of mixed layer kaolinite-montmorillonite.

Confirmation of mixed layer clays is not possible without separation of the clay fraction and structural studies of the clay interlayers. Iron oxides (hematite) are most prevalent in the coarser size fractions. Their absence in the fine grained material is surprising given that they are frequently observed in thin section as finely disseminated grains (e.g. Fig. 6). Biotite and muscovite micas are identified in the intermediate size fractions. Biotite originates from the weathering of volcanic rocks, whereas muscovite is probably associated with altered feldspar.

Quantitative X-ray diffraction data for the U-1a alluvium were also reported in Drellack et al. (1989) and Allen (1995). In general, the mineral assemblage noted in these reports

Table 3: X-Ray Diffraction analysis of different size fractions (in mm) in sample V4

Mineral	> 2.0	>0.850	> 0.425	> 0.250	> 0.180	> 0.090	> 0.053	>0.045	< 0.045
quartz	X	X	X	X	X	X	X	X	X
albite	X	X	X	X	X	X	X	X	
anorthite	X		X	X	X	X	X	X	X
anorthoclase				X					
calcite	X	X	X	X	X	X	X	X	X
dolomite	X	X		X		X	X	X	X
kaolinite	X	X	X		X	X	X	X	X
hematite	X	X	X						
montmorillonite				X			X	X	
clinocllore				X					
muscovite					X	X			
biotite					X	X			

is the same as that observed during this study. In addition, small amounts of hornblende and clinoptilolite were observed in many samples. Both of these minerals originate from the tuffaceous volcanic rocks. Hornblende is a primary rock-forming mineral; whereas clinoptilolite (a zeolite mineral) is a common glass alteration phase in hydrothermally altered tuffs.

Scanning Electron Microscopy

Two of the whole-rock (bulk) alluvium samples were analyzed by scanning electron microscopy (SEM) to determine mineralogical textures and measure particles sizes. Figure 3 is a representative SEM image of U-1a.102C sample V4 (magnification 2200 x). The scale bar is 10 μm . The sample matrix is a composite of individual grains and grain aggregates $\sim 10 \mu\text{m}$ or less in maximum dimension. Within some of these grains, individual platy minerals are visible with a poorly defined trigonal or hexagonal outline. This morphology is characteristic of clay minerals, and X-ray diffraction and energy dispersive analyses suggest kaolinite is the dominant phase. The euhedral crystal form of these clays is consistent with an authigenic origin (i.e. it formed in place following sediment deposition). In less abundance are rounded and fractured mineral grains that appear to have been mechanically weathered. These probably consist of quartz or feldspar. The elongated fragment on the left side of the SEM image (Fig. 3) is probably a volcanic glass shard.

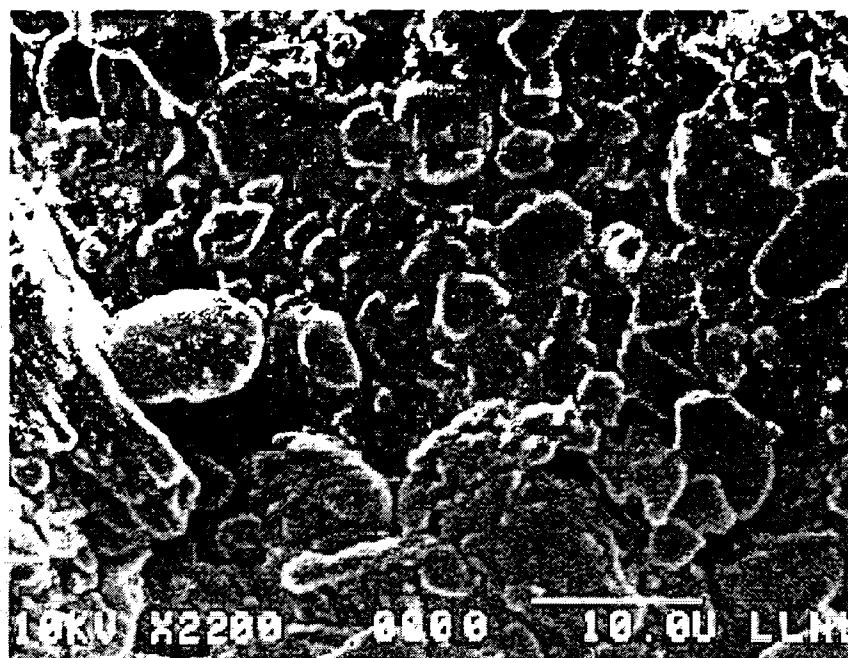


Figure 3: Scanning Electron Microscopy Image of U-1a.102C sample V4. (2200x)
Scale bar is 10 μm .

Petrography of the U-1a.102C and 102D samples

Detailed petrographic descriptions of the thin sections prepared from U-1a alluvium samples are found in Appendix A. This section provides a general synopsis of those observations. A number of thin sections were cut from material that contained small clasts of volcanic, marine carbonate, and clastic sedimentary lithologies associated with the detrital matrix. Quartz, feldspar, calcite, dolomite and clays are the primary minerals comprising the clasts. Some of the tuffaceous clasts contain volcanic glass that is variably altered to secondary minerals (principally chalcedony or zeolite minerals). Marine invertebrate fossils are observed in some of the carbonate clasts. In many cases, the clasts are rimmed by secondary calcite and reddish brown to dark brown clay. Iron oxide phases (hematite and goethite) occur along fractures up to 1 mm in width within some clasts, and quartz or calcite frequently occurs as vein filling material. The clasts typically have little internal porosity.

The detritus surrounding the clasts has three main components: 1) crystal fragments derived from the weathering of volcanic rocks, 2) lithic fragments, usually sand-sized grains of the same material that forms the larger clasts, and 3) a clay-rich matrix. Detrital crystal fragments are dominated by plagioclase, quartz, and K-feldspar, but may include biotite, hornblende, Fe-oxides, pyroxene and calcite. In most cases, the crystal fragments are angular or subangular, implying relatively little transport prior to deposition. The

grain size is generally between 0.1 and 1.0 mm. In some cases, the crystal fragments are relatively fresh and unaltered; more commonly, incipient alteration to secondary minerals is observed, especially along cleavage planes in feldspars.

The most abundant sand-sized (< 2 mm) lithic fragments are composed of clastic sedimentary material, usually fine-grained quartz, feldspar and brown clay minerals. These grains are commonly subrounded. Volcanic glass fragments are also common in many of the samples. Millimeter-sized carbonate rock fragments are less abundant.

The fine-grained matrix contains abundant dark brown clay minerals intermixed with extremely fine-grained secondary calcite. The clay and calcite commonly form concentric layers around larger clasts; in other places the clays exhibit a distinct banded microstratigraphy, forming mat-like textures. Clay minerals typically line voids and pore spaces, sometimes forming relatively large individual crystals (up to 0.1 mm in maximum dimension). The texture of these void-filling clays suggests they are authigenic. Clays are also observed partially replacing volcanic glass and carbonate-rich detrital grains. Iron oxides and oxyhydroxides appear discontinuously throughout the matrix as small euhedral grains; as secondary replacements on grain boundaries, or as minute vein filling deposits. In some samples, secondary quartz, chalcedony, and calcite occur as stringers that crosscut the alluvial matrix. Pore spaces and voids are usually present along the boundaries of detrital grains. The voids tend to be irregular in form and are typically 1 mm or less in maximum dimension.

Energy Dispersive Analysis / Electron Imaging

An electron microprobe equipped a Si(Li) detector and energy dispersive analyzer was used to generate semiquantitative elemental data for identifying minerals observed in thin section. The microprobe was operated at a 15keV accelerating voltage and 10 nA beam current; energy dispersive spectra (EDS) were collected between 1 and 10 KeV. The EDS data was particularly valuable in determining the compositions of minute clay phases that are difficult to identify by optical techniques. Many of the clay minerals were found to contain only Al and Si, indicating that kaolinite is the dominant phase. Where the dark brown clay is matted or clumped, Fe is usually detected with the kaolinite. This may indicate small amounts of admixed iron oxide (hematite) or oxyhydroxide (goethite).

Smectite (montmorillonite) was identified by its characteristic microcrystalline habit under the SEM and the presence of Ca, Mg, Fe, K, Al, and Si in the energy dispersive spectra. Smectite occurs with kaolinite, but in lesser abundance. As noted above, the kaolinite and smectite may sometimes occur as an interlayered phase. Smectite was observed as rinds on detrital feldspars and volcanic glass, where it typically occurs in 5 to 10 μm thick layers. A photomicrograph of smectite replacing a volcanic glass shard is shown in Figure 4. In addition, smectite occurs with kaolinite intermittently as a matrix pore lining. Figure 5 is a photomicrograph of smectite/kaolinite layers lining an exposed

pore. The inner surface of the pore is lined with a discontinuous rind of silica, which appears as small concave platelets.

EDS measurements were also used to determine the compositions of opaque oxide phases. In general the oxide phases are disseminated throughout the sample matrix, but may also occur in clumps or clusters when associated with vein fillings, intergranular spaces, or grain boundaries (Fig. 6). A majority of the oxide phases are Fe-rich. X-ray diffraction results indicate that hematite [Fe_2O_3] is the dominant iron oxide mineral, although goethite [$\text{FeO}(\text{OH})$] is also likely to be present. Mn-Ti-Fe and Mn-Fe oxides were infrequently encountered.

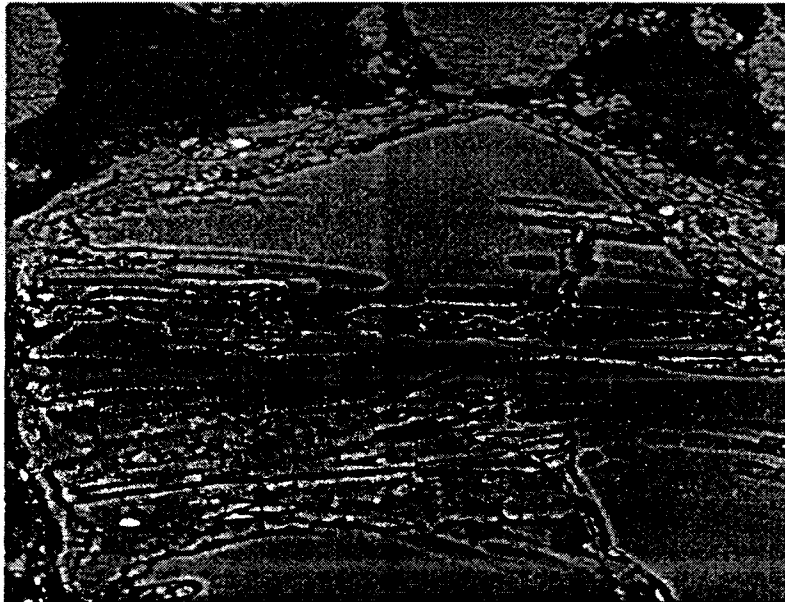


Figure 4: Smectite replacing a volcanic glass shard. Magnification 360x.

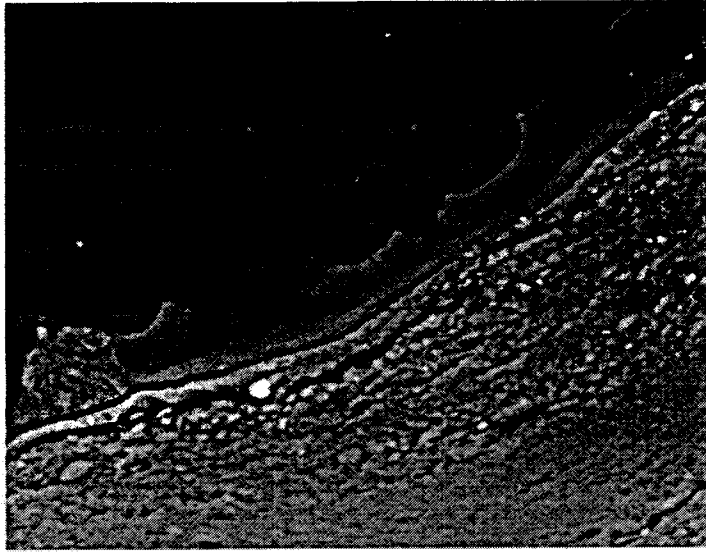


Figure 5: Exposed pore surface in sample D-1 showing smectite and kaolinite clay layers, and a thin silica rind (concave platelets) on the inner wall of the void. Magnification 1,200x.

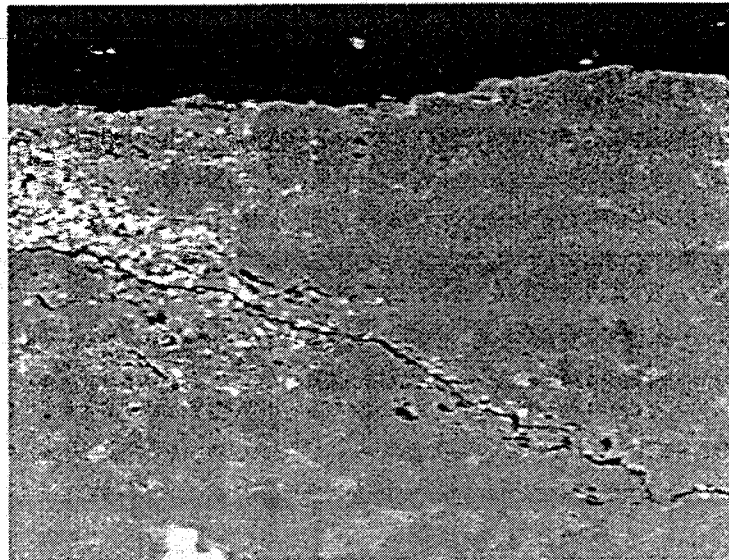


Figure 6: Fracture in alluvium showing the deposition of minute clusters of iron oxides (small bright spots). Magnification 160x.

Stable Isotope Results for Secondary Calcite and Carbonate Rock Samples

Samples of fine-grained alluvial matrix were prepared for stable isotope analysis by sieving disaggregated sample material to -150 mesh. To avoid the introduction of calcite from Paleozoic carbonate clasts, the samples were not crushed. In most cases, the alluvium was poorly indurated and easily friable. Carbonate clasts were also selected from alluvium samples and prepared for isotopic analysis by breaking the clast, picking out pure rock fragments from its interior, and crushing this material so that it passed through a -200 mesh sieve. In addition, spar or caliche rinds on these clasts were separated and prepared for isotopic analysis. Carbonate-bearing samples were reacted with 100% phosphoric acid at 25°C (McCrea, 1950) and the resulting CO₂ gas was extracted and purified on a vacuum line. Carbon and oxygen stable isotope ratios were then measured on a VG Prism isotope ratio mass spectrometer. Results are reported in the conventional δ notation relative to the PDB (carbon) and SMOW (oxygen) standards. Analytical reproducibility is ± 0.1 per mil for carbon and ± 0.2 per mil for oxygen.

The stable isotope results ($\delta^{13}\text{C}$ and $\delta^{18}\text{O}$ values) are reported in Table 4. The table includes data for samples from the 102C and 102D drifts, along with data for samples collected at other locations in the U-1a complex. For comparative purposes, isotope data for Paleozoic carbonate bedrock samples collected from NTS boreholes and wells are also included. The $\delta^{13}\text{C}$ and $\delta^{18}\text{O}$ results for all of these samples are plotted in Figure 7. Secondary calcite samples from the U-1a complex (filled circles in Fig. 7) exhibit a slight positive correlation between $\delta^{13}\text{C}$ and $\delta^{18}\text{O}$, with $\delta^{13}\text{C}$ values ranging from -5.6 to +2.3‰ (PDB) and $\delta^{18}\text{O}$ values ranging from +17.2 and +27.4‰. Relative to the U-1a samples, carbonate rocks from NTS boreholes (open squares) typically have more positive $\delta^{13}\text{C}$ values, and show a broader range in $\delta^{18}\text{O}$ values. Isotopic analyses of four carbonate rock clasts collected from the U-1a alluvium (open diamonds) generally overlap with the carbonate bedrock data, although one clast has a $\delta^{13}\text{C}$ value that more closely resembles the U-1a secondary calcites.

Figure 7 also shows the calculated isotopic value for calcite in equilibrium with an average present-day Yucca Flat groundwater at 30°C[†] (see also Smith et al., 1998). Note that the calculated calcite $\delta^{13}\text{C}$ value (-5.6‰) matches that of the lowest $\delta^{13}\text{C}$ values in the natural calcite samples. Variations in the $\delta^{13}\text{C}$ values of the U-1a secondary calcites are generally consistent with a two-component mixing process involving bicarbonate from groundwater and carbonate derived from the partial dissolution of rock clasts. All of the secondary calcites from the U-1a complex have compositions that lie between these “end-members”. However, the rock clast “end-member” is somewhat loosely defined because of the relatively broad range in $\delta^{13}\text{C}$ values of the parent material.

[†] The average groundwater isotopic composition was determined on the basis of 17 analyses from wells in Yucca Flat (Rose et al., 1997). The hypothetical calcite isotopic value takes into account both the calcite-water ¹⁸O fractionation (O’Neil et al., 1969) and the calcite-bicarbonate ¹³C fractionation (Rubinson and Clayton, 1969; Mook, 1986).

Table 4: Stable isotope results for secondary calcite and carbonate rock samples

Sample Location	Description	$\delta^{18}\text{O}$ (‰ SMOW)	$\delta^{13}\text{C}$ (‰ PDB)	yield (% CaCO_3)
U-1a.102C (0+77) sample V1	fine-grained matrix	+23.9	-1.1	4.9
U-1a.102C (0+77) sample V1	carbonate clast	+20.2	-4.5	72.1
U-1a.102C (0+77) sample V1	calcite spar – rind on clast	+19.5	-3.6	63.1
U-1a.102C (0+77) sample V2	fine-grained matrix	+25.4	-3.2	7.0
U-1a.102C (0+77) sample V3	fine-grained matrix	+23.8	-1.3	3.0
U-1a.102C (0+77) sample V4	fine-grained matrix	+25.3	+0.4	5.5
U-1a.102C (0+77) sample V5	fine-grained matrix	+24.2	-2.5	7.0
U-1a.102C (0+77) sample V5	carbonate clast (dolomite)	+25.7	-0.7	20.1
U-1a.102C (0+77) sample V5	caliche – rind on clast	+22.8	-3.0	61.8
U-1a.102C (0+77) sample H1	fine-grained matrix	+25.4	-1.2	4.6
U-1a.102C (0+77) sample H2	fine-grained matrix	+21.7	-2.9	8.0
U-1a.102C (0+77) sample H3	fine-grained matrix	+24.7	-1.0	2.2
U-1a.102C (0+77) sample H4	bulk sample (milled)	+27.4	+2.3	13.4
U-1a.102C (0+77) sample H4	carbonate clast	+24.1	+3.1	80.1
U-1a.102C (0+77) sample H4	caliche – rind on clast	+23.5	-3.4	48.1
U-1a.102C (0+77) sample H5	fine-grained matrix	+24.7	-1.3	3.7
U-1a.102D (0+21) sample D1	fine-grained matrix	+25.4	-2.6	4.0
U-1a.102D (0+21) sample D2	air fall tuff	+17.6	-5.3	4.0
<i>Samples collected from the U-1a complex in 1995</i>				
U-1a.01 main drift (4+60)	calcite spar – rind on clast	+19.1	-3.4	31.9
U-1a.01 main drift (6+00)	caliche stringer in matrix	+22.8	-4.6	14.9
U-1a.01 main drift (7+50)	air fall tuff	+17.2	-5.6	19.4
U-1a.02 (2+50)	caliche stringer in matrix	+24.2	-3.6	24.4
U-1a.02 (2+60)	fault gouge	+18.1	-5.1	8.9
U-1a.03 x-cut D (0+39)	calcite spar in vug	+17.8	-5.5	97.8
U-1a.03 x-cut D (0+39)	matrix (adjacent to vug)	+21.8	-4.4	14.7
U-1a.03 x-cut B (0+32)	carbonate clast (dolomite)	+25.3	+1.4	46.7
U-1a.03 x-cut B (0+32)	calcite spar – rind on clast	+19.9	-4.2	64.5
<i>Carbonate rock samples from NTS boreholes/wells</i>				
Army Well #1 (1134' below surface)	limestone whole rock	+18.7	+4.3	84.7
Army Well #1 (1134' below surface)	calcite fracture lining	+16.9	+2.6	100.0
UE-1a (515' below surface)	limestone whole rock	+19.7	-1.8	50.1
WW-C (1550-1555' below surface)	limestone whole rock	+14.6	-0.7	89.1
WW-C1 (1580-1590' below surface)	limestone whole rock	+16.5	-0.4	80.7
ER-3-1 (2580' below surface)	calcite vein	+18.4	-0.7	99.2
ER-3-1 (2600' below surface)	calcite vein	+20.6	-0.6	98.2
ER-6-1 (2640' below surface)	dolomite whole rock	+27.0	+0.7	62.9
ER-6-1 (2808' below surface)	dolomite whole rock	+28.1	+0.8	70.7
UE-10j (2110' below surface)	dolomite whole rock	+25.1	+0.3	75.3
UE-10j (2280' below surface)	dolomite whole rock	+27.1	+0.4	58.8
UE-15d (5998' below surface)	dolomite whole rock	+22.0	-1.2	54.6
UE-15i (263' below surface)	limestone whole rock	+13.5	0.0	76.5
UE-16d (996' below surface)	limestone whole rock	+26.8	+5.6	88.9

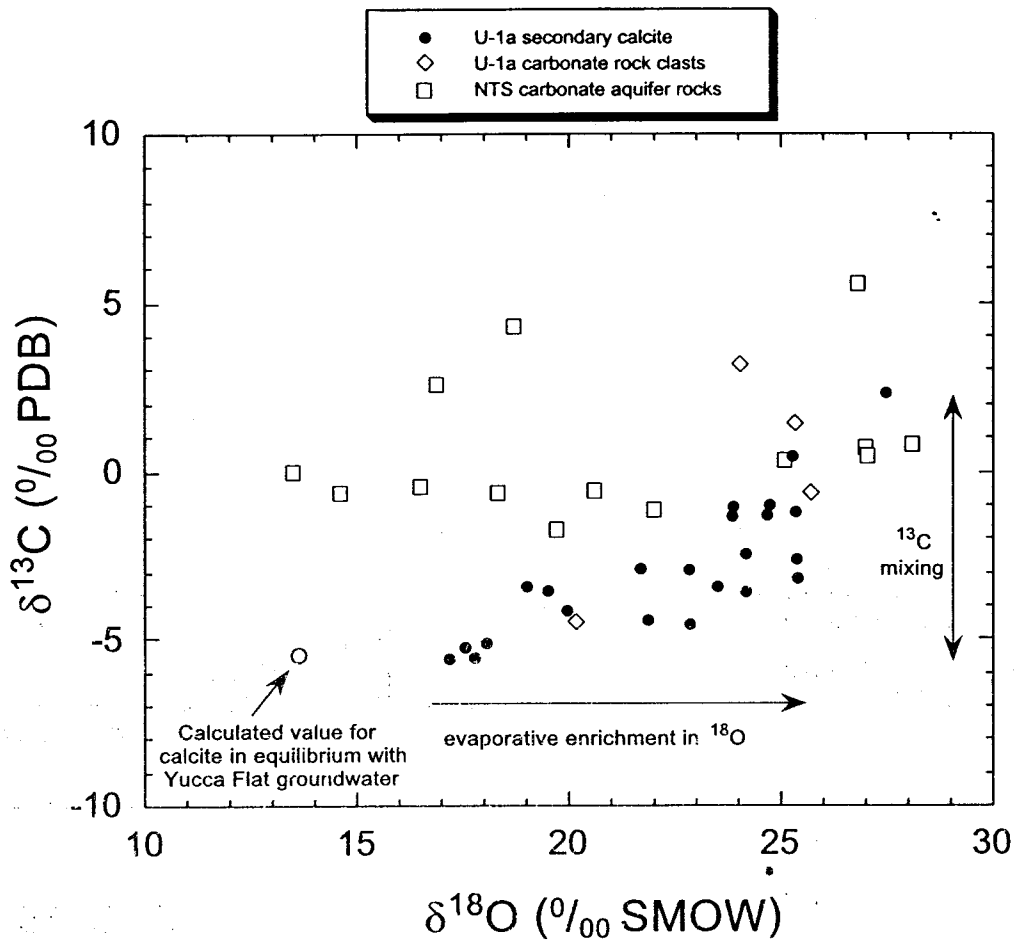


Figure 7: Plot of $\delta^{18}\text{O}$ vs. $\delta^{13}\text{C}$ values for secondary calcite and carbonate rock clasts from U-1a, and carbonate aquifer rocks from NTS boreholes. See text for discussion.

The oxygen isotope values of the U-1a secondary calcites are all enriched in $\delta^{18}\text{O}$ compared to the calculated value for calcite in equilibrium with Yucca Flat groundwater. This variation probably reflects the relative amount of open-system evaporation of the water from which the calcite formed. During evaporation, the light stable isotope (^{16}O) is preferentially lost to the vapor phase, causing a progressive enrichment in the ^{18}O content of the remaining water (see Craig et al., 1963). Evaporation will also cause an increase in the concentration of dissolved solids, driving the residual solution toward calcite saturation. In general, the fine-grained calcite from the U-1a alluvial matrix shows the greatest enrichments in $\delta^{18}\text{O}$, implying high degrees of open system evaporation.

The slight enrichment in $\delta^{13}\text{C}$ with increasing $\delta^{18}\text{O}$ (Fig. 7) implies the fraction of carbon originating from Paleozoic carbonate clasts goes up with increasing evaporation. However, it is interesting to note that the $\delta^{13}\text{C}$ values of the calcareous rinds on carbonate

clasts generally do *not* match the $\delta^{13}\text{C}$ values of the clast itself. In most cases, the $\delta^{13}\text{C}$ data suggest a significant component of groundwater-derived carbon. Lastly, it is notable that relatively depleted (low) calcite $\delta^{18}\text{O}$ values were observed in the air fall tuff layer, and in an isolated vug of calcite spar, implying that some of the calcite probably formed under semi-closed conditions.

Discussion and Conclusions

The results of this study provide insight into potential mineralogical controls on radionuclide transport in the unsaturated zone. The secondary minerals comprising the fine-grained matrix are likely to have the strongest influence on radionuclide sorption. X-ray diffraction and energy dispersive spectra measurements indicate kaolinite is the primary clay mineral in the U-1a.102C alluvium, although smectite (montmorillonite) is also present at lower abundances. Kaolinite is a simple dioctahedral clay with the ideal formula $\text{Al}_2\text{Si}_2\text{O}_5(\text{OH})_4$. Trace amounts of Fe, Ti, Mg and Ca are also usually present. However, due to its lack of interlayer cations, kaolinite has a low cation exchange capacity compared with other clays (approx. 10 mequiv. per 100 g; Weaver and Pollard, 1975). This suggests that kaolinite is unlikely to have a significant influence on radionuclide migration due to ion exchange effects, although adsorption may occur through surface complexation reactions or surface charge effects (e.g. Stumm & Morgan, 1981; Silva & Nitsche, 1995).

Montmorillonite is a dioctahedral smectite commonly found in altered volcanic material. Its ideal formula is $(\text{Na,Ca})_{0.33}(\text{Al,Mg})_2\text{Si}_4\text{O}_{10}(\text{OH})_2\text{nH}_2\text{O}$, with the Na and Ca occupying interlayer sites. The cation exchange capacity of montmorillonite is significantly greater than that of kaolinite, ranging from 70 to 130 mequiv. per 100 g (Weaver & Pollard, 1975). This high exchange capacity is principally due to interlayer ion exchange, and various studies have shown that smectites have a relatively high sorption affinity for cationic radionuclides, including Cs, Sr, Eu, and U (e.g. Erten et al., 1988; Ohnuki & Kozai, 1994; Adeleye et al., 1994; Akcay, 1998). It should be noted that X-ray diffraction results reported in Drellack et al. (1989) and Allen (1995) indicate that montmorillonite is more abundant than kaolinite in the U-1a alluvium. These results are not consistent with our observations, and may suggest the clay minerals are somewhat heterogeneous in their distribution within the U-1a alluvium. Although present in low abundance, both the iron oxides (hematite and goethite) and zeolite minerals (found in altered volcanic clasts) are known to have high cation sorption capacities, and therefore may also have an influence on the bulk retention of radionuclides (e.g. Ames et al., 1983; Park et al., 1992; Ticknor, 1994; Olguín et al., 1994; Collins et al., 1998; Rajec et al., 1998).

It should be noted that whereas particle size analysis generally indicates low abundances of clay *size* fractions, the results of this study indicate that clays are among the most abundant minerals comprising the U-1a alluvium. Petrographic and SEM observations suggest clay minerals tend to occur in banded or matted textures, sometimes in

association with calcite or Fe-oxides. For this reason, the clay-rich matrix is not readily broken down to the size of individual clay grains. Where the matted clay textures are dense and well-developed (e.g. U-1a.102D sample D1) they are likely to locally decrease the permeability of the alluvium. However, the lenticular character of the U-1a bedding units, and the frequent juxtaposition of fine- and coarse-grained sediments over short vertical intervals suggest the long range permeability of the alluvium will not be significantly affected by the clay-rich horizons.

Secondary calcite, though widespread throughout the U-1a alluvium, is probably not present in sufficient amounts to greatly influence the porosity and permeability of the sediments. The $\delta^{13}\text{C}$ results suggest most of the secondary calcite did not originate from the simple dissolution of carbonate rock clasts, but must include an additional source of carbon. Variations in the $\delta^{13}\text{C}$ and $\delta^{18}\text{O}$ values of the secondary calcites suggest mixing with bicarbonate from Yucca Flat groundwater. This implies the secondary calcite may have formed following high stands of the water table in Yucca Flat, perhaps during the interglacial pluvial periods of the late Pleistocene (Winograd & Thordarson, 1975; Smith et al., 1998). Although an alternative model can be envisioned wherein the carbon is derived from downward percolating recharge, one would expect a broader range in more negative $\delta^{13}\text{C}$ values under those circumstances.

It is important to keep in perspective the fact that this study investigates compositional variations over a very narrow interval of the entire Yucca Flat alluvial sequence. Models for radionuclide migration in the unsaturated environment will need to account for vertical variations in mineralogy throughout the entire stratigraphic sequence. Some data is available to suggest that the porosity and permeability of Yucca Flat alluvium decreases with increasing depth (Drellack et al., 1989). However, further studies of the variation in mineralogy as a function of depth are desirable, and would provide insight into whether the relative proportions of key mineral constituents (e.g. kaolinite vs. smectite) vary throughout the sequence. For example, if the proposed model for secondary calcite formation is correct, an increase in the abundance of calcite cement may be observed in close proximity to the water table. Of equal importance is the thorough characterization of the volcanic tuff units that underlie the alluvium, as these are generally interpreted to represent a hydrologic barrier to the downward transmission of surface recharge (Winograd & Thordarson, 1975).

Acknowledgments

We thank Brian Allen for valuable assistance in the acquisition of samples from the U-1a drift complex, and for providing a detailed geologic map of the 102C drift exposure. We also thank Gail Eaton for preparing some of the figures for this manuscript. This work was funded by the Underground Test Area (UGTA) project, U.S. Department of Energy, Nevada Operations Office. The work was performed under the auspices of the U.S. Department of Energy by Lawrence Livermore National Laboratory under contract number W-7405-Eng-48.

References

- Adeleye, S.A., Clay, P.G., and Oladipo, M.O.A. (1994) Sorption of caesium, strontium and europium ions on clay minerals. *Journal of Materials Research*, v. 29, p. 954-958.
- Akçay, H. (1998) Aqueous speciation and pH effect on the sorption behavior of uranium by montmorillonite. *Journal of Radioanalytical and Nuclear Chemistry*, v. 237, p.133-137.
- Allen, B.M. (1995) Preliminary geologic site characterization of the LYNER horizontal drift complex, Yucca Flat, Nevada Test Site. Raytheon Services Nevada, Geologic Report, TSP:DGP:080:95, 71 p.
- Allen, B.M. (1996a) Geologic site characterization of the LYNER U1a.03 drift, Yucca Flat, Nevada Test Site. Bechtel Nevada, Geologic Report, 13 p.
- Allen, B.M. (1996b) Preliminary geologic site characterization of the LYNER U1a.100 and U1a.101 drifts, Yucca Flat, Nevada Test Site. Bechtel Nevada, Geologic Report, 33 p.
- Allen, B.M. (1999) Geology in the U1a.102C and U1a.102D drifts, U1a complex. Bechtel Nevada Memorandum 2150-HB-99-0040, 11 p.
- Ames, L.L., McGarrah, J.E., and Walker, B.A. (1983) Sorption of trace constituents from aqueous solutions onto secondary minerals; I, Uranium. *Clays and Clay Minerals*, v. 31, n. 5, p. 321-334.
- Benedict, F.C., Jr., DeCarlo, E.H., and Roth, M. (1997) Kinetics and thermodynamics of dissolved rare earth uptake by alluvial materials from the Nevada Test Site, southern Nevada, U.S.A. In: Xie Xuejin (ed.), *Proceedings of the 30th International Geological Congress, Beijing, China, 4-14 August 1996*, v. 19, p. 173-188.
- Collins, C.R., Sherman, D.M., and Ragnarsdóttir, K.V. (1998) The adsorption mechanism of Sr^{2+} on the surface of goethite. *Radiochimica Acta*, v. 81, p. 201-206.
- Craig, H., Gordon, L.I., and Horibe, Y. (1963) Isotope exchange effects in the evaporation of water: 1. Low-temperature experimental results. *Journal of Geophysical Research*, v. 68, p. 5079-5087.
- Drellack, S.L., Jr., Thompson, P.H., and Rayburn, C.J. (1989) Geology of the U-1a.01 horizontal drift complex, southwestern Yucca Flat, Nevada Test Site. Fenix & Scisson, Inc., Geologic Report, DOE/NV/10322-37, 69 p.
- Erten, H.N., Aksoyoglu, S., Hatipoglu, S., Göktürk, H. (1988) Sorption of cesium and strontium on montmorillonite and kaolinite. *Radiochimica Acta*, v. 44/45, p. 147-151.
- Fernald, A.T., Corchary, G.S., Williams, W.P., and Colton, R.B. (1968) Surficial deposits of Yucca Flat area, Nevada Test Site. In: E.B. Eckel (ed.), *Nevada Test Site*, Geological Society of America, Memoir 110, p. 49-55.
- French, R.H. (1986) Daily, seasonal, and annual precipitation at the Nevada Test Site, Nevada. Desert Research Institute, Water Resources Center, Publication # 45042, 57 p.
- Hinrichs, E.N. (1968) Geologic structure of Yucca Flat area, Nevada. In: E.B. Eckel (ed.), *Nevada Test Site*, Geological Society of America, Memoir 110, p. 239-246.
- Johnson, M.S., and Hibbard, D.E. (1957) Geology of the Atomic Energy Commission Nevada Proving Grounds Area, Nevada. U.S. Geological Survey Bulletin 1021-K, 55 p.

- Kao, C.S., Smith, D.K., and McKinnis, W.B. (1994) New observations of infiltration through fractured alluvium in Yucca Flat, Nevada Test Site: A preliminary field investigation. Lawrence Livermore National Laboratory Report UCRL-ID-116129, 41 p.
- Laczniak, R.J., Cole, J.C., Sawyer, D.A., and Trudeau, D.A. (1996) Summary of hydrogeologic controls on ground-water flow at the Nevada Test Site, Nye County, Nevada. U.S. Geological Survey Water-Resources Investigations Report 96-4109, 59 p.
- Lowry, B., Dalvit Dunn, S., and Keller, C. (1989) In-situ permeability measurements, and the gas flow diagnostic design for the LEDOUX event. In: Olsen, C.W. and Carter, J.A. (eds.), Proceedings of the Fifth Symposium on Containment of Underground Nuclear Explosions, Santa Barbara, CA, 19-21 September 1989, Lawrence Livermore National Laboratory Report CONF-08909163, v. 1, p. 384-394.
- McCrea, J.M. (1950) On the isotopic chemistry of carbonates and a paleotemperature scale. *Journal of Chemical Physics*, 18: 849-857.
- Mook, W.G. (1986) ^{13}C in atmospheric CO_2 . *Netherlands Journal of Sea Research*, v. 20, p. 211-223.
- Ohnuki, T., and Kozai, N. (1994) Sorption characteristics of radioactive cesium and strontium on smectite. *Radiochimica Acta*, v. 66/67, p. 327-331.
- Oliguín, M.T., Solache, M., Asomoza, M., Acosta, D., Bosch, P., and Bulbulian, S. (1994) UO_2^{2+} sorption in natural mexican erionite and Y zeolite. *Separation Science and Technology*, v. 29, p. 2161-2178.
- O'Neil, J.R., Clayton, R.N., and Mayeda, T.K. (1969) Oxygen isotope fractionation in divalent metal carbonates. *Journal of Chemical Physics*, v. 51, p. 5547-5558.
- Park, C.K., Woo, S.I., Tanaka, T. and Kamiyama, H. (1992) Sorption and desorption behavior of ^{60}Co , ^{85}Sr , and ^{137}Cs in a porous tuff. *Journal of Nuclear Science and Technology*, v. 29, p. 1184-1193.
- Pohl, G.M., Warwick, J.J., and Tyler, S.W. (1996) Coupled surface-subsurface hydrologic model of a nuclear subsidence crater at the Nevada Test Site. *Journal of Hydrology*, v. 186, p. 43-62.
- Rajec, P., Macašek, F., Féder, M., Misadlides, P., and Šamajová, E. (1998) Sorption of caesium and strontium on clinoptilolite- and mordenite-containing sedimentary rocks. *Journal of Radioanalytical and Nuclear Chemistry*, v. 229, p. 49-55.
- Rose, T.P., Kenneally, J.M., Smith, D.K., Davisson, M.L., Hudson, G.B., and Rego, J.H. (1997) Chemical and isotopic data for groundwater in southern Nevada. Lawrence Livermore National Laboratory Report UCRL-ID-128000, 35 p.
- Rubinson, M. and Clayton, R.N. (1969) Carbon-13 fractionation between aragonite and calcite. *Geochimica et Cosmochimica Acta*, v. 33, p. 997-1002.
- Silva, R.J., and Nitsche, H. (1995) Actinide environmental chemistry. *Radiochimica Acta*, v. 70/71, p. 377-396.
- Smith, D.K., Rose, T.P., Davisson, M.L., Hudson, G.B., Niemeyer, S., and Moeller, A.E. (1998) Volatile and fluid transport in deep, arid soils. Lawrence Livermore National Laboratory Report UCRL-ID-129653, 10 p.
- Stumm, W., and Morgan, J.J. (1981) *Aquatic Chemistry*, 2nd ed. John Wiley and Sons, New York, 780 p.

- Ticknor, K.V. (1994) Uranium sorption on geological materials. *Radiochimica Acta*, v. 64, p. 229-236.
- Tyler, S.W., McKay, W.A., and Mihevc, T.M. (1992) Assessment of soil moisture movement in nuclear subsidence craters. *Journal of Hydrology*, v. 139, p. 159-181.
- Weaver, C.E., and Pollard, L.D. (1975) *The Chemistry of Clay Minerals. Developments in Sedimentology*, v.15, Elsevier, Amsterdam, 213 p.
- Wentworth, C.K. (1922) A scale of grade class terms for clastic sediments. *Journal of Geology*, v. 30, p. 377-392.
- Winograd, I.J., and Thordarson, W. (1975) Hydrogeologic and hydrochemical framework, south-central Great Basin, Nevada-California, with special reference to the Nevada Test Site. U.S. Geological Survey Professional Paper 712-C, 126 p.
- Wolfsberg, K. (1978) Sorption-desorption studies of Nevada Test Site alluvium and leaching studies of nuclear test debris. Los Alamos National Laboratory Report LA-7216-MS, 33 p.

Appendix A: Lithologic and Petrographic Sample Descriptions

Samples H1 through H5 were collected along a horizontal transect across the working face of the U-1a.102C drift, at 0+77 ft west of the U-1a.102 drift centerline. Samples V1 through V5 were collected along a vertical transect on the same face (refer to Fig. 1). Samples D1 and D2 were collected on the right rib of the U-1a.102D drift, at 0+21 ft east of the U-1a.102 drift centerline. All samples were collected on 10 November 1998. The numerical values given for the type of lithology (1 thru 5) are consistent with the U-1a mapping unit nomenclature of Drellack et al. (1989) and Allen (1995) given in Table 1.

U-1a.102C drift (0+77 ft) – Sample H1

Position: 0.5 ft to the right of the left rib; 5.6 ft above the invert*

Lithologic Description and Occurrence

Type 2, coarse gravelly sand; yellowish-brown; moderately to poorly indurated. Moderately sorted, with individual clasts up to ~ 2 inches (5 cm). Clasts are subrounded to subangular, and consist of tuffaceous and pre-Tertiary fragments (especially carbonate rocks). Secondary calcite rinds are common on carbonate clasts. Sample was taken from a small channel-fill deposit that truncates other bedding units at this location.

Petrographic Description

Thin section was prepared from a 1.5 in. (3.8 cm) quartzite clast with a thin, well-cemented rind of fine-grained detritus.

Clast: Equigranular quartz grains (avg. ~0.1 mm) comprise >90% of clast, showing polygonal grain boundaries characteristic of an earlier episode of metamorphism. Light brownish-gray intergranular clay and carbonate minerals form well-developed coatings between individual quartz grains. Clast contains a series of sub-parallel fractures along which Fe-oxide (and possible Mn-oxide) phases were deposited. In reflected light, the mineralized fractures are up to ~1 mm in width, with reddish-brown vein fillings indicative of hematite [Fe₂O₃] and/or goethite [FeO(OH)]. The clast is generally lacking open void spaces, even along the mineralized fractures.

Matrix: The rim of the quartzite clast is *dominated* by calcite on one side and by clays + iron oxides on the other side. Secondary calcite rim forms small (<0.1 mm) euhedral crystals in places, implying growth into open space.

* *Invert* is a mining term for the floor of a drift. The reported distance above the invert is the value that was measured on 10 Nov 98.

Since that time, the invert level was mined down an additional 6 feet.

U-1a.102C drift (0+77 ft) – Sample H2

Position: 5.0 ft to the right of the left rib; 5.2 ft above the invert

Lithologic Description and Occurrence

Type 2, gravelly sand; yellowish-brown; moderately indurated. Moderately well-sorted, subangular to subrounded clasts, typically < 1 in. (2.5 cm) in maximum dimension; rare clasts up to 2 in. (5 cm). Gravel clasts consist of approximately equal abundances of tuffaceous and pre-

Tertiary fragments (especially carbonate rocks). Sample is from a graded bed, ~ 5 in. (12.7 cm) in thickness. Long axes of pebbles are oriented subparallel to bedding, some showing imbricate structure.

Petrographic Description

Thin section is dominated by a 1 in. (2.5 cm) clast of fine-grained calcareous siltstone set in a fine-grained detrital matrix.

Clast: Consists of fine-grained quartz (0.05 to 0.1 mm) + carbonate minerals + clays, together with irregular clumps of darker iron oxides and opaque minerals; weakly foliated. No significant fracturing or void space occurs within the clast. Carbonate minerals are leached from the outer 1 mm of the siltstone, and evidently reprecipitated on the clast exterior. Euhedral calcite spar (to 0.1 mm) occurs in open spaces along the rim. In some places, there is an intermediate rind of Fe-oxides and clays (+ Mn-oxides?) deposited between the leached clast and the carbonate rind, displaying radiating crystal growth patterns; this sequence is not uniformly developed.

Matrix: The matrix surrounding the siltstone clast consists of subangular sand-size detrital grains (avg. 0.3 to 0.5 mm; 1.0 mm maximum) set in a clay + carbonate mineral matrix. Iron oxides impart a reddish-brown color to the clay-rich matrix. The detrital grain assemblage includes: (1) crystal fragments derived from volcanic rocks (feldspar + quartz + minor biotite and hornblende; very little secondary alteration is observed, even in the ferromagnesian silicate phases); (2) subrounded, brown clay-rich fragments; (3) volcanic glass fragments (commonly vitric); and (4) re-worked composite clastic and carbonate sediment grains. Small (< 1 mm) intergranular voids are relatively abundant. The walls of these voids are coated with thin films of brownish-gray clays or possible carbonate minerals (with high birefringence).

U-1a.102C drift (0+77 ft) – Sample H3

Position: 10.6 ft to the right of the left rib; 5.3 ft above the invert

Lithologic Description and Occurrence

Type 2, gravelly sand; yellowish-brown; moderately to poorly indurated. Moderately sorted, containing subangular to subrounded clasts, typically 1-2 in. (2.5 to 5 cm) in size; a few clasts up to 3 in. (7.6 cm). The sample exhibits more or less a continuum in particle sizes, but the smaller size fractions predominate. The gravel size fraction includes both tuffaceous and pre-Tertiary fragments (especially carbonate rock fragments). The bed from which the sample was taken is ~4 in. (10.2 cm) in thickness, and shows no gradation or sorting of size fractions; gravel clasts exhibit no preferred orientation. Textural evidence suggests the unit was deposited relatively quickly, probably at the distal end of an ephemeral stream (hence the moderately good sorting).

Petrographic Description

Thin section provides a good example of the intact texture of a moderately well sorted sand (larger clasts are not present in the thin section). Detrital grains/fragments comprise ~50% of the sample; the remainder of the sample is dominated by a clay-rich matrix.

Detrital material includes the following: Crystal fragments (~20%), typically 0.5-1.0 mm; 1.5 mm maximum.

The crystal detritus is mineralogically “immature” and includes plagioclase, alkali feldspar, quartz, biotite.

hornblende, single crystal calcite grains, and discrete grains of opaque iron oxides. Crystal fragments tend to

be angular and relatively unaltered.

Lithic fragments (~25-30%), typically ≤ 1 mm; rarely up to 3 mm maximum. Composed of subangular to rounded

grains of quartz/feldspar *or* calcite with individual sub-fragments ≤ 0.2 mm, cemented with fine-grained clays,

calcite, and/or Fe-oxides. Also present are subrounded to rounded, brown detrital grains composed almost

entirely of very fine grained clays. Other detritus includes glassy pumice fragments and calcareous shell

fragments.

Matrix: Detrital grain boundaries are typically rimmed with a thin veneer of very fine grained clay minerals, stained brown with included iron oxides or oxyhydroxides. Secondary calcite rims occur on some carbonate detritus. Intergranular pores and voids are relatively common. Clay minerals (with iron oxides) form the lining in most of the pores, but the distribution of pore space is variable. In some cases, voids are entirely filled with brownish clay material, whereas clay minerals are almost absent in other voids.

U-1a.102C drift (0+77 ft) – Sample H4

Position: 15.3 ft to the right of the left rib; 5.6 ft above the invert

Lithologic Description and Occurrence

Type 2, gravelly sand; dark yellowish-brown; moderately indurated. Moderately sorted, containing subangular to subrounded clasts typically ≤ 1 in. (2.5 cm), but ranging in size up to 3 in. (7.6 cm). Gravel is dominated by carbonate and cherty rock fragments, but also includes tuffaceous material. The layer that was sampled is 3 to 4 in. (7.6 to 10.2 cm) in thickness, and shows no gradation or sorting of size fractions. Silty layers occur both above and below this unit. Moderate energy, fluvial depositional environment.

Petrographic Description

Thin section was cut from a carbonate rock clast that is ~ 1 in (2.5 cm) in maximum dimension, rimmed with secondary calcite + clay minerals.

Clast: Primary marine carbonate rock that has been extensively recrystallized and contains abundant fossil shell fragments, especially molluscs (gastropoda, pelecypoda). The rock from which the clast was derived was cut by secondary calcite + quartz veins up to 2 mm in thickness, with individual crystals ~1 mm in maximum dimension. Quartz (chalcedony?) vein material sometimes forms beautiful radiating aggregates. The vein material contains no pore volume.

Matrix: The rim of the clast shows evidence of precipitation of secondary calcite in thin bands. Tiny, free-growing spar crystals occur in places. Secondary carbonate minerals are admixed with brownish, low-birefringence clay minerals.

U-1a.102C drift (0+77 ft) – Sample H5

Position: 18.6 ft to the right of the left rib; 5.7 ft above the invert

Lithologic Description and Occurrence

Type 2, gravelly sand; yellowish-brown; moderately to poorly indurated. Moderately sorted, containing subangular to subrounded clasts typically ≤ 1 in. (2.5 cm), but ranging in size up to 3 in. (7.6 cm). Clasts consist of both tuffaceous and pre-Tertiary fragments (the latter dominated by carbonate rock fragments). Sample layer is 4 to 5 in. (10.2 to 12.7 cm) in thickness, and is laterally continuous with the bed at location H4.

Petrographic Description

Thin section was cut from two separate pieces, each containing calcareous clasts with extensive rinds and attached sedimentary matrix.

H5 fragment #1.

Clast: Consists of a 1 cm fragment of weathered carbonate rock embedded in a rip-up clast of sedimentary matrix that was recycled into this deposit. The clast matrix consists of a dense, matted dark brown clay containing angular to subangular quartz, plagioclase, opaque oxides, and lithic fragments. In places, the matrix exhibits alternating bands of calcite and dark brown clay (w/ admixed iron oxyhydroxides?).

Matrix: The composite clast is embedded in a sedimentary matrix typical of the U-1a alluvium. The texture and assemblage of detrital material is notably different from that of the composite clast. Detritus includes a high abundance of pumice fragments, with lesser amounts of lithic and crystal fragments. Fragments are ≤ 2 mm in maximum dimension. Brown clay rims are common on many of the fragments, and the cement consists of a fine-grained mixture of clay + carbonate minerals, probably with Fe-oxyhydroxides. The matrix is characterized by a relatively high pore volume (unlike the embedded composite clast, where the pore volume is low). Voids are lined with clays and/or carbonate minerals, and rarely chalcedony.

H5 fragment #2.

Clast: Composite carbonate rock fragment with a complex history prior to deposition in Yucca Flat alluvium. The main part of the clast is fossiliferous limestone containing small shell and crinoid stem fragments set in a dense, fine-grained matrix. This material was subsequently invaded by coarse calcite veins that brecciated the original rock and deposited blocky, interlocking calcite crystals (up to 1 mm) in fractures up to 5 mm in width.

Matrix: The carbonate rock fragment described above is set in a matrix of alluvial detritus that includes subrounded lithic fragments (typically quartz-feldspar siltstone or clay-rich grains), angular fragments of quartz and feldspar, and volcanic glass fragments. Individual lithic fragments are up to ~ 4 mm in length. The matrix cement composition is variable. One side of the large carbonate rock fragment has a thick rind of secondary calcite cement with lesser amounts of admixed clay minerals. This cement completely surrounds smaller detrital fragments adhering to the larger clast, and tiny euhedral calcite crystals have formed in open spaces. The opposite side of the carbonate rock fragment is coated with secondary clay minerals, but not calcite. This tendency for preferential growth of calcite on one side and clays on the opposite side is mimicked on some of the smaller lithic fragments.

Intergranular pore space is relatively abundant (~15% by volume). Pores are lined with either clay minerals or microcrystalline calcite, depending on the location in the sample.

U-1a.102C drift (0+77 ft) – Sample V1

Position: 11.0 ft to the right of the left rib; 10.1 ft above the invert

Lithologic Description and Occurrence

Type 2, cobble-rich, gravelly sand; yellowish-brown; moderately to poorly indurated. Sediment is poorly sorted, and includes cobbles up to 6 x 9 inches (15.2 x 22.9 cm), abundant gravel and sand, and fine-grained silt. Cobble and gravel sized particles are typically subangular, and consist of pre-Tertiary carbonate and clastic rocks, with subordinate volcanic tuff fragments. The bedding pinches and swells in thickness, ranging from 12 to 24 inches (30.5 to 61 cm). Probably represents channel-fill sediment that was deposited under relatively high-energy conditions.

Petrographic Description

Thin section was prepared from six separate fragments of alluvial material.

V1 fragment #1.

Carbonate rock fragment < 1 cm in size consisting of interlocking calcite or dolomite grains up to 0.25 mm. Rim of clast has a thin “weathering” layer (10-20 μm) consisting of very fine grained calcite + clays. Outside this rim, the alluvial matrix consists of fine-grained clay + carbonate minerals containing angular fragments of quartz and feldspar.

V1 fragment #2.

Similar to fragment #1, consisting of a ~1 cm carbonate clast containing ~5% detrital quartz grains. Recrystallized, interlocking carbonate + quartz grains show little variation in size, and are typically 0.1 mm in maximum dimension. Fluid infiltration along fractures resulted in minor carbonate dissolution, and precipitation of fine-grained clays with dark brown to black oxide minerals.

The carbonate clast has an alteration rind consisting of a 0.1 mm layer of well-crystallized kaolinite (EDS analysis) upon which a thick rim of greyish-brown clay and carbonate minerals were deposited. The thick outer rim contains severely corroded feldspar grains that appear to be dissolving at the expense of clay mineral growth. Banded clay alteration rims are clearly visible on the altered feldspar grains.

Outside the alteration rind, the matrix consists of feldspar + quartz fragments and clay-rich lithic fragments (some with a distinctive fibrous texture) set in a matrix containing abundant carbonate cement with fine-grained clay minerals.

V1 fragment #3

Small (< 1 cm) clast consisting of subequant grains of feldspar + quartz, ~ 0.1 mm in size, comprising between 65 and 95% of the rock mode. The remainder of the clast consists of calcite + clay cement, which varies in abundance from <5% to ~35% of the rock mode. Opaque oxide minerals occur as minor secondary replacements on feldspar/quartz grain boundaries, and as small euhedral grains. No associated matrix.

VI fragment #4

Rock fragment (< 1 cm) consisting principally of secondary carbonate minerals, with lesser amounts of clays + Fe oxides that have largely replaced the primary mineral assemblage. Some relict feldspar and quartz grains remain, but in most cases the primary minerals are completely altered to calcite + clay. Void spaces are filled with secondary calcite or chalcedony. Although the rock mode runs as high as 75% carbonate minerals, the textures clearly suggest carbonate mineral replacement of a pre-existing clastic rock.

No associated matrix.

VI fragment #5

Fragment consists of a 5 mm clast of devitrified tuff embedded in alluvial matrix. Within the tuff fragment, 'ghosts' of poorly welded glass shards are visible, now devitrified to cryptocrystalline silica. The matrix surrounding the clast contains angular, relatively unaltered feldspar, quartz and hornblende fragments, together with clastic sedimentary lithic fragments (up to 2 mm). The matrix itself consists of clay with minor amounts of calcite + silica.

VI fragment #6

This piece is similar to VI fragment #4, and consists of a fine-grained clast in which calcite has largely replaced a pre-existing volcanic rock. Rock contains ~5% relict grains of quartz and ~5% brown iron oxides + opaque oxide minerals; the remainder of the rock mode is dominated by fine-grained calcite (crystals rarely exceeding 0.1 mm) and minor clays. Relict prisms of what were originally plagioclase crystals (?) are now completely replaced by calcite. No associated matrix.

U-1a.102C drift (0+77 ft) – Sample V2

Position: 10.6 ft to the right of the left rib; 8.2 ft above the invert

Lithologic Description and Occurrence

Type 1, volcanoclastic sand and silt; yellowish-brown; well indurated compared to most U-1a alluvium. Moderately well sorted, containing rare subrounded to subangular pebbles of volcanoclastic and carbonate rock, 1 to 2 inches in diameter (2.5 - 5 cm). Bedding is cross cut by a number of thin veinlets formed by the precipitation of fine-grained calcite and silica along fractures. Matrix contains rare secondary calcite spar. Bed thickness averages ~22 in. (56 cm).

Petrographic Description

Thin section reveals a moderately well sorted volcanoclastic siltstone. Detrital grains and crystal fragments comprise 35 to 40% of the sample; the remainder consists of clay-rich matrix cut by secondary veins of chalcedony and calcite.

Detrital material includes the following:

Crystal fragments (~25%), ≤ 1.0 mm maximum size, dominated by alkali feldspar, plagioclase and quartz, with

lesser amounts of biotite, hornblende, pyroxene, and 0.1 mm opaque oxides. Crystal fragments tend to be

angular and fairly unaltered in appearance; incipient alteration of feldspars is visible along fractures and grain

boundaries.

Lithic fragments (~10-15%), generally ≤ 0.5 mm in size; includes subrounded siltstone lithic fragments and dark-

brown detrital grains composed of fine grained clays.

Matrix: Consists predominantly of brown clay minerals, some of which occur in thick, layered mats. Clay minerals

commonly form overgrowths on detrital grains. The sample contains several prominent composite veins (up to 1.5

mm thick). The largest of these is a chalcedony vein rimmed with banded clays and/or iron oxides (reddish-brown,

semi-opaque). Carbonate-bearing fluids subsequently formed thin calcite stringers (0.2 to 0.3 mm) that cross cut

the chalcedony vein and filled small voids at the core of the vein. Concentric bands of clay minerals were co-

precipitated along some of these veinlets.

There are a number of small, irregular-shaped voids throughout the matrix (up to 1 mm across).

In general, the voids are lined with the same clay minerals that comprise the sample matrix.

U-1a.102C drift (0+77 ft) – Sample V3

Position: 11.4 ft to the right of the left rib; 7.2 ft above the invert

Lithologic Description and Occurrence

Type 2, gravelly sand; dark yellowish-brown; moderately to poorly indurated. Moderately sorted, containing subangular to subrounded clasts up to 3 in (7.6 cm) comprising 25 to 30% of rock.

Clasts consist of both tuffaceous and pre-Tertiary fragments, and exhibit no preferred orientation.

Sparse calcite spar in matrix, locally abundant on carbonate clasts. Bedding is weakly graded.

Bed thickness averages 6 to 7 inches (15.2 to 17.8 cm). Laminated silt-rich units occur both above and below this unit. Moderate energy fluvial depositional environment.

Petrographic Description

Thin section was cut from a relatively well-sorted graded bed and varies from fine-grained siltstone to coarser silty sandstone. Detrital grains and crystal fragments comprise up to 50% of the sample. Matrix is clay-rich.

Detrital material includes the following:

Crystal fragments (25-30%), typically ~0.5 mm, consisting of quartz, plagioclase, and alkali feldspar, with

occasional biotite, hornblende, and detrital calcite grains. Crystal fragments are generally angular, and

feldspars typically exhibit cracking along cleavage planes wherein clay minerals have formed.

Lithic fragments (~20%), typically <1 mm, composed of subrounded to rounded dark brown to grayish brown

composite grains containing fine grained quartz, feldspar and clay minerals; some contain calcite.

Volcanic glass fragments (~2%), vitric or partially devitrified flattened pumice fragments (fiamme), generally
<1 mm in size.

Matrix: Abundant brown to dark brown clay minerals, with smaller amounts of secondary carbonate. Clay minerals sometimes form thick mantles on detrital grains, especially on feldspars and volcanic glass fragments. Textures suggest some *in situ* clay mineral growth. Intergranular spaces are largely filled with very fine-grained clay mineral intergrowths. However, small irregular voids are present, both within the matrix, and as spaces along grain boundaries. These voids are lined with secondary micro-crystalline clays + calcite (grain sizes on the order of 1 or 2 μm). Some of the voids form discontinuous, sublinear cracks.

U-1a.102C drift (0+77 ft) – Sample V4

Position: 10.5 ft to the right of the left rib; 4.0 ft above the invert

Lithologic Description and Occurrence

Type 1 or 1/4, volcanoclastic sand and silt; yellowish brown; moderately well indurated. Moderately to well sorted, containing rare subangular to subrounded clasts ranging in size from <1 in. (2.5 cm) to >15 in. (38 cm). Clasts are dominated by Pre-Tertiary clastic or carbonate lithologies. Laminated bedding consists almost entirely of sand, silt and clay sized particles, and contains some secondary calcite cement. Average bed thickness is ~18 in. (~45 cm).

Petrographic Description

Moderately well-sorted sandy siltstone or sandy claystone. Detrital grains and crystal fragments comprise up to 40 to 45% of the sample. Matrix is clay-rich.

Detrital material includes the following:

Crystal fragments (15-20%), up to 1 mm maximum, but typically ≤ 0.5 mm in size, dominated by angular to

subangular fragments of plagioclase, alkali feldspar and quartz, with minor biotite, hornblende and calcite.

Lithic fragments (~20%), up to 2 mm, but generally < 1 mm; composed of subrounded dark brown to grayish

brown grains of variable composition. Generally clay-rich, but may also contain silt-size quartz and feldspar.

Volcanic glass fragments (~2%), vitric or partially devitrified pumice and glass shards.

Matrix: Variable in composition but dominated by mottled brown to grayish-brown clay minerals, tiny crystal fragments (<0.1 mm), and carbonate minerals. Clay minerals occur in clumps and bands, commonly wrapping around and coating detrital grains. Some of the clays evidently formed by *in situ* crystallization. Dark brown clays show a reddish color in reflected light, indicative of hematite inclusions. Carbonate and volcanic glass fragments look ragged and partially altered to clay along grain boundaries.

The rock contains abundant pore space; voids are characteristically small (< 0.5 mm) and irregular, and typically occur along grain boundaries. Clay minerals (and sometimes calcite) form microcrystalline linings on voids, showing up as thin “bright” films on the wall of the voids (in crossed polars).

U-1a.102C drift (0+77 ft) – Sample V5

Position: 10.3 ft to the right of the left rib; 2.9 ft above the invert

Lithologic Description and Occurrence

Type 3, cobble-rich, gravelly sand; yellowish-brown; moderately to poorly indurated. Poorly sorted, containing abundant large, subangular clasts that are commonly 5 to 6 in (12.7 to 15.2 cm) across, but range in size down to < 1 in (2.5 cm). Clasts are dominated by pre-Tertiary lithologies (especially carbonate rock) but also include tuffaceous fragments. Most of the larger clasts are composed of carbonate rock that commonly exhibit secondary calcareous rinds. Elongated clasts show a weak preferred orientation parallel to bedding. Matrix is dominated by sand and silt-sized grains. Bed thickness is ~12 in (30 cm) at the sample point, but pinches and swells across the exposure (necking down to as little as 4 inches [10.2 cm]). High energy fluvial depositional environment.

Petrographic Description

Two different thin sections were prepared. Section #1 was cut from a tuffaceous lithic fragment. Section #2 consists of disaggregated volcanoclastic sedimentary detritus.

V5 Section #1

Clast: 1.5 in (3.8 cm) diameter lithic fragment of partially welded volcanic tuff. Contains ~35% euhedral to subhedral phenocrysts, up to 2 mm in maximum dimension. These include: plagioclase + alkali feldspar (~20%), quartz (~5%), biotite (2-3%), clinopyroxene rimmed by hornblende overgrowths (<1%), and Fe-Ti oxides (2%). Volcanic glass matrix contains partially welded glass shards with flow banded texture, and sparse pumice fragments. Glass shards exhibit wrap-around textures surrounding phenocrysts and pumice fragments. Much of the glassy matrix is partially to completely devitrified.

Matrix: Only a small amount of sedimentary matrix is attached to the rim of the clast. It consists primarily of brown clay minerals in granular clumps, with small sand or silt-sized inclusions of crystal and lithic fragments, and glass shards.

V5 Section #2

Thin section was cut from disaggregated sand and silt-sized detritus that was potted in epoxy and polished. Although not intact, it provides a good indication of the sediment composition for this sample.

Detrital material includes the following:

Crystal fragments (~15%), up to 1 mm maximum size, including angular to subangular fragments of plagioclase,

alkali feldspar, quartz, biotite, and calcite. Much of the crystalline detritus is variably replaced by secondary clay minerals.

Lithic fragments (~20%), up to 3 mm, but generally ~1 mm; rounded to subrounded brown to grayish-brown grains

composed of clays ± silt-size quartz and feldspar ± calcite. Some of the carbonate-rich fragments include

blocky calcite vein material. Detritus also includes a 2.5 mm shell fossil (gastropoda?) whose interior is filled with secondary calcite spar.

Volcanic glass fragments (~5%), partially devitrified pumice fragments with clay rims. Matrix: Largely composed of brown clay minerals, associated with small (<0.5 mm) detrital fragments that have been partially or completely replaced by clays. Some of the clay minerals are well crystallized and typically coarser grained than the material that is replacing crystal and lithic fragments. Secondary clays minerals are also replacing volcanic glass and carbonate-rich detrital grains. Secondary calcite has developed (along with clay minerals) on some of the carbonate-rich grains.

U-1a.102D drift (0+21 ft) – Sample D1

Position: ~5 ft above the invert, on the right rib of the drift

Lithologic Description and Occurrence

Type 1, alluvial “wall rock” directly below a thin air-fall tuff layer (sample D2). The alluvium was slightly baked by the heat from the air-fall tuff. Dominantly sand and silt-size material; yellowish-brown; hard and well indurated, but relatively porous. Well sorted, containing rare subrounded pebbles to ~ 1 cm representing both tuffaceous and pre-Tertiary lithologies. Also contains small vugs lined with secondary calcite spar.

Petrographic Description

Silty sandstone with clay rich matrix. Detrital material includes the following:

Crystal fragments (~20%), up to 1 mm maximum size, including angular fragments of feldspar, quartz, calcite, biotite, hornblende and Fe-oxides.

Volcanic glass fragments (~15%), glassy to partially devitrified pumice fragments up to 3 mm in size.

Lithic fragments (10-15%), generally ≤ 1 mm; rounded to subrounded composite clastic and carbonate fragments, usually dominated by clay minerals, but also containing silt-sized quartz, feldspar, calcite, and Fe-oxide grains.

The latter show a reddish color in reflected light, indicative of hematite (Fe_2O_3).

Matrix: Consists of compact brown to greyish brown fine-grained clay minerals, commonly exhibiting banded, layered, and matted textures. Matrix also includes patchy fine-grained carbonate minerals. In general, the clay matrix is dense, and completely encloses detrital grains. Clay replacement textures are observed on some detrital grains, especially volcanic glass and feldspar fragments.

The rock contains abundant porosity, but in contrast to many of the U-1a samples, most of the pores are *not* associated with detrital grain boundaries. The pores commonly occur entirely within the fine-grained clay matrix, and have the appearance of trapped fluid pockets. Clay minerals form concentric bands or layers around the pores, which are generally smooth walled and range in shape from nearly spherical to highly irregular. Most of the voids are lined only with microcrystalline clay minerals; a few contain fine-grained calcite. The well-developed

secondary clay minerals may have originated from weak thermal overprinting of the rock following deposition of the overlying air-fall tuff layer.

U-1a.102D drift (0+21 ft) – Sample D2

Position: ~5 ft above the invert, on the right rib of the drift

Lithologic Description and Occurrence

Air-fall tuff, pale grayish-brown; dense, compact, and relatively well indurated. Vitric to partially devitrified glass, containing sparse fine-grained phenocrysts, pumice and lithic fragments. The exposed bed is only 1 to 2 inches (2.5 to 5 cm) thick, but can be up to 24 inches (~60 cm) thick in other drifts within the U-1a complex.

Petrographic Description

Relatively homogeneous volcanic tuff consisting almost entirely of partially welded glass shards, most of which consist of single-wall vesicle fragments. Individual glass shards rarely exceed 0.5 mm in length. No long-range preferred orientation, but some short-range parallel alignment of shards is observed.

Phenocrysts comprise only 1-2% of the rock mode, consisting of feldspar and quartz crystals, generally 0.2 mm in size, but rarely up to 1 mm. A few dark brown lithic fragments (<1 mm) are also included in the glass matrix (comprising <1% of the mode).

Much of the rock has been overprinted with secondary calcite, which replaces the glass matrix in discontinuous patches, and completely fills occasional small voids in the rock (up to 0.75 mm in maximum dimension). No calcite veining is observed. In the areas where calcite is absent, careful examination of the glass shards at high power magnification reveals that they are partially devitrified along their rims to a mineral with first order gray birefringence. The replacement mineral is probably either silica or a zeolite mineral. In most of the section, the calcite overprinting is so pervasive that this devitrification process is not observable.